

# ACOUSTIC INVERSION METHODS USING SHIP NOISE

by

Michael G. Morley  
B.Sc. University of Victoria, 1997

A Thesis Submitted in Partial Fullfillment of the  
Requirements for the Degree of  
MASTER OF SCIENCE  
in the School of Earth and Ocean Sciences

© Michael G. Morley, 2007  
University of Victoria

All rights reserved. This thesis may not be reproduced in whole or in part, by  
photocopy or other means, without the permission of the author.

# Acoustic Inversion Methods using Ship Noise

by

Michael G. Morley  
B.Sc., University of Victoria, 1997

## Supervisory Committee:

---

Dr. N. Ross Chapman, Supervisor (School of Earth and Ocean Sciences)

---

Dr. Stan E. Dosso, Co-Supervisor (School of Earth and Ocean Sciences)

---

Dr. George Spence, Departmental Member (School of Earth and Ocean Sciences)

---

Dr. David J. Thomson, External Examiner

Supervisor: Dr. N. Ross Chapman (University of Victoria)

Co-Supervisor: Dr. Stan E. Dosso (University of Victoria)

Departmental Member: Dr. George Spence ( University of Victoria)

## Abstract

In this thesis, acoustic inversion methods are employed to estimate array element locations and the geoacoustic properties of the seabed using measured acoustic data consisting of noise from a surface ship in the Gulf of Mexico. The array element localization utilizes relative travel-time information obtained by cross-correlating the recorded time series of ship noise received at spatially separated hydrophones. The relative travel-time data are used in an inversion, based on the regularized least-squares method and the acoustic ray tracing equations, to obtain improved estimates of the receiver and source positions and their uncertainties. Optimization and Bayesian matched-field inversion methods are employed to estimate seabed geoacoustic properties and their uncertainties in the vicinity of a bottom-moored vertical line array using the recorded surface ship noise. This study is used to test the feasibility of matched-field methods to detect temporal changes in the geoacoustic properties of the seabed near a known gas hydrate mound in the Gulf of Mexico. Finally, a synthetic study is performed that demonstrates how ignoring environmental range dependence of seabed sound speed and water depth in matched-field inversion can lead to biases in the estimated geoacoustic parameters. The study considers the distributions of optimal parameter estimates obtained from a large number of range-independent inversions of synthetic data generated for random range-dependent environments. Range-independent Bayesian inversions are also performed on selected data sets and the marginal parameter distributions are examined. Both hard- and soft-bottom environments are examined at a number of scales of variability in sound speed and water depth.

---

# Table of Contents

Supervisory Committee	ii
ABSTRACT	iii
Table of Contents	iv
List of Tables	vi
List of Figures	vii
Acknowledgements	xi
Dedication	xii
<b>1 Introduction</b>	<b>1</b>
1.1 Motivation . . . . .	2
1.1.1 Natural gas hydrate . . . . .	3
1.1.2 Gulf of Mexico gas hydrate monitoring station . . . . .	5
1.2 Acoustic inversion with ship noise . . . . .	8
1.3 Statement of work . . . . .	8
<b>2 Theory</b>	<b>10</b>

---

2.1	General inverse theory . . . . .	10
2.2	Matched-field inversion . . . . .	11
2.3	Optimization inversion . . . . .	13
2.3.1	Downhill simplex method . . . . .	13
2.3.2	Simulated annealing . . . . .	14
2.3.3	Adaptive simplex simulated annealing . . . . .	16
2.4	Bayesian inversion . . . . .	19
2.4.1	Bayesian formulation . . . . .	19
2.4.2	Metropolis-Gibbs sampling . . . . .	22
2.4.3	Fast Gibbs sampler . . . . .	24
2.5	Likelihood-based mismatch functions . . . . .	25
2.6	Acoustic propagation theory . . . . .	27
2.6.1	Normal modes . . . . .	29
2.6.2	ORCA normal-mode model . . . . .	32
2.6.3	Parabolic equations . . . . .	33
2.6.4	PECan model . . . . .	35
<b>3</b>	<b>Description of experiment</b>	<b>37</b>
3.1	Data acquisition . . . . .	37
3.2	Data quality . . . . .	43
<b>4</b>	<b>Array element localization using ship noise</b>	<b>46</b>
4.1	Ray tracing . . . . .	47
4.2	Linearized inversion . . . . .	51
4.3	Cross-correlation data processing . . . . .	56
4.4	Results . . . . .	59
4.5	Array geometry and source repositioning: synthetic case study . . . . .	66
4.6	Discussion . . . . .	69

---

<b>5</b>	<b>Matched-field inversion using ship noise</b>	<b>70</b>
5.1	Ship noise . . . . .	70
5.2	Data pre-processing . . . . .	71
5.3	Optimization inversion of ship-noise data . . . . .	74
5.4	Bayesian inversion of ship-noise data . . . . .	80
5.5	Synthetic data example . . . . .	82
5.6	Discussion . . . . .	84
<b>6</b>	<b>Parameter estimate biases in geoacoustic inversion</b>	<b>85</b>
6.1	Introduction . . . . .	85
6.2	Forward modelling . . . . .	88
6.2.1	Geoacoustic model and range dependence . . . . .	88
6.2.2	Propagation modelling . . . . .	89
6.3	MFI ensemble results . . . . .	91
6.3.1	Methodology . . . . .	91
6.3.2	Range-dependent sound speed . . . . .	93
6.3.3	Range-dependent bathymetry . . . . .	98
6.4	Bayesian inversion results . . . . .	102
6.5	Summary and discussion . . . . .	105
<b>7</b>	<b>Conclusions and future work</b>	<b>107</b>
	<b>References</b>	<b>111</b>
	<b>List of Abbreviations</b>	<b>119</b>

# List of Tables

5.1	Summary of optimization inversion results from MC798 data set. . . .	79
5.2	Summary of Bayesian inversion results from the MC798 dataset. . . .	82
6.1	Summary of PECan input parameters, and results from benchmarking of range-independent PECan and ORCA. . . . .	91

---

## List of Figures

1.1	Diagram depicting the proposed gas hydrate seafloor observatory. . .	7
2.1	Graphical representation of an $M=3$ simplex. . . . .	15
3.1	Gulf of Mexico map . . . . .	39
3.2	Vertical line array schematic diagram . . . . .	40
3.3	MC798 bathymetry and ship track lines . . . . .	41
3.4	MC798 water column sound speed profile . . . . .	42
3.5	Ship noise spectra at each hydrophone. . . . .	44
3.6	Spectral levels of ship noise versus background. . . . .	45
4.1	Sample of raw ship-noise data and processed cross-correlation data. .	57
4.2	Spectrogram of ship noise. . . . .	58
4.3	Raster image of cross-correlation data . . . . .	59
4.4	Cross-correlation data picks. . . . .	60
4.5	Plan view of prior and recovered ship and VLA locations. . . . .	62
4.6	Estimated vertical array shape. . . . .	63
4.7	Data residuals from prior and recovered model estimates. . . . .	64
4.8	Estimated uncertainties for AEL solution. . . . .	65
4.9	Geometry for the synthetic example. . . . .	67

---

4.10	Plan view of AEL solution for synthetic example. . . . .	68
4.11	Absolute and linearized estimates of source position uncertainty. . . . .	69
5.1	Spectrograms of ship noise along each track line. . . . .	72
5.2	Assumed geoacoustic model for MC798. . . . .	77
5.3	ASSA inversion results for data snapshot 5259. . . . .	78
5.4	ASSA inversion results for data snapshot 5274. . . . .	78
5.5	FGS inversion results for data snapshot 5259. . . . .	81
5.6	FGS inversion results for data snapshot 5274. . . . .	81
5.7	FGS inversion results for range-independent, synthetic case. . . . .	83
6.1	Range-independent environmental model. . . . .	88
6.2	Sample realizations of randomly varying bathymetry and distributions of seafloor slope angle. . . . .	90
6.3	Parameter distributions from single-frequency inversions with range- dependent sound speed for the hard-bottom case. . . . .	93
6.4	Parameter distributions from multi-frequency inversions with range- dependent sound speed for the hard-bottom case. . . . .	95
6.5	Summary of inversion results for range-dependent sound speed for the hard-bottom case. . . . .	95
6.6	Parameter distributions from multi-frequency inversions with range- dependent sound speed for the soft-bottom case. . . . .	97
6.7	Summary of inversion results for range-dependent sound speed for the soft-bottom case. . . . .	97
6.8	Averaged reflection coefficient curves for random fluctuations in sound speed for hard- and soft-bottom cases. . . . .	98
6.9	Parameter distributions from multi-frequency inversions with range- dependent water depth for the hard-bottom case. . . . .	99

---

6.10	Summary of inversion results for range-dependent water depth for the hard-bottom case. . . . .	100
6.11	Summary of inversion results for range-dependent water depth for the soft-bottom case. . . . .	101
6.12	Comparison between hard- and soft-bottom inversion results for different values of $\lambda_{max}$ . . . . .	102
6.13	Marginal distributions from single realization of data for range-dependent sound speed (soft-bottom case). . . . .	104
6.14	Marginal distributions from single realization of data for range-dependent water depth (hard-bottom case). . . . .	104

## Acknowledgements

I would like to thank my supervisors, Dr. Ross Chapman and Dr. Stan Dosso for the considerable direction, guidance, and patience they have shown me over the years. I would also like to thank Dr. Yongmin Jiang, Dr. Erika Geresi, Dr. Michael Wilmut, Dr. Steve Bloomer, and the other past and present members of the Ocean Acoustics group for their helpful discussions and debates.

I could not have come this far without the support of my family: my parents, Dale and Pat Morley, my sister, Cheryl, and especially my brother, Darren. Many thanks also to all of my friends. The support and encouragement of my family and friends was vital during many difficult times over the past several years, and it was through them that I found the strength to finish.

I would like to thank JASCO Research Ltd., Barrodale Computing Services, and General Dynamics Canada for the contract opportunities I enjoyed during my tenure as a graduate student. I would also like to thank Liesa Lapinski and Dave Chapman at DRDC Atlantic for providing some of the computer codes used in this work.

Financial support for this research was provided by the Minerals Management Service, a bureau in the U.S. Department of the Interior. I would like to thank Dr. Robert Woolsey, Dr. Thomas McGee, Carol Lutken and the Mississippi Mineral Resources Institute at the University of Mississippi for supporting this research.

# Dedication

Dedicated in loving memory to my mother, Patricia Irene Morley, July 31, 1942 – February 19, 2004. Your courage was an inspiration to us all.

# Chapter 1

## Introduction

*Acoustic inversion* describes a common class of problems in the field of underwater acoustics that includes the use of measured acoustic fields to estimate properties of the ocean environment such as the geoacoustic properties of the seabed (*geoacoustic inversion*) and/or the positions of the acoustic sensors of an experiment (*array element localization*). *Geoacoustic properties* refers to those material properties that impact the propagation of an acoustic field through the seabed such as sediment layer thicknesses, compressional and shear wave speed, density, and compressional and shear wave attenuation.

In this thesis, an array element localization (AEL) acoustic inversion method is applied to obtain improved estimates of the positions of the hydrophones on a receiver array using a ship of opportunity (in this case the survey ship) as a sound source. Subsequently, matched-field inversion (MFI) methods are applied to estimate the geoacoustic properties of the seabed in the vicinity of the array using the same ship-noise source. Finally, a synthetic study is performed to examine the effect that ignoring environmental range dependence has on the geoacoustic parameter estimates from MFI.

AEL involves accurate localization of the individual sensors of an acoustic array using measured acoustic travel times between the receivers and a number of sources.

The inversion method is based on a regularized least-squares approach, whereby the model that best fits the data is found by iteratively solving a system of equations consisting of a locally linear approximation to the acoustic ray equations (e.g., [1–7]). Prior information such as knowledge of the approximate locations of the receivers and sources from the deployment procedure, and the expectation that the hydrophone array shape is a smooth function of position can be used to constrain the solution [1, 3]. The data used in this thesis consists of relative acoustic arrivals of a ship-noise recordings obtained by cross-correlating the signals received at spatially separated receiver pairs.

MFI estimates seabed geoacoustic parameters by comparing measured acoustic fields with replica fields computed for candidate geoacoustic models to determine the model parameters that minimize the mismatch (e.g., [8–30]). Much effort has been applied to develop algorithms that efficiently search complicated, multi-dimensional model spaces for the optimal parameters. Grid search methods [8], global-search algorithms such as simulated annealing [9–13] and genetic algorithms [14–17], and hybrid inversion [18–22] have been applied. MFI based on mismatch minimization provides optimal parameter estimates, but no indication of the uncertainty in these estimates. More recently, Markov-chain Monte Carlo methods have been applied to estimate parameter uncertainties within a Bayesian formulation, based on sampling from the posterior probability density [23–27].

## 1.1 Motivation

Historically, geoacoustic inversion has primarily focused on finding approximate values for the regional seabed geoacoustic properties in order to improve sonar performance in locating underwater sound sources. Recently, there has been increased interest in obtaining accurate estimates of the seabed properties themselves. The motivation for the work presented in this thesis is to examine the feasibility of applying matched-

field techniques using noise from a surface ship of opportunity as a sound source in order to monitor the properties of the seabed in the vicinity of a *gas hydrate* outcrop, with the objective of detecting any significant temporal changes in the geoacoustic properties of gas hydrate bearing sediments near the surface.

### 1.1.1 Natural gas hydrate

Gas hydrate refers to a family of crystalline solids made up of a gas molecule surrounded by a lattice of water molecules. Only certain gases, such as carbon-dioxide, hydrogen sulfide, methane and a few other low-carbon-number hydrocarbons, have the molecular size and structure suitable to form hydrate. The most abundant form of naturally occurring gas hydrate is in the Earth's oceans and consists mostly of methane, and hence it is often called "methane hydrate". Hereafter, all references to gas hydrate in this thesis refer to this type.

Gas hydrate has been found in oceanic sediments along continental margins in many regions of the world. Solid gas hydrate is marginally stable within a narrow range of low-temperature and high-pressure conditions, and thus it only exists in ocean depths greater than  $\sim 300$ – $500$  m outside of arctic regions [31].

Under suitable thermodynamic conditions and high concentration of gas, gas hydrate forms in the pore spaces, cracks, and fissures of marine sediments as methane comes into contact with seawater near the seafloor. The methane may be produced locally near the seafloor as a bi-product of the breakdown of organic materials by bacteria, or it may originate from buried hydrocarbon reservoirs and migrate towards the seafloor along faults.

The maximum depth below the seafloor to which solid gas hydrate can form is called the base of the hydrate stability zone (BHSZ). The thickness of the hydrate stability zone (HSZ) is largely controlled by the local geothermal gradient of the Earth and the amount and type of the constituent gas, and is typically less than  $\sim 1000$  m [31]. Below the BHSZ, the geothermal temperature is too high for solid

gas hydrates to form. The BHSZ can sometimes be inferred from seismic reflection profiles as an anomalous horizon that parallels the seafloor reflector with opposite polarity. This bottom simulating reflector (BSR) marks the interface between higher sound speed hydrate bearing sediments above, and lower sound speed sediments and free gas below. Continuous BSRs are not always observed where gas hydrate is present due to complex geology such as salt domes and diapirs that influence the geothermal gradient.

Gas hydrates are of interest to both the research community and offshore industries for three main reasons. First, massive quantities of methane gas are stored as gas hydrate in the seabed worldwide which, if recoverable, represents a significant fossil fuel resource. Estimates of the amount of potentially recoverable methane gas from hydrates vary considerably [32]; however, a common estimate is 10 terratonnes (1 terratonne =  $10^{18}$  g), which greatly exceeds the amount of fossil fuels available from known conventional gas reserves [31]. More recent estimates of the global quantity of gas hydrates have reduced this value by at least an order of magnitude [33, 34]. Second, methane is about 20 times as effective as a greenhouse gas as carbon-dioxide [35]. Past and potential future releases of the methane stored in gas hydrate triggered by sea-level fluctuations could have a significant impact on the global climate; however, this hypothesis is subject to much debate within the scientific community. Finally, gas hydrates are a potential submarine geohazard. This issue is perhaps of the most immediate importance to offshore industries and the research community.

In some circumstances, gas hydrates are capable of cementing sediment grains together, increasing the load bearing capacity of the host sediment. If the thermodynamic equilibrium conditions within the HSZ are altered by some natural or manmade disturbance (e.g., seismic activity, rapid sedimentation, increased bottom-water temperature, seafloor operations), then the gas hydrates could destabilize and dissociate into water and gas, weakening the surrounding sediment [36]. On a large scale, this type of event could potentially trigger a seafloor slump or submarine landslide. There

is evidence to suggest that this was the case for the Storegga Slide off the coast of Norway [37], though the role of gas hydrates in this slide has recently been disputed [38]. In the case of a manmade disturbance, even a small scale seafloor instability has the potential to cause significant damage and human injury to a seafloor operation [39]. In the Gulf of Mexico, as gas seeps up faults from deeper hydrocarbon deposits, massive amounts of gas hydrate often accumulate to form mounds on the seabed <sup>1</sup>. These mounds are ephemeral, capable of changing greatly within a few days [41]. It is believed that events that produce changes in these hydrate mounds also trigger episodes of seafloor instability.

### 1.1.2 Gulf of Mexico gas hydrate monitoring station

The work in this thesis is sponsored by the Center for Marine Resources and Environmental Technology (CMRET) at the University of Mississippi which is partnered with other academic institutions, members of the oil and gas industry, and government agencies with the common goal of conducting inter-disciplinary research to better understand naturally occurring gas hydrate. The CMRET is in the process of establishing a seafloor observatory near a known gas hydrate mound in the Gulf of Mexico for the purpose of continuously and remotely observing the physical and chemical properties of and biological communities associated with the mound, and changes to the composition and spatial distribution of the mound over time [41].

The gas hydrate monitoring station is a continuously evolving concept, and the overall design and types of components to be included (and the location) has changed significantly since work on this thesis began. In the original version of the station's design, the primary acoustic sensory components were a set of bottom moored vertical hydrophone arrays and a single horizontal array of four-component (4-C) hydrophone/geophones on the seafloor. Recognizing the importance of shear wave in-

---

<sup>1</sup>Models have shown that in regions of high gas flux, the increased salinity of the pore water due to hydrate formation inhibits further formation allowing gas to migrate up to the seafloor along high-salinity gas chimneys [40].

formation in gas hydrate detection and quantification, the CMRET redesigned the monitoring station, increasing the number of 4-C horizontal arrays to four, reducing the number of vertical arrays to one, and adding an instrumented borehole array. A diagram of the current proposed configuration of the monitoring station is shown in Fig. 1.1.

In the original concept, after the station is deployed the site would be “calibrated” by collecting seismic data with the arrays using a ship-towed impulsive source such as an air- or water-gun. The data would be processed and interpreted to estimate a detailed geoacoustic model of the environment in the vicinity of the station. Following the calibration, the acoustic noise from ships passing nearby (sources of opportunity) would be recorded autonomously and matched-field processing (MFP) would be applied to estimate the locations of these ships using the known geoacoustic model on a more-or-less continuous basis [41].

MFP is a method for localizing unknown sources of noise in the ocean. MFP is similar to MFI; however, the geoacoustic model is generally held fixed and the search is limited to finding the source range, depth, and azimuth that provides the best match between the measured and replica fields. With greater acoustic interaction with the seabed, the technique becomes more sensitive to the representative environmental model [42], and any mismatch between the assumed geoacoustic model and the true environment can degrade the ability to locate and track these sources [43].

The concept of using MFP to monitor the seabed was that if, at some point, the ability to position the passing ships by MFP was significantly degraded, this might be an indication of a mismatch between the modelled and true environments due to some change in the local geoacoustic properties of the seabed. The site would be resurveyed as necessary using a controlled source to determine if any change had actually occurred and whether it was related to gas hydrate.

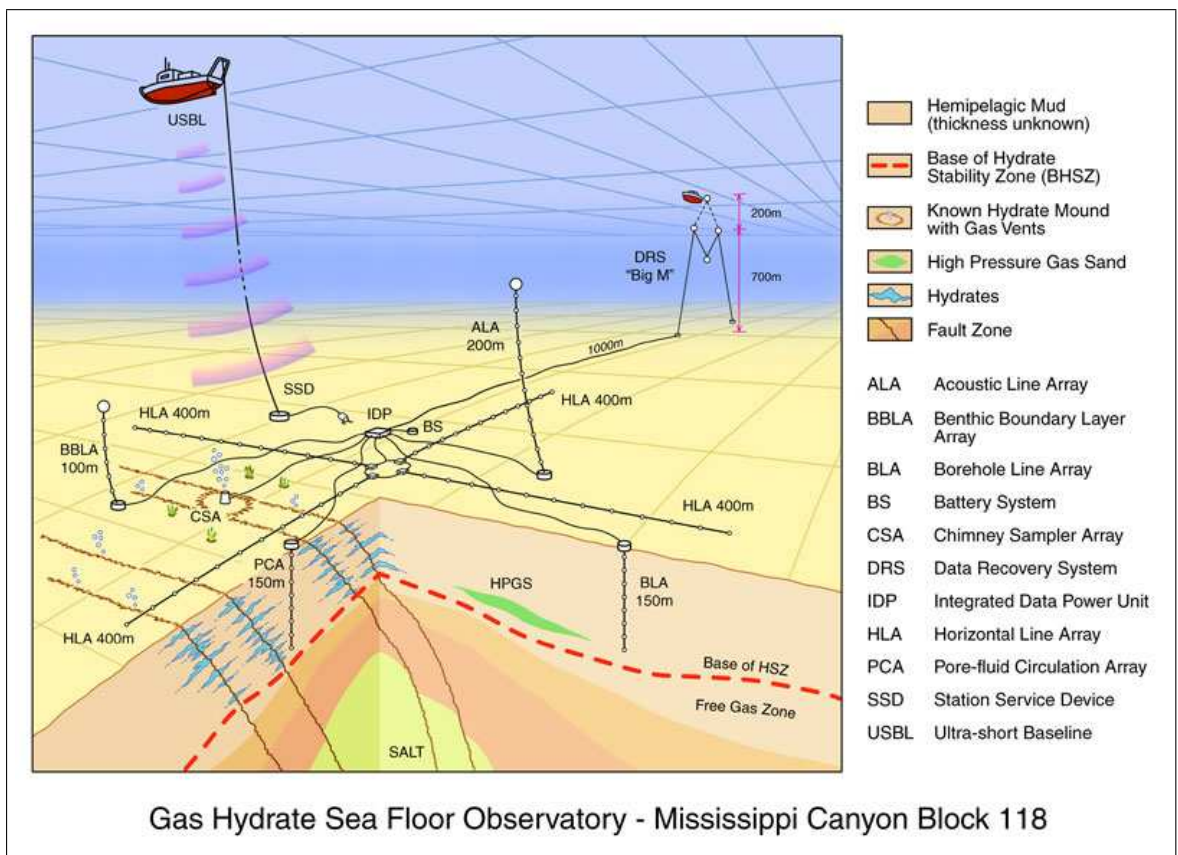


Figure 1.1: Diagram depicting the proposed Gulf of Mexico gas hydrate monitoring station concept (courtesy Specialty Devices Inc.).

## 1.2 Acoustic inversion with ship noise

There are several examples where acoustic inversion techniques have been applied using noise from ships. In Ref. [44] the authors used MFP based on a genetic algorithm search on ship noise to obtain estimates of the hydrophone locations on a horizontal line array. The track of a surface ship was monitored by cross-correlating the ship noise received by horizontally separated receivers in Ref. [45].

Geoacoustic inversion has also been applied using ship noise. In Ref. [46] the authors estimated a sub-bottom sound speed profile from a ship-noise signal that had refracted in the seabed. Their method was based on an inversion of travel-time data obtained by cross-correlating two hydrophone traces. A rudimentary geoacoustic inversion was performed in Ref. [47] based on focalization of the ship position in an ambiguity surface obtained by MFP. More recently, MFI inversion methods based on optimization and Bayesian inference have been applied to ship noise data (e.g., Refs. [48–51])

## 1.3 Statement of work

In this thesis, acoustic inversion is applied to ship-noise data obtained with a prototype vertical line array (VLA) during a research cruise to a candidate monitoring station site in the Gulf of Mexico. One of the primary goals is to use MFI to obtain estimates of the seabed properties in the vicinity of the array in order to examine whether matched-field methods using ship noise are sensitive enough to these properties (for the environment and experimental configuration considered here) to use for seabed monitoring.

First, an AEL inversion is performed to obtain improved estimates of the hydrophone locations. Optimization and Bayesian MFI methods are then applied using the ship-noise data to estimate the geoacoustic properties of the seabed in the vicinity of the array along with estimates of their uncertainties. Finally, a synthetic study

---

is performed to examine biases in MFI that arise due to neglected range-dependent propagation effects.

The thesis is organized as follows: Chapter 2 is devoted to developing the theory behind MFI, the optimization and Bayesian inversion algorithms employed here, and the acoustic propagation models used. Chapter 3 describes the research cruise to the Gulf of Mexico and the quality of the data obtained. An AEL inversion method along with results of an inversion using ship noise are presented in Chapter 4. Results from MFI of ship-noise data from the Gulf of Mexico are discussed in Chapter 5. In Chapter 6 the synthetic study on range-dependent affects to MFI results is discussed, and a summary of conclusions and potential future work is discussed in Chapter 7.

## Chapter 2

# Theory

This chapter is devoted to the theoretical development of the MFI algorithms used in this thesis as well as the different types of likelihood-based mismatch functions and acoustic propagation models employed by them.

### 2.1 General inverse theory

The problem of estimating the parameters of a physical model from a measured set of data is generally known as “inverse theory” [52, 53]. If there exists a suitable mathematical description of how a process interacts with a physical system, one may predict the data or observations measured for a postulated model of that system. This is known as a “forward problem” and can be expressed by the equation,

$$\mathbf{d} = F(\mathbf{m}) \tag{2.1}$$

where  $\mathbf{m}$  is the postulated model,  $\mathbf{d}$  is the predicted data, and  $F$  is a kernel representing a physical process. The forward problem has the properties that a solution always exists, and is unique – that is, a given model will produce only one set of data. An example of a forward problem is to predict the arrival time of seismic energy from

a distant earthquake using a wave propagation model. In this example the Earth represents the physical system and the seismic energy propagating from the earthquake is the process. Conversely, given a measured data set  $\mathbf{d}$  the model  $\mathbf{m}$  that gives rise to the data may be found by solving

$$\mathbf{m} = F^{-1}(\mathbf{d}). \quad (2.2)$$

The “inverse problem” is not as straightforward to solve as the forward problem. Many different approaches have been developed to solve Eq. 2.2 depending on the information provided by the data and the complexity of the problem. It is entirely possible that no solution to the inverse problem exists or that the solution is non-unique. For linear and weakly non-linear inverse problems, closed form solutions to Eq. 2.2 can be derived with analytic expressions for the uncertainty in the model estimate based on the assumed error in the data. If the kernel  $F$  is highly non-linear then closed form solutions are not possible and more computationally intensive methods are required to estimate a model that best fits the data and the uncertainty in that model.

## 2.2 Matched-field inversion

MFI in underwater acoustics is a method for estimating the geometric and geoacoustic parameters of an ocean environment by matching the spatial characteristics (i.e., phase and amplitude) of an acoustic field measured at an array of hydrophones with modelled fields. MFI is an example of a strongly non-linear inverse problem and no closed form solution exists. Solutions to the problem are estimated by an inversion-by-forward-modelling approach, whereby the model  $\mathbf{m}$  is sought that minimizes the mismatch  $E$  between observed data  $\mathbf{d}$  and modelled data  $\mathbf{d}(\mathbf{m})$ . The observed data consist of an acoustic field measured at an array of hydrophones some distance away from a sound source, and transformed to the frequency domain by Fourier meth-

ods. The model,  $\mathbf{m} = \{m_i, i = 1, M\}$ , is a discretized approximation of the true ocean/seabed waveguide. Model parameters that are typically of interest include the geometric parameters of the experiment such as source position, water depth, and hydrophone locations, and the geoacoustic parameters such as the compressional and shear speeds, density, attenuation, and sediment layer thicknesses in the seabed. The modelled data are computed by numerical propagation models that are based on solving the acoustic wave equation to determine the complex valued acoustic field for a given source-receiver geometry and geoacoustic model. Many candidate models are tested and the one that minimizes the mismatch between the measured and modelled data is considered the best solution to the problem [54].

Some drawbacks of this inversion approach are that the solution is non-unique, it provides no estimate of the uncertainty in the model, and as the number of parameters in the problem increases, so does the size and complexity of the model space. Many local minima and steep, narrow valleys may be present in the model space so it must be searched thoroughly to find the globally optimum solution. In such a large and complicated multi-dimensional model space a simple random or gridded search method would need to test a prohibitively large number of trial models to sufficiently search the space to find the optimum model. For this reason a more efficient algorithm must be employed to perform a directed search of the model space. One such algorithm, adaptive simplex simulated annealing (ASSA) [22], is an efficient search algorithm that has been applied to several geoacoustic inverse problems (i.e., Refs. [13, 51, 55–57]) and is discussed in Section 2.3.

MFI based on mismatch minimization provides optimal parameter estimates, but no indication of the uncertainty in these estimates. More recently, Markov-chain Monte Carlo methods have been applied to estimate parameter uncertainties within a Bayesian formulation, based on sampling from the posterior probability density [23–27]. In Section 2.4 the Bayesian approach is described for estimating the uncertainty in the model.

## 2.3 Optimization inversion

ASSA is a search optimization algorithm that is designed to navigate complicated parameter spaces to find the global minimum of a mismatch (or objective) function  $E(\mathbf{m})$ . Expressions for these objective functions are developed in Sec. 2.5. ASSA is a *hybrid* algorithm that combines the advantages of a local search method and a global search method while minimizing their respective weaknesses. ASSA combines an adaptive fast simulated annealing (FSA) algorithm with the downhill simplex method (DHS) to search the parameter space for the globally optimum solution without becoming trapped in sub-optimal local minima.

### 2.3.1 Downhill simplex method

Local search methods seek to minimize the mismatch  $E(\mathbf{m})$  between the observed and calculated data by moving in the direction of the local downhill gradient,  $\frac{\partial E(\mathbf{m})}{\partial m_i}$ , in the search space. The DHS method is a local search method that is sensitive to gradients but does not require the computation of derivatives [58]. The DHS algorithm progresses through a sequence of geometric permutations of a simplex of models to navigate the model space. A simplex is a set of points or vertices that forms a closed, bounded subset within the space. For an  $M$ -dimensional model space, an initial simplex of  $M+1$  models is formed and each model is ranked according to its mismatch. The simplex is represented geometrically for a 3-dimensional parameter space in Fig. 2.1(i). In the first simplex step, the point with the highest mismatch is reflected through the face of the simplex formed by the other models (Fig. 2.1(ii)). If the mismatch of the new model is smaller than all other points in the simplex, an expansion by a factor of two is performed in the same direction (Fig. 2.1(iii)). If the new model fails to reduce the mismatch, a contraction by a factor of one-half towards the face of the simplex is performed (Fig. 2.1(iv)). If none of these steps succeeds in reducing the mismatch then a multiple contraction is performed, shrinking the

simplex by one-half towards the lowest mismatch model (Fig. 2.1(v)).

Local methods such as DHS are efficient at moving downhill towards the minimum mismatch model, but are sensitive to the choice of starting model and can become trapped in local minima. There is no provision for the search to move uphill to escape these minima, hence the model that achieves the minimum mismatch may not be the globally optimum solution. Nevertheless, the DHS method has shown some success in geoacoustic inversion [20, 59].

### 2.3.2 Simulated annealing

Simulated annealing (SA) is an optimization method for finding the maximum or minimum value of a function of many independent variables [61]. The method is based on the thermodynamic annealing process in statistical mechanics whereby the lowest energy state of a material is found by heating the material and slowly lowering the temperature in steps, allowing it to come to thermal equilibrium at each step. In SA, the global minimum of an objective function  $E(\mathbf{m})$ , analogous to the energy state of the material, is sought by performing a directed *Monte-Carlo* search of the parameter space. Random perturbations of a starting model,  $\mathbf{m}$ , form new models,  $\mathbf{m}' = \mathbf{m} + \delta\mathbf{m}$  with energy  $E(\mathbf{m}')$ . Models that decrease  $E$  are always accepted, while those that increase it are accepted if they satisfy the Metropolis criteria [62],

$$P(\Delta E) = \exp\left(\frac{-\Delta E}{T}\right) \geq \xi \quad (2.3)$$

where  $\Delta E = E(\mathbf{m}') - E(\mathbf{m})$  is the difference in function values between the previous and perturbed model states,  $T$  is a temperature control parameter, and  $\xi$  is a random number drawn from a uniform distribution on the interval  $[0, 1]$ . After a prescribed number of models is accepted at each iteration, the temperature is reduced, lowering the probability of accepting models that increase  $E$ . According to Eq. 2.3, even at very low temperatures there is a finite probability of accepting models that increase

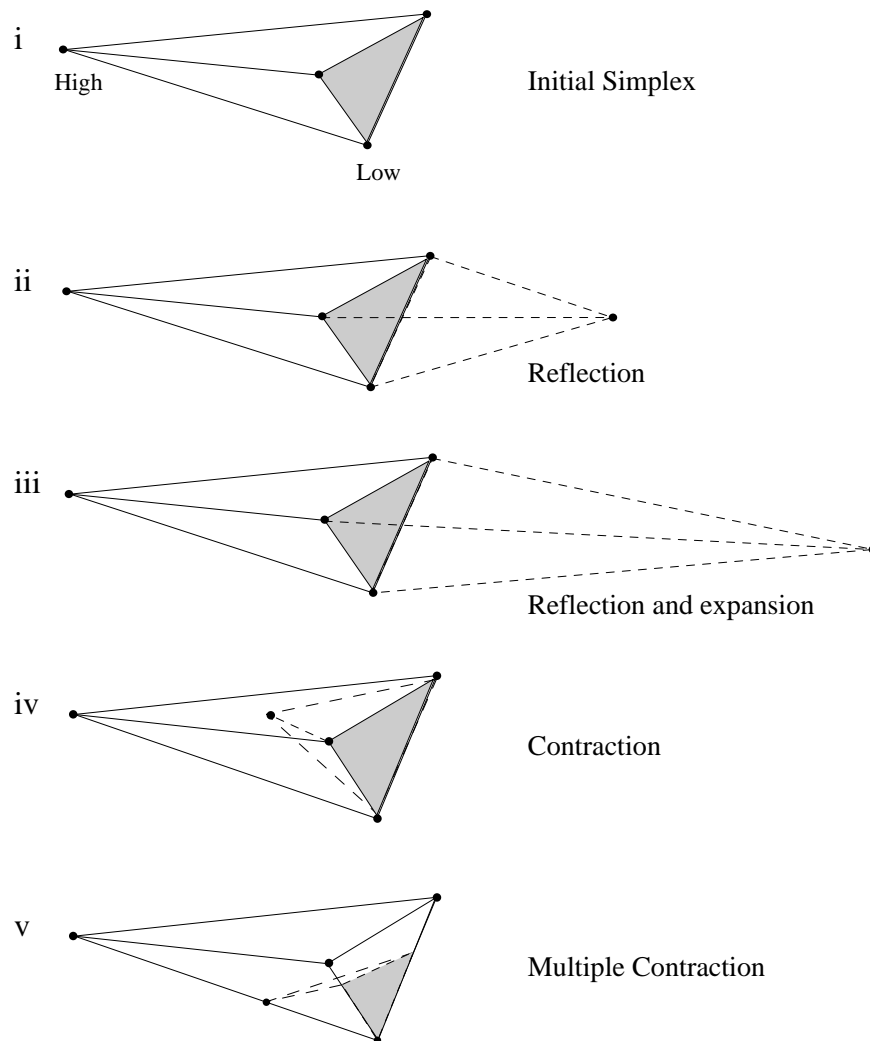


Figure 2.1: Graphical representation of an  $M=3$  parameter simplex after Ref. [60].

$E$ . The temperature is decreased until the maximum number of iterations is reached or until  $\Delta E$  is smaller than some pre-defined value. The initial starting temperature,  $T_0$ , temperature reduction factor,  $\beta$ , the total number of temperature steps and the number of accepted perturbations per step define the *annealing schedule*.

In classical SA the model perturbations are drawn randomly from a uniform probability distribution and the temperature is reduced at each step according to,  $T_k = T_0 / \ln(k)$  where  $k$  is the iteration number. The method of FSA [63] is similar to SA but it uses a Cauchy distribution to generate random model perturbations and a faster cooling schedule given by,

$$T_k = \beta^k T_0 \quad (2.4)$$

where  $\beta < 1$ . The Cauchy distribution has a narrower central peak and longer, flatter tails than the Gaussian distribution which ensures that the majority of the perturbations remain small while allowing occasional large perturbations. The use of the Cauchy distribution and faster cooling schedule in FSA speeds up convergence while allowing a better chance of escaping local minima. Both SA and FSA have been applied to ocean acoustics problems (e.g., Refs. [9–13, 19]).

The random elements of global optimization methods such as SA and FSA allow for uphill steps in the objective function and can avoid becoming trapped in local minima; however, they do not utilize gradient information and are less efficient at moving locally downhill towards the minimum of the objective function than local methods.

### 2.3.3 Adaptive simplex simulated annealing

ASSA combines an adaptive FSA algorithm with the DHS method by performing random perturbations of a simplex of models instead of a single model only [22]. Upper and lower search bounds for the model parameters,  $m_i^- \leq m_i \leq m_i^+$ , are chosen

based on *a priori* knowledge of what are physically reasonable values. An initial simplex of  $M + 1$  models,  $\mathbf{m}_i = \{m_1, m_2, \dots, m_M\}$ , is drawn at random from the parameter space, and a simplex step is performed to obtain a new model,  $\mathbf{m}'$ . A random perturbation is added to each model parameter such that,

$$m_i'' = m_i' + \delta m_i C \quad (2.5)$$

where  $\delta m_i$  is the width of the parameter search interval and  $C$  is a random number drawn from a Cauchy distribution,

$$C = \tan(\eta\pi - 0.5). \quad (2.6)$$

In Eq. 2.6,  $\eta$  is a random number drawn from a uniform distribution on the interval  $[-1, 1]$ . Following each simplex step and random perturbation, the Metropolis criteria (Eq. 2.3) is invoked to determine if the new model is accepted or rejected. When a minimum number of models have been accepted then the temperature is reduced according to Eq. 2.4 and a new iteration begins. The temperature is reduced until the maximum number of temperature steps is reached or a convergence criteria is met. The convergence criteria used here is given by,

$$\frac{|E_{max} - E_{min}|}{|E_{max} + E_{min}|/2} < 10^{-4}. \quad (2.7)$$

In other words, if the difference between the highest and lowest energies in the simplex divided by the mean of those values is less than  $10^{-4}$  then the inversion is said to have converged.

It is important to strike a balance between the randomness of the global search component and the local, gradient based component in hybrid search algorithms. Once the search is in the neighborhood of the global minimum, it would be preferable to concentrate the search near this region in order to speed up convergence. In

order to accomplish this one can scale the size of the random perturbations by some amount, reducing the range of possible perturbations for each model parameter after each iteration, thereby decreasing the random component of the search algorithm. If some of the parameters are more sensitive than others (i.e. they converge towards the optimum value at higher temperatures) then the distributions from which these perturbations are drawn from need not be as large. ASSA adaptively scales the size of the random perturbations of each model parameter using information from previous perturbations. It is assumed that the size of recently accepted perturbations should provide a reasonable approximation of the distribution width for subsequent perturbations. Two user-defined control parameters,  $s$  and  $S$ , determine the scale factor. For the first  $S$  perturbations the distribution width,  $\delta m_i$ , is set to  $m_i^+ - m_i^-$  after which it is equal to the lesser of  $m_i^+ - m_i^-$  or  $s\bar{m}_i$ , where  $\bar{m}_i$  is the mean of the last  $S$  accepted perturbations of  $m_i$ . Typical values of  $s$  and  $S$  that are used are 3 and 30 respectively. If the perturbation size becomes too small at some stage of the inversion, then a situation may occur where nearly all the models tried are accepted and the inversion can get stuck in one area of the search space. In this case, ASSA has the ability to increase the size of the perturbations by an empirical factor of  $1/\beta^2$ , based on the temperature reduction factor. The criteria for growing the perturbation size is if more than 50% of the model perturbations are accepted at a given temperature step.

With an appropriate annealing schedule, the ASSA hybrid algorithm with adaptive perturbation scaling balances the tradeoff between random and gradient directed searching and is a very efficient at finding the optimum solution to highly non-linear inverse problems.

## 2.4 Bayesian inversion

For linear inverse problems, the uncertainty in the estimated model parameters can be derived analytically based on assumptions about the statistics of the errors in the data. It is often assumed that the data errors are random and Gaussian-distributed in which case the errors in the estimated model will also be Gaussian. For non-linear inversion problems such as MFI, optimization algorithms such as ASSA can determine a model that yields the best fit to the data; however, they provide no estimates of the uncertainty in the model parameters. Model uncertainties can be estimated through a Bayesian inference approach whereby information from the measured data is combined with prior information about the model to form the multi-dimensional posterior probability density (PPD). The PPD is the complete solution to the inverse problem and integral moments of the PPD provide estimates of the mean, covariance, and marginal distributions of the model parameters. Estimating the PPD requires efficient sampling and evaluation of models from the parameter space and care must be taken to ensure that the method produces an unbiased estimation. A general description of the Bayesian inversion technique and applications to geophysical inverse problems can be found in Refs. [54, 64]. The Bayesian inversion algorithm described here and developed in Refs. [25, 26] uses a Gibbs sampling approach based on the Metropolis criteria and provides an unbiased sampling of the PPD.

### 2.4.1 Bayesian formulation

Most inverse problems seek to find an estimate of a fixed “true model” that best fits the data. Bayesian inversion differs in that there is no assumption of a fixed true model, but instead the model is treated as random variable which can be described statistically. A summary of the Bayesian formulation follows. Given model and data vectors  $\mathbf{m} = [m_1, m_2, m_3, \dots, m_M]^T$  and  $\mathbf{d} = [d_1, d_2, d_3, \dots, d_N]^T$ , where  $m_i$  and  $d_i$  are

random variables, the joint probability of  $\mathbf{m}$  and  $\mathbf{d}$  is

$$P(\mathbf{m}, \mathbf{d}) = P(\mathbf{m}|\mathbf{d})P(\mathbf{d}), \quad (2.8)$$

where  $P(\mathbf{m}|\mathbf{d})$  is the conditional probability density function of the model given the data and  $P(\mathbf{d})$  is the probability density function of the data. It must also be true that

$$P(\mathbf{m}, \mathbf{d}) = P(\mathbf{d}|\mathbf{m})P(\mathbf{m}), \quad (2.9)$$

where  $P(\mathbf{m})$  is the probability density function of the model, independent of the data. Equating 2.8 and 2.9, and solving for  $P(\mathbf{m}|\mathbf{d})$  yields Bayes' rule

$$P(\mathbf{m}|\mathbf{d}) = \frac{P(\mathbf{d}|\mathbf{m})P(\mathbf{m})}{P(\mathbf{d})}, \quad (2.10)$$

which expresses the information about the model given the data. If  $\mathbf{d}^{obs}$  denotes a measured data set, then substituting  $\mathbf{d} = \mathbf{d}^{obs}$  into Eq. 2.10 allows Bayes' Rule to be interpreted as a function of  $\mathbf{m}$  called the likelihood function,  $L(\mathbf{d}^{obs}|\mathbf{m})$ , and Eq. 2.10 becomes

$$P(\mathbf{m}|\mathbf{d}^{obs}) \propto L(\mathbf{d}^{obs}|\mathbf{m})P(\mathbf{m}), \quad (2.11)$$

where  $P(\mathbf{m}|\mathbf{d}^{obs})$  is the PPD describing the state of information of the model given both the prior information and the data, and  $P(\mathbf{m})$  is the probability density function that describes any prior knowledge of the model independent of the data. In Eq. 2.11  $P(\mathbf{d}^{obs})$  is a constant of proportionality since  $\mathbf{d}^{obs}$  is fixed.

Choosing an appropriate likelihood function depends on the nature of the data errors for the problem being considered. Sources of error on the data can include both measurement and instrument error, and theory error which arises due to simplifying assumptions made about the model and the physics of the forward problem. Since it is difficult (often impossible) to quantify these errors independently, assumptions must be made about their statistics. Assuming that the data errors are uncorrelated,

Gaussian-distributed random variables, the likelihood function is of the form

$$L(\mathbf{d}^{obs}|\mathbf{m}) \propto \exp[-E(\mathbf{m}, \mathbf{d}^{obs})], \quad (2.12)$$

where  $E(\mathbf{m}, \mathbf{d}^{obs})$  is an error function that quantifies the misfit between the observed and predicted data for model  $\mathbf{m}$  given by (for real data)

$$E(\mathbf{m}, \mathbf{d}^{obs}) = -\frac{1}{2}[\mathbf{d}^{obs} - \mathbf{d}(\mathbf{m})]^T \mathbf{C}_D^{-1} [\mathbf{d}^{obs} - \mathbf{d}(\mathbf{m})]. \quad (2.13)$$

In Eq. 2.13,  $\mathbf{C}_D$  represents the data covariance matrix and  $^T$  represents a matrix transpose. Substituting the likelihood function into Eq. 2.11 the expression for the PPD becomes

$$P(\mathbf{m}|\mathbf{d}^{obs}) \propto \exp[-E(\mathbf{m}, \mathbf{d}^{obs})]P(\mathbf{m}), \quad (2.14)$$

or

$$P(\mathbf{m}|\mathbf{d}^{obs}) = \frac{\exp[-\phi(\mathbf{m}, \mathbf{d}^{obs})]}{\int \exp[-\phi(\mathbf{m}', \mathbf{d}^{obs})]d\mathbf{m}'} \quad (2.15)$$

where

$$\phi(\mathbf{m}) = E(\mathbf{m}, \mathbf{d}^{obs}) - \log_e P(\mathbf{m}). \quad (2.16)$$

The domain of integration of the denominator in Eq. 2.15 spans the entire model space.

The multi-dimensional PPD is difficult to interpret so to simplify the interpretation, integral moments of the PPD are calculated, such as the posterior mean model and model covariance. Marginal probability distributions provide a 1-D parameter distribution from a higher-dimensional distribution by integrating out the other dimensions. These integral expressions are defined respectively as

$$\langle \mathbf{m} \rangle = \int \mathbf{m}' P(\mathbf{m}'|\mathbf{d}^{obs})d\mathbf{m}', \quad (2.17)$$

$$\mathbf{C}_M = \int (\mathbf{m}' - \langle \mathbf{m}' \rangle)(\mathbf{m}' - \langle \mathbf{m}' \rangle)^T P(\mathbf{m}' | \mathbf{d}^{obs}) d\mathbf{m}', \quad (2.18)$$

$$P(m_i | \mathbf{d}^{obs}) = \int \delta(m'_i - m_i) P(\mathbf{m}' | \mathbf{d}^{obs}) d\mathbf{m}', \quad (2.19)$$

where  $\delta$  represents the Dirac delta function. Equations 2.17–2.19 can be written in the general form

$$I = \int f(\mathbf{m}') P(\mathbf{m}' | \mathbf{d}^{obs}) d\mathbf{m}'. \quad (2.20)$$

The model that maximizes the PPD is called the maximum *a posteriori* (MAP) estimate and can be more meaningful than the posterior mean model if the PPD is multi-modal and/or asymmetric. If the PPD is uni-modal and symmetric the MAP and the posterior mean model coincide. MAP estimates can be obtained from search-optimization methods such as ASSA without having to compute the PPD.

### 2.4.2 Metropolis-Gibbs sampling

In order to estimate the PPD moment integrals (Eq. 2.20), an efficient method of sampling many models from the search space is required. The simplest approach is to perform a grid search in which the model space is divided uniformly, and the misfit of the model is evaluated at each point on the grid. Numerical integration techniques are then used for computing the moments of the PPD. For problems with more than a few dimensions and complicated forward models, this method is impractical due to the computation time required to sample the PPD at a sufficient number of grid points to ensure an unbiased estimate.

The uniform Monte Carlo sampling method estimates the PPD by sampling models randomly from a uniform distribution over the entire model space. The method can be inefficient, since many regions of the space are populated with low-probability models that do not contribute to the integral. Importance sampling methods preferentially draw samples from regions of the space that contribute most to the integrand by sampling from non-uniform distributions. For a non-uniform sampling distribu-

tion,  $g(\mathbf{m})$ , defined such that

$$\int g(\mathbf{m}') d\mathbf{m}' = 1, \quad (2.21)$$

the integral equation (Eq. 2.20) can be written

$$I = \int \left[ \frac{f(\mathbf{m}')P(\mathbf{m}'|\mathbf{d}^{obs})}{g(\mathbf{m}')} \right] g(\mathbf{m}') d\mathbf{m}' \quad (2.22)$$

$$\approx \frac{1}{Q} \sum_{i=1}^Q \frac{f(\mathbf{m}_i)P(\mathbf{m}_i|\mathbf{d}^{obs})}{g(\mathbf{m}_i)}. \quad (2.23)$$

for  $Q$  models  $\mathbf{m}_i$  drawn from  $g(\mathbf{m})$ . A convenient choice of  $g(\mathbf{m})$  comes from the observation that Eq. 2.15 has the same form as the Gibbs distribution,

$$P_G(\mathbf{m}, \mathbf{d}^{obs}) = \frac{\exp[-\phi(\mathbf{m}, \mathbf{d}^{obs})/T]}{\int \exp[-\phi(\mathbf{m}, \mathbf{d}^{obs})/T] d\mathbf{m}}, \quad (2.24)$$

for temperature  $T=1$ . In the method of SA described in Sec. 2.3.3, samples are drawn from the Gibbs distribution using the Metropolis algorithm (Eq. 2.3) with decreasing probability of accepting samples as  $T$  is reduced. Using the Metropolis algorithm at  $T=1$  to draw samples from the Gibbs distribution, the sampling function becomes

$$g(\mathbf{m}) = P(\mathbf{m}|\mathbf{d}^{obs}). \quad (2.25)$$

Substituting Eq. 2.25 into Eq. 2.23 reduces the integral to

$$I \approx \frac{1}{Q} \sum_{i=1}^Q f(\mathbf{m}_i). \quad (2.26)$$

Thus, by the Metropolis-Gibbs sampling method, once  $Q$  samples are drawn from the parameter space using the Metropolis algorithm at  $T=1$ , Eqs. 2.17–2.19 are straightforward to compute.

### 2.4.3 Fast Gibbs sampler

The fast Gibbs sampler (FGS) algorithm (Refs. [25, 26]) uses the method of Gibbs sampling described in Sec. 2.4.2 to provide an unbiased sampling of the PPD integral moments. In FGS, random perturbations are applied to a starting model  $\mathbf{m}$  and the mismatch function  $E(\mathbf{m})$  is evaluated for each new model. The models are accepted or rejected according to the Metropolis criteria (Eq. 2.3) at constant temperature  $T = 1$ . Once a large sample of models has been collected, Eq. 2.26 is applied to compute the moment integrals of the PPD (Eqs. 2.17–2.19).

Correlations between parameters can lead to narrow valleys in the parameter space which can adversely affect the efficiency of sampling. To improve the sampling efficiency in the presence of correlated model parameters, perturbations are performed in a rotated parameter space that diagonalizes the model covariance matrix,  $\mathbf{C}_M$ . An eigenvector decomposition is performed to determine the rotation matrix,  $\mathbf{U}$ , that diagonalizes  $\mathbf{C}_M$  according to,

$$\mathbf{C}_M = \mathbf{U}\mathbf{\Lambda}\mathbf{U}^T \quad (2.27)$$

where  $\mathbf{\Lambda}$  is a diagonal matrix containing the eigenvalues of  $\mathbf{C}_M$ , and the columns of the orthonormal matrix  $\mathbf{U}$  form the corresponding eigenvectors. The rotated model parameters are computed using the orthonormal transformation,

$$\tilde{\mathbf{m}} = \mathbf{U}^T \mathbf{m}. \quad (2.28)$$

During the *pre-rotation* stage of the FGS algorithm, two independent samples of models are collected in parallel and periodically compared for convergence. Convergence occurs when the maximum difference between correlation matrices for the two samples is less than a threshold value,  $\epsilon_r$ . A typical value for  $\epsilon_r$  is 0.25. Once convergence has been established, the covariance matrix of the combined sample is computed and the rotation matrix is obtained. Bounds for the parameters in the rotated space are chosen by drawing a large number ( $\sim 10^5$ ) of models randomly from

a uniform distribution, and transforming them to the rotated parameter space. The maximum and minimum values of each transformed parameter form the bounds in the rotated space.

From this point forward, perturbations are applied in the rotated parameter space and the new models are rotated back to the original space prior to computing the mismatch function  $E(\mathbf{m})$ , and testing for acceptance or rejection by the Metropolis criteria. To ensure that an unbiased sample has been obtained and to verify convergence, two independent samples of models are collected in parallel and periodically inter-compared. When the maximum difference between the cumulative marginal distributions of all the parameters is smaller than a threshold  $\epsilon$  then the sample is said to have converged and the two individual samples are combined to form the final sample. A typical value for  $\epsilon$  is 0.05.

## 2.5 Likelihood-based mismatch functions

The mismatch function  $E(\mathbf{m})$  that is best suited to a particular inverse problem depends on the statistical nature of the errors on the data. The exact nature of these errors is seldom fully understood due to unknown theory errors that arise from simplifying approximations made about the form of the model and the physics of the problem. Some work has been done to rigorously derive mismatch functions applicable to matched-field applications from maximum-likelihood methods (e.g., Refs. [23, 65]). In this section the mismatch functions used in this research are developed following from derivations in Ref. [65].

Consider a set of complex acoustic pressure data,  $\mathbf{d}_f$ , measured at  $N$  hydrophones and  $F$  frequencies. If the errors on the data can be assumed to be zero-mean, Gaussian random variables with uniform variance and are uncorrelated in space and frequency

then the likelihood function for complex data is given by,

$$L(\mathbf{m}, \nu) = \prod_{f=1}^F \frac{1}{(\pi\nu_f)^N} \exp[-|\mathbf{d}_f - \mathbf{d}_f(\mathbf{m})|^2/\nu_f], \quad (2.29)$$

where  $\nu_f$  is the variance at each frequency and  $\mathbf{d}_f(\mathbf{m})$  is the modelled acoustic data. Commonly in matched-field problems the amplitude and phase of the source are unknown in which case the modelled data can be expressed as  $\mathbf{d}_f(\mathbf{m}) \rightarrow A_f e^{i\theta_f} \mathbf{d}_f(\mathbf{m})$  where  $A_f$  and  $\theta_f$  are the arbitrary source amplitude and phase of the modelled data. Substituting this expression into Eq. 2.29 and maximizing the likelihood function with respect to the unknown source amplitude and phase (i.e. setting  $\partial L/\partial A_f = \partial L/\partial \theta_f = 0$ ) gives

$$L(\mathbf{m}, \nu) = \prod_{f=1}^F \frac{1}{(\pi\nu_f)^N} \exp[-B_f(\mathbf{m})|\mathbf{d}_f|^2/\nu_f], \quad (2.30)$$

where  $B_f(\mathbf{m})$  is the normalized Bartlett mismatch,

$$B_f(\mathbf{m}) = 1 - \frac{|\mathbf{d}_f^\dagger \mathbf{d}_f(\mathbf{m})|^2}{|\mathbf{d}_f|^2 |\mathbf{d}_f(\mathbf{m})|^2}. \quad (2.31)$$

This leads to the mismatch function given by

$$E(\mathbf{m}) = \sum_{f=1}^F B_f(\mathbf{m})|\mathbf{d}_f|^2/\nu_f, \quad (2.32)$$

which is the incoherent sum over frequency of the normalized Bartlett mismatch scaled by the ratio of the square of the data magnitude to the variance,  $|\mathbf{d}_f|^2/\nu_f$ . The data variance is seldom known in most experiments and in optimization inversions, the scaling factor is commonly assumed to be the same for each frequency, in which case the mismatch function becomes the familiar uniform Bartlett mismatch,

$$E(\mathbf{m}) = \sum_{f=1}^F B_f(\mathbf{m}). \quad (2.33)$$

This expression is invalid for Bayesian inversion, and for optimization it is seldom a good assumption as most often the errors on the data differ from frequency to frequency. The variances can be implicitly included in the inversion by maximizing the likelihood function (Eq. 2.30) with respect to  $\nu_f$  by setting  $\partial L/\partial \nu_f = 0$ , leading to

$$E(\mathbf{m}) = N \sum_{f=1}^F \log_e [B_f(\mathbf{m}) |\mathbf{d}_f|^2]. \quad (2.34)$$

The *implicit* form of the Bartlett mismatch function (Eq. 2.34) is used for optimization and Bayesian inversions of measured and synthetic data in Chapter 5. In Chapter 6 an additional mismatch function that incorporates an estimate of the data covariance matrix is described and employed in Bayesian inversions of synthetic data.

## 2.6 Acoustic propagation theory

The modelled, or replica, acoustic fields in MFI are calculated using one of several models developed to simulate the propagation of an acoustic signal through a realistic ocean environment. These models are based on solving the acoustic wave equation directly (as in finite-difference and finite-element methods), or numerically by making assumptions that allow mathematical simplifications of the wave equation [66].

The acoustic wave equation is derived from linear approximations of the hydrodynamic equations for conservation of mass, Euler's equation, and the adiabatic equation of state for seawater. The homogenous form of the acoustic wave equation for pressure is (after Ref. [67]),

$$\rho_0(\mathbf{r}) \nabla \cdot \left( \frac{1}{\rho_0(\mathbf{r})} \nabla P(\mathbf{r}, t) \right) - \frac{1}{c^2(\mathbf{r})} \frac{\partial^2 P(\mathbf{r}, t)}{\partial t^2} = 0, \quad (2.35)$$

where the speed of sound in an ideal fluid  $c(\mathbf{r})$  and the density  $\rho_0(\mathbf{r})$  are arbitrary functions of position  $\mathbf{r}$ . Here,  $P(\mathbf{r}, t)$  is the perturbed pressure about the background hydrostatic pressure as a function of position and time. If constant density is assumed,

Eq. 2.35 reduces to the standard wave equation

$$\nabla^2 P(\mathbf{r}, t) - \frac{1}{c^2(\mathbf{r})} \frac{\partial^2 P(\mathbf{r}, t)}{\partial t^2} = 0. \quad (2.36)$$

Applying the time-frequency Fourier transform pair

$$P(\mathbf{r}, t) = \frac{1}{2\pi} \int_{-\infty}^{\infty} p(\mathbf{r}, \omega) e^{-i\omega t} d\omega, \quad (2.37)$$

$$p(\mathbf{r}, \omega) = \int_{-\infty}^{\infty} P(\mathbf{r}, t) e^{i\omega t} dt, \quad (2.38)$$

to Eq. 2.36 leads to the homogenous *Helmholtz equation*

$$[\nabla^2 + k^2(\mathbf{r})] p(\mathbf{r}, \omega) = 0, \quad (2.39)$$

where  $k(\mathbf{r}) = \omega/c(\mathbf{r})$  is the wave number at angular frequency  $\omega$ . Sources are introduced by adding a forcing term  $f(\mathbf{r}, t)$  to the right hand side of Eq. 2.39. For a point source at  $\mathbf{r} = \mathbf{r}_0$  represented by the *Dirac delta function*  $\delta(\mathbf{r} - \mathbf{r}_0)$ , Eq. 2.39 can be written in its inhomogenous, time-independent form

$$[\nabla^2 + k^2(\mathbf{r})] p(\mathbf{r}) = -4\pi\delta(\mathbf{r} - \mathbf{r}_0), \quad (2.40)$$

where harmonic time-dependence of the acoustic field and the source is assumed [67].

Solving the wave or Helmholtz equation, with appropriate boundary conditions and source terms, forms the basis for most numerical methods in ocean acoustics. In this work, two acoustic propagation models based on the normal mode and parabolic equation methods of solving Eqs. 2.39 and 2.40 are employed. A brief overview of these methods is provided in the next two sections.

### 2.6.1 Normal modes

The method of normal modes is an important approach to solving the Helmholtz equation for a range-independent ocean environment bounded by the seafloor and surface.

Consider a point source in an ocean of depth  $h$  with sound speed and density depending only on depth  $z$ . Assuming the acoustic field is cylindrically symmetric about the source, it is convenient to adopt a cylindrical coordinate system with  $\mathbf{r} = (r, \theta, z)$ , in which case Eq. 2.40 can be written <sup>1</sup>

$$\frac{1}{r} \frac{\partial}{\partial r} \left( r \frac{\partial p}{\partial r} \right) + \rho(z) \frac{\partial}{\partial z} \left( \frac{1}{\rho(z)} \frac{\partial p}{\partial z} \right) + \frac{\omega^2}{c^2(z)} p = \frac{-\delta(r)\delta(z - z_0)}{2\pi r} \quad (2.41)$$

for a point source at  $\mathbf{r}_0 = (0, 0, z_0)$ .

Applying the technique of separation of variables to Eq. 2.41, a solution is sought of the form

$$p(r, z) = R(r)Z(z). \quad (2.42)$$

By substituting Eq. 2.42 into the homogenous form of Eq. 2.41 and grouping terms in  $r$  and  $z$ , the equation can be separated into radial and depth equations

$$\frac{1}{r} \frac{d}{dr} \left( r \frac{dR_m}{dr} \right) + k_{rm}^2 R_m = 0, \quad (2.43)$$

$$\rho \frac{d}{dz} \left( \frac{1}{\rho} \frac{dZ_m}{dz} \right) + \left( \frac{\omega^2}{c^2} - k_{rm}^2 \right) Z_m = 0, \quad (2.44)$$

where  $R_m$  and  $Z_m$  are particular functions of  $R$  and  $Z$  obtained with the separation constant  $k_{rm}^2$ .

As a first step in solving the problem, consider the depth-dependent equation (2.44) with the boundary conditions  $p(z)|_{z=0} = 0$  (pressure-release surface) and  $\frac{dp}{dz}|_{z=h} = 0$  (rigid bottom). This is a classical Sturm-Liouville eigenvalue problem with an infi-

<sup>1</sup>Under the assumption of cylindrical symmetry,  $\theta$  dependence is eliminated, reducing the dimensions of the pressure function to  $p = p(r, z)$ .

nite number of solutions, characterized by eigenfunctions  $Z_m(z)$  with corresponding horizontal propagation constants (eigenvalues)  $k_{rm}^2$ . The modal solutions have the following properties:

- The eigenfunctions are orthogonal, i.e.,

$$\int_0^h \frac{Z_m(z)Z_n(z)}{\rho(z)} dz = 0, \quad \text{for } m \neq n. \quad (2.45)$$

- The eigenvalues,  $k_{rm}^2$ , are real valued and ordered as  $k_{r1}^2 > k_{r2}^2 > \dots$  with  $k_{rm}^2 < k_{\max}^2 = \frac{\omega^2}{c_{\min}^2}$ , where  $c_{\min}$  is the lowest sound speed in the problem.
- The  $m$ th mode,  $Z_m$ , has zeros on the interval  $[0, h]$ .
- The eigenfunctions form a complete set, thus any function can be represented as a linear combination of the modes, i.e.,

$$g(r, z) = \sum_{m=1}^{\infty} a_m Z_m(z). \quad (2.46)$$

The eigenfunctions are similar to the the modes of a vibrating string with  $k_{rm}$  analogous to the frequency of vibration. In the ocean acoustic environment, it will be shown that the modes can be interpreted in terms of a vertical standing wave pattern in pressure resulting from interference of up- and down-going waves.

In order to solve the complete inhomogenous Helmholtz equation, we evoke the last property of the modal solution which allows the pressure to be written as

$$p(r, z) = \sum_{m=1}^{\infty} R_m(r)Z_m(z). \quad (2.47)$$

The separation of variables technique is applied by substituting Eq. 2.47 into Eq. 2.41 and applying the operator

$$\int_0^h (\cdot) \frac{Z_m(z)}{\rho(z)} dz. \quad (2.48)$$

This leads to

$$\frac{1}{r} \frac{d}{dr} \left( r \frac{dR_n}{dr} \right) + k_{rn}^2 R_n = -\frac{\delta(r) Z_n(z_0)}{2\pi r \rho(z_0)}, \quad (2.49)$$

where, due to the orthogonality property of the eigenfunctions (Eq. 2.45), only the  $m=n$  terms are retained. Equation 2.49 is a standard Bessel equation whose solution is

$$R_n(r) = \frac{1}{4\rho(z_0)} Z_n(z_0) H_0^{(1,2)}(k_{rn}r), \quad (2.50)$$

where  $H_0^{(1,2)}$  is the zero'th order Hankel function of the first or second kind. Applying the Sommerfeld radiation condition which requires that the acoustic energy radiates only outward in the far field (i.e.,  $k_{rn}r \gg 1$ ), the asymptotic form of the Hankel function of the first kind can be used,

$$H_0^{(1)}(k_{rn}r) \approx \sqrt{\frac{2}{\pi k_{rn}r}} e^{i(k_{rn}r - \pi/4)}. \quad (2.51)$$

Substituting this solution into the equation for pressure (2.47), the far-field solution to the inhomogenous Helmholtz equation for a range-independent environment is

$$p(r, z) \approx \frac{1}{\rho(z_0)\sqrt{8\pi}} e^{i\pi/4} \sum_{m=1}^{\infty} Z_m(z_0) Z_m(z) \frac{e^{ik_{rm}r}}{\sqrt{k_{rm}r}}. \quad (2.52)$$

It can be shown that for a homogenous ocean (constant density and sound speed) with a pressure release boundary at the surface and a rigid bottom, the mode eigenvalues  $k_{rm}(z)$  are given by

$$k_{rm} = \sqrt{\frac{\omega^2}{c^2} - \left[ \frac{(m - \frac{1}{2})\pi}{h} \right]^2}, \quad (2.53)$$

and the eigenfunctions are,

$$Z_m(z) = \sqrt{\frac{2\rho}{h}} \sin \left( \frac{(m - \frac{1}{2})\pi}{h} z \right). \quad (2.54)$$

Thus, the far-field solution for pressure (Eq. 2.52) can be written

$$p(r, z) = \frac{1}{\sqrt{2\pi}h} e^{i\pi/4} \sum_{m=1}^{\infty} \sin(k_{zm}z_0) \sin(k_{zm}z) \frac{e^{ik_{rm}r}}{\sqrt{k_{rm}r}}, \quad (2.55)$$

where the vertical wavenumber  $k_{zm}$  has discrete values

$$k_{zm} = \frac{(m - \frac{1}{2})\pi}{h}. \quad (2.56)$$

The modal solution is interpreted as a set of vertical standing waves formed by the interference of up- and down-going plane waves excited by a source at  $z_0$ , and propagating in range at grazing angle  $\theta_m$ . The acoustic field at any range-depth point in the waveguide is the sum of all the modes. If the argument inside the square root in Eq. 2.53 is positive,  $k_{rm}$  are real valued and the modes propagate outward in range as *trapped* modes; otherwise,  $k_{rm}$  are imaginary and the modes are *evanescent* and decay rapidly with range. Only the propagating modes contribute to long range propagation, and their number increases with water depth and frequency. Higher order propagating modes travel at steeper grazing angles. Mode cut-off occurs at  $k_{rm} = \omega/c$ , beyond which the modes cease to propagate and become pure standing waves.

### 2.6.2 ORCA normal-mode model

The modal solution in the previous section was derived for a simple, homogenous, inelastic waveguide. For more complex environments, the modal spectrum is a combination of discrete and continuous parts and the problem becomes singular [68]. Thus, simulating acoustic propagation through realistic multi-layered environments requires a more sophisticated treatment to order to determine the mode functions and eigenvalues of the problem.

The ORCA normal mode model [68] used in this thesis is an efficient and ro-

bust model for acousto-elastic propagation over a wide range of range-independent environment types. The model employs a mode-finding algorithm that analytically computes the downward- and upward-looking plane wave reflection coefficients  $R_1$  and  $R_2$  at a reference depth and searches the complex  $k$ -plane for points where their product equals unity. At these points, constructive interference between the up- and down-going plane waves occurs and thus these points correspond to mode eigenvalues. Using these eigenvalues, the wave equations for compressional and shear wave potentials are solved for each layer in the problem using Airy functions.

The use of Airy function solutions in ORCA means that computational times increase linearly as a function of frequency and water depth, rather than quadratically as for models based on solving the wave equation numerically. Using the complex  $k$ -plane mode finding option in ORCA, the model is capable of finding both the trapped and evanescent modes exactly, making the solution valid at short ranges and for environments that include attenuation and support shear waves. The real  $k$ -axis option finds only the trapped modes and is much faster; however, it may be inaccurate at short ranges and in environments with moderate to high attenuation [68]. For the work performed for this thesis, the complex  $k$ -plane mode finding algorithm was used.

### 2.6.3 Parabolic equations

The method of normal-modes outlined in the previous sections is valid only for environments whose properties vary only with depth (i.e., are range independent). Extensions to the method such as coupled and adiabatic normal modes approximate range-dependent propagation; however, they are computationally intensive. Parabolic equation (PE) methods of solving the Helmholtz equation are a popular approach to range-dependent propagation in ocean acoustics. The method uses a parabolic approximation to the Helmholtz equation which leads to an initial value problem which can be solved by numerical methods that march the solution out in range. The PE method is less computationally intensive than coupled-mode models, and more

accurate than adiabatic-mode models for complex range-dependent environments.

Consider the homogenous form of the Helmholtz equation for a harmonic point source at  $(0, z_0)$

$$\frac{1}{r} \frac{\partial}{\partial r} \left( r \frac{\partial p}{\partial r} \right) + \rho \frac{\partial}{\partial z} \left( \frac{1}{\rho} \frac{\partial p}{\partial z} \right) + k_0^2 n^2 p = 0, \quad (2.57)$$

where  $k_0 = \omega/c_0$  is a reference wavenumber, and  $n(r, z) = \frac{c_0}{c(r, z)} [1 + i\alpha(r, z)]$  is the index of refraction for sound speed  $c(r, z)$  and attenuation  $\alpha(r, z)$ . Substituting a trial solution of the form <sup>2</sup>

$$p(r, z) = \psi(r, z) \frac{e^{ik_0 r}}{\sqrt{r}} \quad (2.58)$$

into Eq. 2.57, where  $\psi(r, z)$  is an envelope function that varies slowly with range, results in the elliptical wave equation

$$\frac{\partial^2 \psi}{\partial r^2} + 2ik_0 \frac{\partial \psi}{\partial r} + \rho \frac{\partial}{\partial z} \left( \frac{1}{\rho} \frac{\partial \psi}{\partial z} \right) + k_0^2 (n^2 - 1) \psi = 0. \quad (2.59)$$

This equation can be factored into expressions for the incoming and outgoing wavefields. Assuming that the outgoing wavefield dominates (i.e., backscatter is negligible) and the range dependence of  $n(r, z)$  is relatively weak, the the one-way, far-field approximation to the elliptical wave equation can be used,

$$\frac{\partial \psi}{\partial r} = ik_0 (-1 + \sqrt{1 + Q}) \psi. \quad (2.60)$$

In Eq. 2.60,  $Q$  denotes the differential operator

$$Q = n^2 - 1 + \frac{1}{k_0^2} \rho \frac{\partial}{\partial z} \left( \frac{1}{\rho} \frac{\partial}{\partial z} \right). \quad (2.61)$$

In this form, Eq. 2.60 is not directly solvable; however, parabolic approximations (i.e., first order differential equations with respect to  $r$ ) to this equation are obtained by approximating the operator  $\sqrt{1+Q}$ . There are several approaches to approximat-

---

<sup>2</sup>This expression comes from the asymptotic form of Hankel function  $H_0^{(1)}$ , where the far-field approximation ( $k_0 r \gg 1$ ) is assumed.

ing the square-root operator, the choice of which depends on the accuracy and the computational speed required.

In PE methods, the acoustic field is computed by marching the solution out in range. The environment is divided into a grid in range and depth with each range step assumed to be range-independent. The field at range  $r + \Delta r$  is computed by solving Eq. 2.60 at each range step using the field at range  $r$ . The method requires an approximation of the initial starting field at the range of the source, which is computed using a numerical model (e.g., normal modes).

#### 2.6.4 PECan model

In this thesis, the PECan (Parabolic Equations CANadian) propagation model [69] is used where calculations of acoustic data for range-dependent environments are required.

The PECan model is based on an approximation to the wave operator rather than the square-root operator. If  $\psi$  is represented by the Taylor series expansion about  $r + \Delta r$ ,

$$\psi(r + \Delta R, z) = \exp(\Delta r \partial_r) \psi(r, z), \quad (2.62)$$

then Eq. 2.60 can be written

$$\psi(r + \Delta r, z) = \exp \left[ ik_0 \Delta r \left( -1 + \sqrt{1 + Q} \right) \right] \psi(r, z). \quad (2.63)$$

This equation represents the general marching algorithm used in the PE approach. To solve this equation, PECan uses the split-step Padé approach to approximating the wave operator,

$$\exp \left[ ik_0 \Delta r \left( -1 + \sqrt{1 + Q} \right) \right] \approx 1 + \sum_{m=1}^M \frac{A_m Q}{1 + B_m Q}. \quad (2.64)$$

Combining Eqs. 2.63 and 2.64 leads to the basic marching equation for the one-way

field

$$\psi(r + \Delta r, z) = \psi(r, z) + \sum_{m=1}^M \psi_m(r + \Delta r, z), \quad (2.65)$$

where

$$\psi_m(r + \Delta r) = \sum_{m=1}^M \frac{A_m Q}{1 + B_m Q} \psi(r, z) \quad (2.66)$$

is the standard Padé series expansion. The coefficients  $A_m$  and  $B_m$  of the Padé expression are determined in the same fashion as for other PE approaches [70]. Since the split-step Padé algorithm is based on a direct approximation of the wave propagator itself, rather than the square-root operator, larger range steps  $\Delta r$  can be used while maintaining the same level of accuracy, thus reducing computation time [69].

The PE solution is computed on a discrete grid in range and depth. Values of sound speed, density, and attenuation are defined at each point on the grid, interpolated from coarse vertical profiles provided by the user. The size of the grid steps determines the accuracy of the computed field, as well as the number of terms retained in the Padé expression. In general, as the source frequency increases, smaller grid steps and more Padé terms are required. To avoid artificial reflections from the base of the computational grid, an absorbing layer several wavelengths thick is added to the lower portion of the grid. The attenuation is gradually increased within this layer to attenuate the acoustic energy.

PECan has several options for choosing the initial starting field. In this work, the PECan self-starter is used [69]. Losses due to shear wave conversion are approximated in the model through the complex density approach [71]. Though the derivation above is for a 2D environment, PECan is capable of modelling  $N \times 2D$  and 3D propagation. The version of PECan used in this work has been modified to convert it from a stand-alone program to a subroutine that can be called from another program.

## Chapter 3

# Description of experiment

### 3.1 Data acquisition

In October, 2003 a scientific cruise was conducted by the Center of Marine Resources and Environmental Technology (CMRET) at the University of Mississippi to test a prototype VLA, and collect data to be used in the development of software and processing techniques necessary for the gas hydrate monitoring station project. The VLA was deployed at two locations in the northern Gulf of Mexico: Mississippi Canyon, federal lease block 798 (MC798), and Atwater Valley, federal lease block 14 (AV14) (Fig. 3.1). Both sites were considered as candidates for the placement of the monitoring station. The goal of the cruise was to record both impulsive-source seismic data and ship-noise data over similar survey tracks. Data from the impulsive source would be used to develop the seismic data processing techniques specific to the VLA geometry and to estimate a geoacoustic model of the seabed for the region around the VLA. The ship-noise data would be used to test the feasibility of using matched-field methods for estimating geoacoustic properties of the seabed and detecting changes in those properties due to accumulation or dissociation of gas hydrates. Since the data collected at AV14 were of very poor quality due to instrument failures, only the data from MC798 are considered in this research.

The MC798 study area is situated along the upper continental slope of the northern Gulf of Mexico on the western flank of the bathymetric feature known as Mississippi Canyon – an offshore extension of the Mississippi River channel (Fig. 3.1). The area is characterized by complex geologic and bathymetric features, which pose significant challenges to the application of matched-field inversion. Despite this drawback, MC798 is within reasonable proximity to various Gulf coast seaports, it had no leaseholder from which to obtain permission for seafloor activities, and there are gas hydrates present [72, 73], making it a likely site for the remote gas hydrate observatory at the time of the cruise.

A schematic diagram of the VLA is shown in Fig. 3.2. The array consists of 16 hydrophones spaced at 12.5 m intervals suspended in the water column by glass-sphere floats at the top, and anchored to the seafloor by an expendable concrete weight at the bottom. The electronics are contained in pressure housings near the base of the array. The data acquisition and telemetry system (DATS) within the data logger allows the array to record data autonomously, digitizing the hydrophone signals to 16 bits at 10 kHz sampling rate. A record of up to 10 s can be recorded and stored to the hard drive following each shot. The DATS is connected to a two-way acoustic modem allowing communications to the surface to start and stop recording, adjust the hydrophone gains, transmit data for quality analysis, and monitor the health of the system. An upward looking acoustic doppler current profiler (ADCP) is mounted on the array to determine the speed and direction of currents in the water column. The array is recovered by triggering one of the acoustic releases that detach it from the anchor allowing the buoyancy from the glass spheres to bring it to the surface.

During the survey in the MC798 study area, the VLA was deployed in  $\sim 800$  m of water and acoustic data were recorded for several source-tow tracks of approximately 10-km length, crossing over the array position. The array was programmed to record the hydrophone data at regular time intervals with a 6-s segment of data recorded every 18 s. Impulsive-source seismic data were acquired along each track using a



Figure 3.1: Map showing locations of VLA deployments in MC798 and AV14 during October, 2003 research cruise, and the current planned location of the remote gas-hydrate monitoring station in Mississippi Canyon, Block 118.

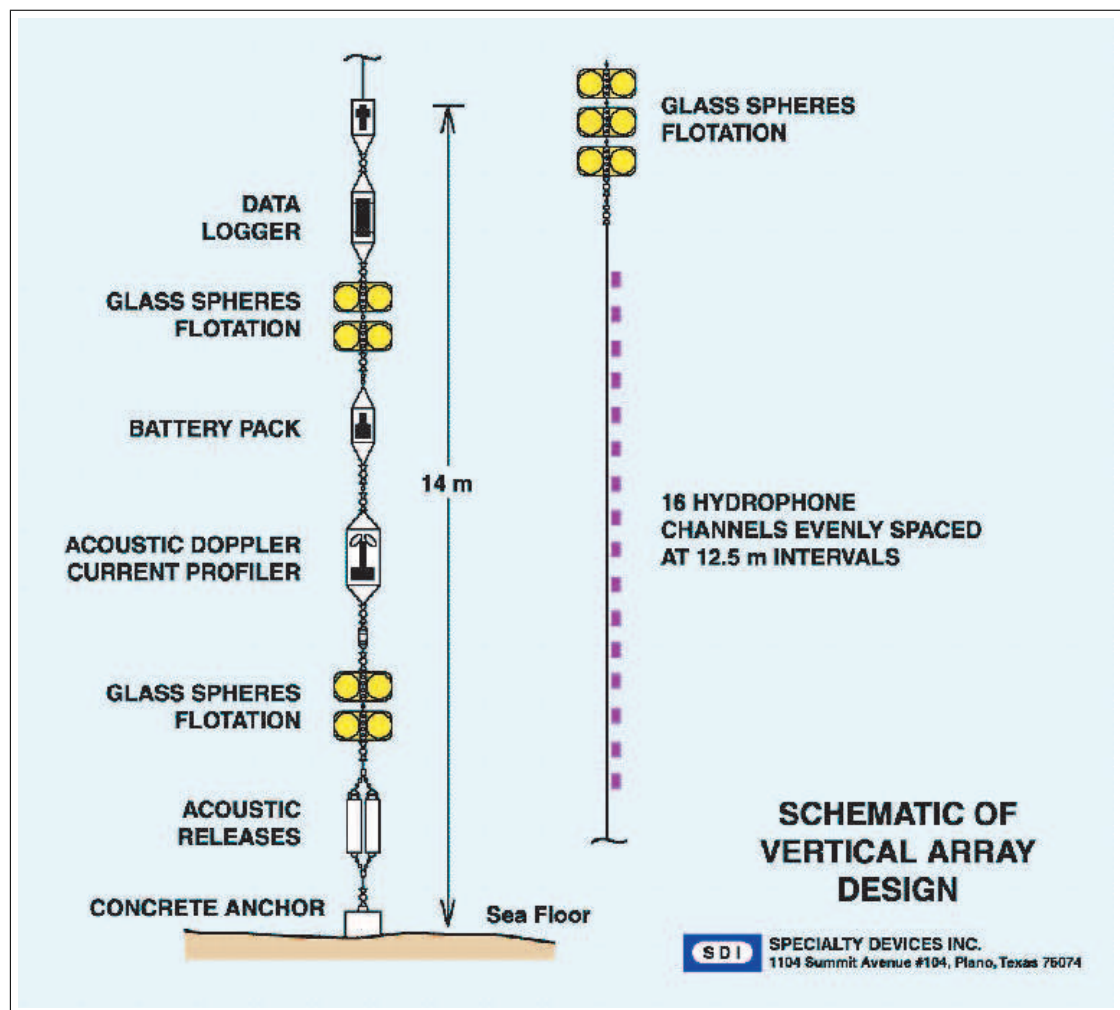


Figure 3.2: Schematic diagram of the VLA (courtesy Specialty Devices Inc.).

towed 80 in<sup>3</sup> water gun, and then the track lines were repeated without the water gun to record the ship noise from the *R/V Pelican*. The position at which the VLA was dropped from the ship, and the two ship-noise track lines that provided useable data (lines 1 and 2) are shown in Fig. 3.3. While collecting the ship-noise data, the *R/V Pelican* was traveling at maximum speed of  $\sim 10$  kts (5.4 m/s) in order to generate as much noise as possible.

Prior to collecting the acoustic data, measurements were made of the water column conductivity, temperature, and depth, from which the sound speed profile was computed (shown in Fig. 3.4). The current over the bottom  $\sim 60$  m of the water column was measured by the ADCP and found to be approximately 0.1 m/s in a southerly direction over the duration of the experiment. Seas were generally calm but waveheights occasionally increased to 1–2 m during the experiment.

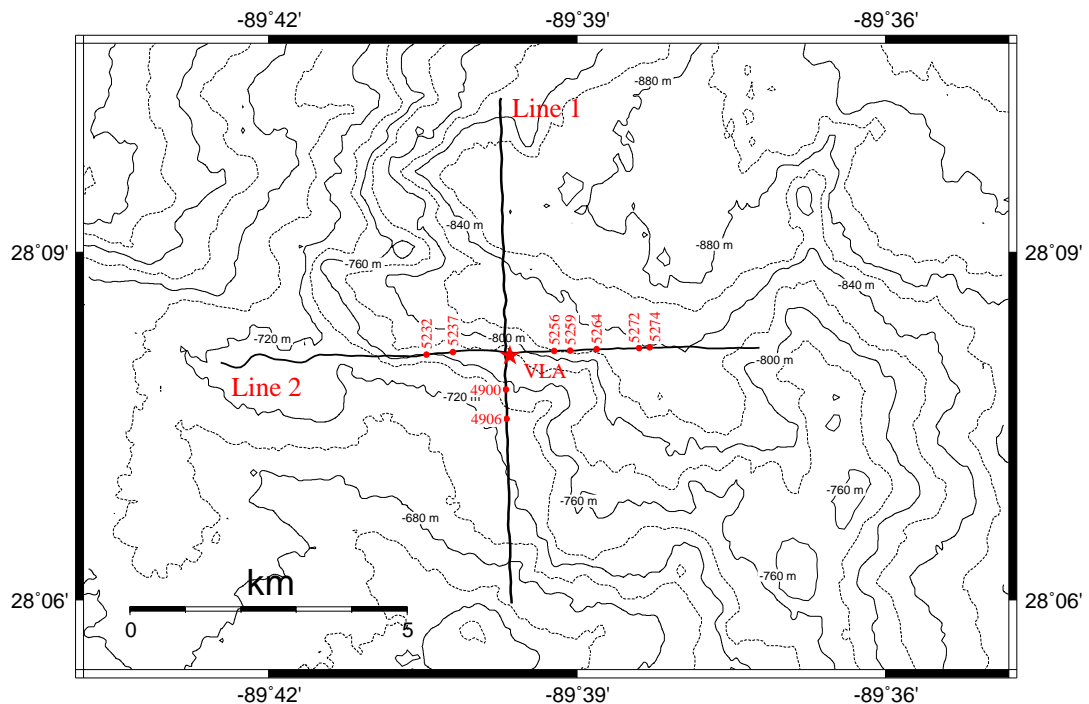


Figure 3.3: MC798 bathymetry showing tracks of *R/V Pelican* while recording ship noise data. The red star indicates the position where the VLA was dropped overboard. The ship location corresponding to data snapshots inverted by MFI are shown labeled with the data file identification numbers.

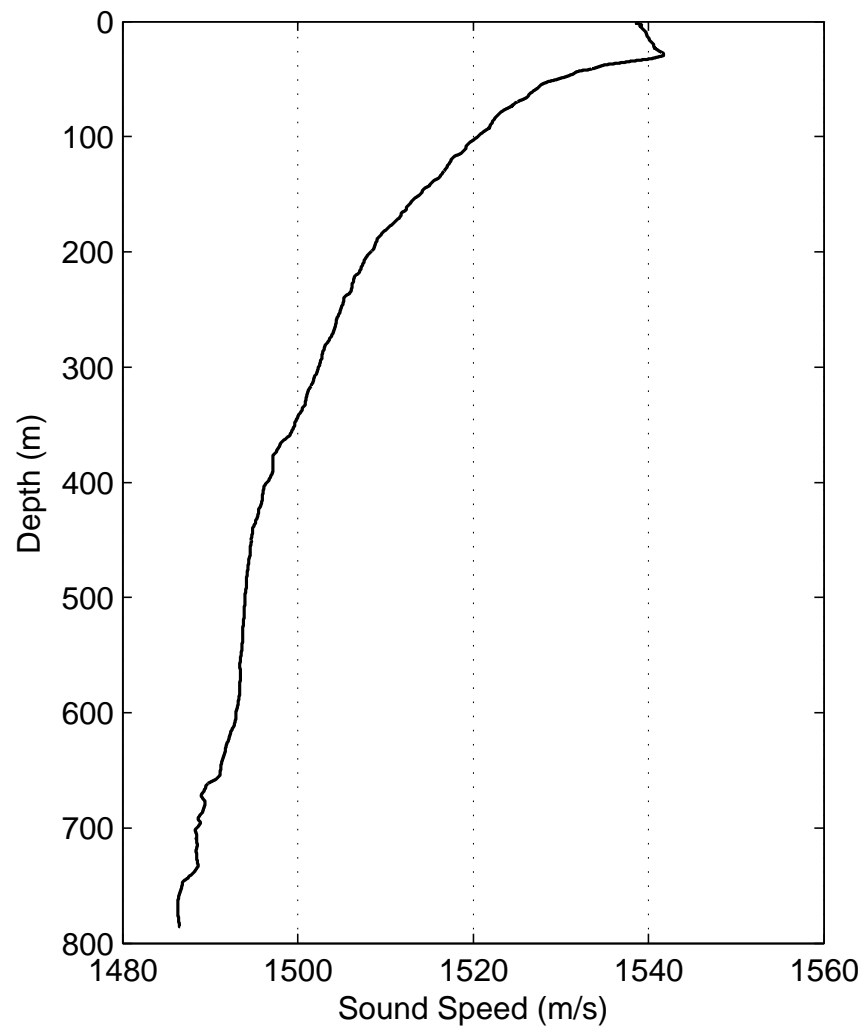


Figure 3.4: Water column sound speed profile in MC798.

## 3.2 Data quality

Upon examination of the data in the months following the 2003 research cruise, several problems were identified that severely impacted the quality of the data and its suitability for matched-field applications. The first and most obvious issue is the deep water and large variations in bathymetry at the survey site. Matched-field inversion generally becomes more sensitive to the properties of the seabed in shallow water (e.g., Refs. [42, 74]), although the sensitivity also depends on the shape of the water column sound speed profile, the source frequency, and the bottom type. The water depth at the array deployment position is  $\sim 800$  m which poses a significant challenge to using matched-field inversion for estimating geoacoustic bottom properties using a weak sound source at the sea surface. The survey was situated on the western flank of the Mississippi Canyon where bottom slopes were up to  $3^\circ$  in the vicinity of the array (see Fig. 3.3). This should necessitate using an acoustic forward model capable of handling range-dependent propagation (e.g., PE, adiabatic normal modes); however, computing the thousands of replica fields required in a matched-field inversion using one of these models would take a prohibitively large amount of time (especially in deep water and at higher frequencies).

In previous tests using the VLA, it was found that the amplitude of the direct arrivals from the water gun exceeded the dynamic range of the DATS causing the signal to be clipped at near offsets. In order to record an unclipped, far-field signature of the water gun for seismic post-processing, the gain on hydrophone channel 16 (uppermost) was purposely set lower than the others; however, this rendered the ship-noise data from this hydrophone unusable. Examination of the frequency spectra estimated from a sample of data recorded as the ship was near *endfire*<sup>1</sup> to the VLA revealed that hydrophones 1 and 8, located at the bottom and middle of the array respectively, were also unusable (Fig. 3.5). It is believed these hydrophones had

---

<sup>1</sup>Endfire refers to when the acoustic source location is along the same line formed by the hydrophones of a linear array.

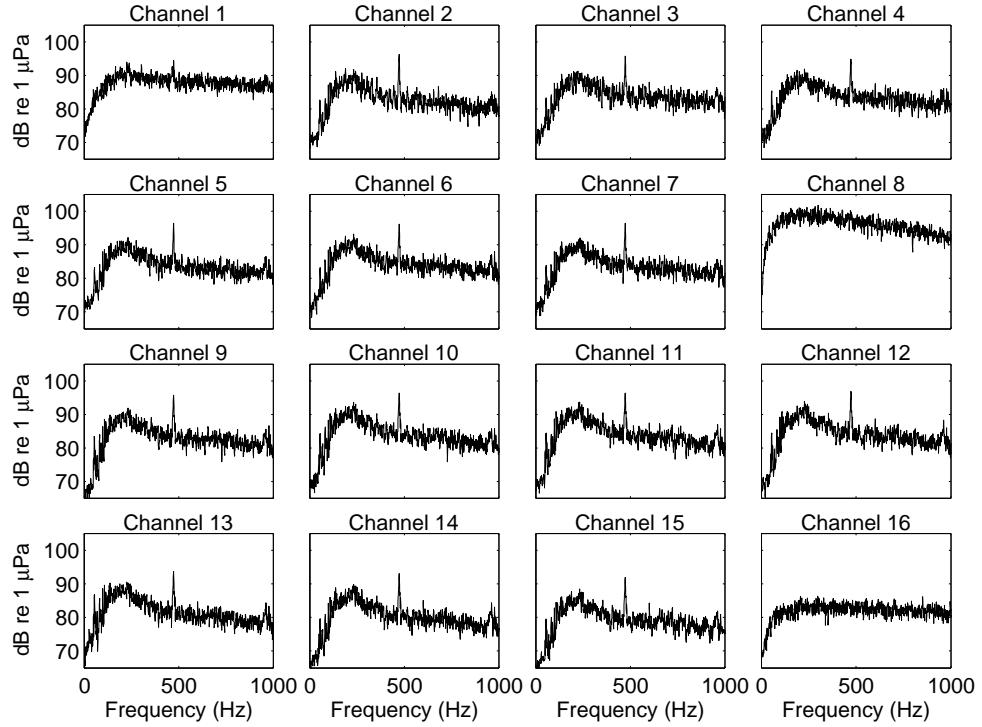


Figure 3.5: Relative spectra of ship noise data at each hydrophone with the ship at near endfire to the VLA along track-line 2.

water intrusion. The hydrophone spectra in Fig. 3.5 also exhibit an unexpected steep decline in spectral power below  $\sim 200$  Hz as if the data were low-cut filtered. Subsequent discussions with the manufacturer of the VLA revealed that there was an incorrect jumper setting on a circuit board in the DATS during acquisition that applied a low-cut filter to the data as observed. This loss of data restricts using low frequencies for MFI.

The *R/V Pelican* is a small research ship with a relatively quiet acoustic signature (i.e., in comparison to a large cargo vessel). Figure 3.6(a) shows that at the closest point of approach to the VLA position, the ship signal is approximately 15 dB above the estimated background level near 200 Hz. The background spectrum in Fig. 3.6 was estimated from a sample of data recorded when the ship was approximately 10 km away from the array position, and though it is not completely free of signal from the ship, it serves as a reference level to determine a signal to noise ratio (SNR) for the ship

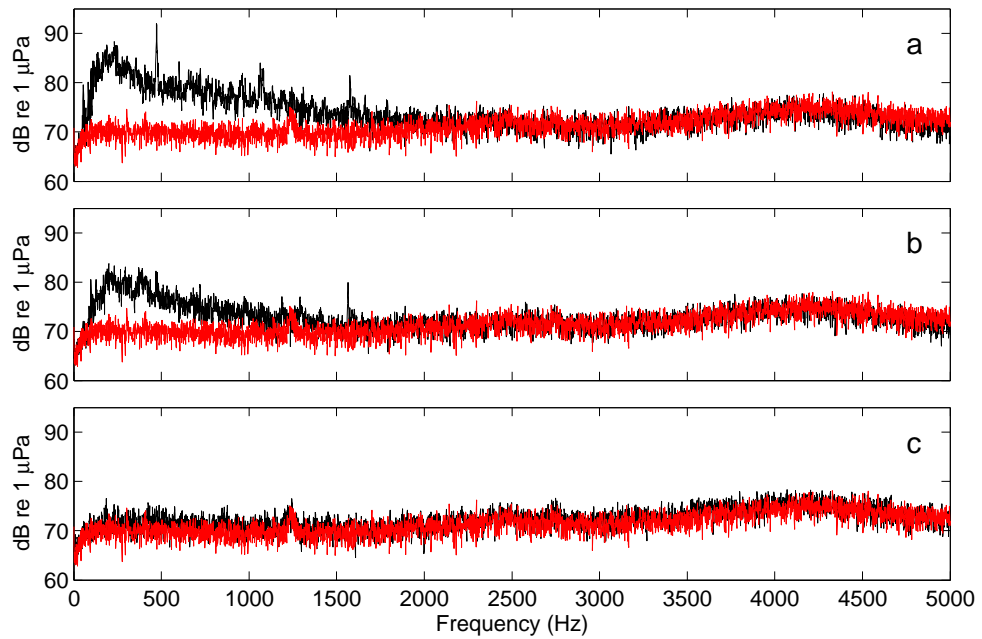


Figure 3.6: Plot showing spectral levels measured at the top of the array when the ship was present (black) versus background (red). In panel (a), the ship was nearly over the array position, (b) the ship was one water depth away, (c) the ship was three water depths away.

data. At a horizontal distance from the array equivalent to one water depth ( $\sim 800$  m), the SNR drops to  $\sim 10$  dB (Fig. 3.6(b)), and at three water depths ( $\sim 2400$  m) the ship signal is nearly indistinguishable from the background noise (Fig. 3.6(c)).

## Chapter 4

# Array element localization using ship noise

Prior to applying advanced array processing techniques such as matched-field inversion, it was necessary to determine accurate locations for the individual hydrophones of the VLA. AEL typically uses acoustic travel-times from a controlled source at several positions in an inversion to obtain accurate source and receiver locations. AEL inversion has been applied to estimate both source and receiver positions for a variety of experimental geometries using controlled sources [1–6, 75]. Acoustic travel-time measurements obtained from the water-gun data recorded in MC798 would normally have provided the information necessary for such an inversion; however, large, correlated timing errors and badly clipped direct arrivals made these data unsuitable. Alternatively, a method was devised to extract relative direct-arrival times from the broadband recordings of ship noise taken at multiple positions along the track lines shown in Fig. 3.3 by cross-correlating the time series between vertically separated hydrophone pairs. Cross-correlation techniques have been used in ocean acoustic applications such as surface-ship tracking [45], marine mammal tracking [76], geoacoustic inversion [46], and more recently to estimate Green’s functions between bottom moored hydrophones for positioning and time synchronization using ocean ambient

noise [77]. Array shape estimation has also been performed by a matched-field approach using the noise from ships of opportunity [44]; however, it does not appear that cross-correlation of ship noise data has been applied in an advanced AEL inversion to estimate source and receiver positions. In this work, relative arrival times determined from the cross-correlation processing are used as data in an AEL inversion based on the acoustic ray-tracing equations. The data are combined with prior information about the source and receiver positions to determine the hydrophone locations and to refine the source (ship) positions. A regularization constraint is applied to find the smoothest solution for the array shape and source tracks (e.g., Refs. [1–5, 7, 75]). Linearized estimates for the uncertainties of the recovered hydrophone positions are determined from the posterior model covariance matrix, and non-linear uncertainties are estimated by performing a Monte Carlo appraisal procedure [1, 7]. The details of this work are discussed in the following sections.

## 4.1 Ray tracing

In this section, the ray theory that is used to compute acoustic travel-times and partial derivatives in the AEL inversion algorithm is developed after Ref. [7].

AEL inversion is based on inverting the acoustic travel times between each source position  $(x_s, y_s, z_s)$  and receivers at  $(x_r, y_r, z_r)$  using a ray-tracing forward model [7]. The ray model is capable of including bottom and surface reflected ray paths; however, only direct rays are considered here. For a depth-dependent sound-speed profile,  $c(z)$ , the expressions for the path length and travel time along a ray path between a source and receiver are given by

$$r = \int_{z_s}^{z_r} \frac{pc(z)dz}{[1 - p^2c^2(z)]^{1/2}}, \quad (4.1)$$

$$t = t_0 + \int_{z_s}^{z_r} \frac{dz}{c(z)[1 - p^2c^2(z)]^{1/2}}, \quad (4.2)$$

where  $t_0$  represents the source transmission instant. In Eqs. 4.1 and 4.2,  $p = \cos \theta(z)/c(z)$  (where  $\theta(z)$  is the grazing angle) is the ray parameter which remains constant along the ray path and defines the take-off angle of the ray at the source. The eigenray that forms a direct path between a source and receiver is found by determining the value for the ray parameter,  $p$ , that gives the correct path length according to Eq. 4.1. The ray model [7] uses Newton's method to determine an appropriate value for  $p$ . An initial estimate,  $p_0$ , is found by assuming a straight-line ray path with constant sound speed representing the harmonic mean between the source and receiver,

$$c_H = (z_r - z_s) \left/ \int_{z_s}^{z_r} \frac{dz}{c(z)} \right. \quad (4.3)$$

A new value,  $p_1$ , is estimated by expanding Eq. 4.1 to first order in a Taylor series about  $p_0$  to yield,

$$p_1 = p_0 + \left[ \frac{\partial r(p_0)}{\partial p} \right]^{-1} [r(p) - r(p_0)]. \quad (4.4)$$

The partial derivative in Eq. 4.4 is found by differentiating Eq. 4.1 with respect to  $p$  giving

$$\frac{\partial r}{\partial p} = \int_{z_s}^{z_r} \frac{c(z) dz}{[1 - p^2 c^2(z)]^{3/2}}. \quad (4.5)$$

Equation 4.4 is solved iteratively, replacing  $p_0$  with  $p_1$  each time, until the value for  $r(p)$ , determined by Eq. 4.1, is within a specified tolerance limit of the actual range. Once  $p$  is determined, the travel-time along the ray path is evaluated according to Eq. 4.2.

The partial derivatives of Eq. 4.2 with respect to the unknown parameters  $(x_r, y_r, z_r)$ ,  $(x_s, y_s, z_s)$ , and  $t_0$  are also required for the inversion. Expressions for these derivatives are determined by applying the chain rule, e.g.,

$$\frac{\partial t}{\partial x_r} = \frac{\partial t}{\partial p} \frac{\partial p}{\partial r} \frac{\partial r}{\partial x_r} = \frac{\partial t}{\partial p} \left[ \frac{\partial r}{\partial p} \right]^{-1} \frac{\partial r}{\partial x_r}. \quad (4.6)$$

The partial derivatives for the horizontal coordinates of the source and receiver posi-

tions are thus [7]:

$$\frac{\partial t}{\partial x_r} = p(x_r - x_s)/r, \quad (4.7)$$

$$\frac{\partial t}{\partial y_r} = p(y_r - y_s)/r, \quad (4.8)$$

$$\frac{\partial t}{\partial x_s} = p(x_s - x_r)/r, \quad (4.9)$$

$$\frac{\partial t}{\partial y_s} = p(y_s - y_r)/r, \quad (4.10)$$

where Eqs. 4.1, 4.2 and the horizontal range between source and receiver,  $r = [(x_s - x_r)^2 + (y_s - y_r)^2]^{1/2}$  have been used. The partial derivatives of Eq. 4.2 with respect to the source and receiver depths are:

$$\frac{\partial t}{\partial z_r} = \frac{1}{c(z_r)} [1 - p^2 c^2(z_r)]^{1/2}, \quad (4.11)$$

$$\frac{\partial t}{\partial z_s} = \frac{1}{c(z_s)} [1 - p^2 c^2(z_s)]^{1/2}. \quad (4.12)$$

Finally, the derivative of Eq. 4.2 with respect to the source transmission instant,  $t_0$ , is

$$\frac{\partial t}{\partial t_0} = 1. \quad (4.13)$$

For the purposes of the AEL inversion, it is convenient to replace  $t_0$  in Eq. 4.2 by  $\bar{c}t_0/\bar{c}$ , where  $\bar{c}$  is a representative sound speed. This allows the unknown source instant to be represented as  $\bar{c}t_0$ , which has the same dimension (distance) as the other parameters, and can improve the numerical stability of the inversion algorithm. The partial derivative for  $t_0$  becomes

$$\frac{\partial t}{\partial \bar{c}t_0} = \frac{1}{\bar{c}}. \quad (4.14)$$

In order to implement the expressions above on a computer, it is advantageous to evaluate the integrals in Eqs. 4.1, 4.2, 4.3, and 4.5 numerically. Assuming that

the continuous sound-speed profile,  $c(z)$ , can be represented by a number of discrete layers,  $\{(z_k, c_k), k=1, N_z\}$ , with constant, non-zero gradients,  $\{g_k\}$ , these expressions become [7]:

$$r = \sum_{k=j}^{i-1} \frac{w_k - w_{k+1}}{pg_k}, \quad (4.15)$$

$$t = t_0 + \sum_{k=j}^{i-1} \frac{1}{g_k} \left[ \log_e \frac{c_{k+1}(1 + w_k)}{c_k(1 + w_{k+1})} \right], \quad (4.16)$$

$$c_H = (z_r - z_s) / \left[ \sum_{k=j}^{i-1} \frac{1}{g_k} \left[ \log_e \frac{g_k(z_{k_1} - z_k) + c_k}{c_k} \right] \right], \quad (4.17)$$

$$\frac{\partial r}{\partial p} = \sum_{k=j}^{i-1} \frac{w_k - w_{k+1}}{p^2 g_k w_k w_{k+1}}, \quad (4.18)$$

where  $w_k \equiv (1 - p^2 c_k^2)^{1/2}$  and  $i$  and  $j$  correspond to the depth indexes of the receiver and source respectively.

Turning rays must be considered if a non-turning eigenray cannot be found for a particular source-receiver geometry. The turning ray search is initiated by using the average sound-speed gradient between the source and receiver depths as an indicator of the most likely ray take-off direction. This preferred direction is downward for the case of a positive average sound-speed gradient (upward refracting) and upward for a negative average gradient (downward refracting). Rays with turning points at the top boundary of each layer of the sound-speed profile (i.e. where  $p_k = 1/c_k$ ) are traced in the preferred direction until two rays, corresponding to consecutive sound-speed layers, are found that bracket the receiver position. The bisection method is then used to refine the eigenray and find the value of  $p$ . If no turning rays are found, the procedure is repeated with rays launched in the other direction.

Once the  $p$  value for the turning ray is found, the integrals along the ray path (Eqs. 4.1, 4.2, 4.3, and 4.5) must be evaluated. For a turning ray that propagates initially downward and turns in a positive gradient layer,  $l$ , the discretized equations

for the ray are [7]:

$$r = \sum_{k=j}^{l-1} \frac{w_k - w_{k+1}}{pg_k} + \frac{2w_l}{pg_l} + \sum_{k=l}^i \frac{w_k - w_{k-1}}{pg_{k-1}}, \quad (4.19)$$

$$t = t_0 + \sum_{k=j}^{l-1} \frac{1}{g_k} \left[ \log_e \frac{c_{k+1}(1 + w_k)}{c_k(1 + w_{k+1})} \right] + \frac{2}{g_l} \log_e \left[ \frac{1 + w_l}{pc_l} \right] \quad (4.20)$$

$$+ \sum_{k=l}^i \frac{1}{g_{k-1}} \left[ \log_e \frac{c_{k-1}(1 + w_k)}{c_k(1 + w_{k-1})} \right], \quad (4.21)$$

$$\frac{\partial r}{\partial p} = \sum_{k=j}^{l-1} \frac{w_k - w_{k+1}}{p^2 g_k w_k w_{k+1}} - \frac{2}{g_l p^2 w_l} + \sum_{k=l}^i \frac{w_k - w_{k-1}}{p^2 g_{k-1} w_k w_{k-1}}. \quad (4.22)$$

Similar equations can be derived for an initially upward propagating ray that turns in a negative gradient.

## 4.2 Linearized inversion

In this section, the linearized inverse theory that forms the basis of the AEL inversion algorithm is described after Ref. [7].

The AEL inverse problem described here consists of estimating the 3-D position variables  $(x, y, z)$  for  $N_r$  VLA hydrophones and  $N_s$  source (ship) positions by performing a linearized inversion of travel-time data using the acoustic ray theory described in Sec. 4.1. The data can consist of absolute travel times with known source transmission instants, relative travel times where the source transmission instants are unknown, or absolute travel times with an unknown, constant offset. In this study the data consists of the time differences between direct arrivals of broadband ship noise received at pairs of vertically separated receivers; hence, it is considered relative travel-time data. The  $N_s$  source instants coincide with the arrival time of the ship noise at a reference receiver and are included as explicit unknown parameters in the inversion.

The measured acoustic arrival times  $\mathbf{t}$  between the sources and receivers can be

written in vector form as,

$$\mathbf{t} = \mathbf{t}(\mathbf{m}) + \mathbf{n}, \quad (4.23)$$

where  $\mathbf{m}$  represents the unknown parameters (i.e.,  $x, y, z$  for both the sources and receivers, and  $t_0$ ), and  $\mathbf{t}(\mathbf{m})$  represents the acoustic travel times between the sources and receivers. The vector  $\mathbf{n}$  represents additive errors (noise) on the data with the assumption that the errors are due to independent, zero-mean, Gaussian-distributed random processes.

The inverse problem of estimating the model  $\mathbf{m}$  that best fits the data  $\mathbf{t}$  is functionally nonlinear. A local linearized estimate can be obtained by expanding  $\mathbf{t}(\mathbf{m}) = \mathbf{t}(\mathbf{m}_0 + \delta\mathbf{m})$  in a Taylor series to first order about a starting model  $\mathbf{m}_0$ . Rearranging terms, the expansion can be written

$$\mathbf{J}\mathbf{m} = \mathbf{t} - \mathbf{t}(\mathbf{m}_0) + \mathbf{J}\mathbf{m}_0 \equiv \mathbf{d}, \quad (4.24)$$

where  $\mathbf{d}$  represents the data modified by the known quantities  $\mathbf{J}$  and  $\mathbf{m}_0$ . In Eq. 4.24,  $\mathbf{J}$  is the Jacobian matrix of partial derivatives  $J_{ij} = \partial t_i(\mathbf{m}_0)/\partial m_j$ , derived in Sec. 4.1. Equation 4.24 represents a linear inverse problem that may be solved for  $\mathbf{m}$  by the method described below. Since nonlinear terms are neglected, the linearized inversion must be repeated iteratively until the solution converges.

The standard least-squares solution for linear inverse problems is determined by minimizing the  $\chi^2$  data misfit

$$\chi^2 = |\mathbf{G}(\mathbf{J}\mathbf{m} - \mathbf{d})|^2, \quad (4.25)$$

where  $\mathbf{G}$  is a matrix of the form

$$\mathbf{G} = \text{diag}[1/\sigma_i], \quad (4.26)$$

and represents a weighting by the data uncertainties (standard deviations),  $\sigma_i$ , as

suming the data errors are Gaussian distributed. Including both source and receiver positions as unknowns in the inversion leads to an ill-conditioned problem which cannot be solved by standard least-squares methods, even for an over-determined problem where the number of data exceeds the number of unknowns. This ill-conditioning can be stabilized by including independent prior information in the inverse problem. This is accomplished by minimizing an objective function  $\phi$  that includes the data misfit (Eq. 4.25) and regularization terms that impose constraints on the solution based on prior information about the model:

$$\phi = |\mathbf{G}(\mathbf{J}\mathbf{m} - \mathbf{d})|^2 + \mu_1 |\mathbf{H}_1(\mathbf{m} - \hat{\mathbf{m}}_1)|^2 + \mu_2 |\mathbf{H}_2(\mathbf{m} - \hat{\mathbf{m}}_2)|^2. \quad (4.27)$$

The last two terms in Eq. 4.27 are regularization terms representing the prior information typically available in AEL problems (described below). The variables  $\mu_1$  and  $\mu_2$  are trade-off parameters (Lagrange multipliers) which control the relative importance of the regularization terms in the minimization.

The first regularization term in Eq. 4.27 can be used to apply prior estimates for the source and receiver locations based on knowledge of the deployment procedure, where  $\hat{\mathbf{m}}_1$  is the prior estimate of these parameters and  $\mathbf{H}_1$  is a regularization matrix of the form,

$$\mathbf{H}_1 = \text{diag}[1/\delta_j], \quad (4.28)$$

where  $\delta_j$  is the estimated standard deviation of each prior parameter estimate assuming the uncertainties are Gaussian distributed. The second regularization term can apply the prior expectation that the array shape and/or source tracks are smooth functions of position  $(x, y, z)$ . This condition is implemented using  $\hat{\mathbf{m}}_2 = 0$  and  $\mathbf{H}_2$  consisting of the tridiagonal matrix with non-zero entries on the  $j$ th row given by

$$\mathbf{H}_{2j} = \text{tridiag} \left[ \frac{-1}{(u_{j+1} - u_j)^2}, \frac{u_{j+2} - u_j}{(u_{j+2} - u_{j+1})(u_{j+1} - u_j)^2}, \frac{-1}{(u_{j+2} - u_{j+1})(u_{j+1} - u_j)} \right], \quad (4.29)$$

where  $u_j$  represents the distance to the  $j$ th position along the array or source track. Each row of  $\mathbf{H}_2$  represents a discrete approximation to the second derivative operator  $\partial^2/\partial u^2$ . The term  $|\mathbf{H}_2(\mathbf{m})|^2$  provides a measure of curvature, and the regularization ensures that the solution has the simplest array shape and/or source track that is consistent with the data and prior parameter estimates. The smoothness criteria has been applied in previous AEL research with various array geometries [3, 4, 6], and it was applied to source tracks using data received by ocean bottom seismometers [78].

The regularized solution is obtained by setting  $\partial\phi/\partial\mathbf{m}=0$  leading to

$$\mathbf{m} = \hat{\mathbf{m}}_1 + [\mathbf{J}^T \mathbf{G}^T \mathbf{G} \mathbf{J} + \mu_1 \mathbf{H}_1^T \mathbf{H}_1 + \mu_2 \mathbf{H}_2^T \mathbf{H}_2]^{-1} [\mathbf{J}^T \mathbf{G}^T \mathbf{G} \mathbf{d} - \mathbf{J} \hat{\mathbf{m}}_1]. \quad (4.30)$$

From a starting model  $\mathbf{m}_0$  (usually coinciding with the prior estimate model  $\hat{\mathbf{m}}_1$ ), Eq. 4.30 is applied iteratively until convergence is achieved. Convergence is based on two criteria: fitting the data to a statistically appropriate level such that the non-linear  $\chi^2$  misfit achieves its expected value of  $\langle \chi^2 \rangle = N$  for  $N$  data, and achieving a stable solution in which the change in model parameters between successive iterations is small compared with the expected accuracy.

Assigning values to the trade-off parameters,  $\mu_1$  and  $\mu_2$ , to achieve a balance between the data misfit and the the prior information is a non-trivial procedure requiring a two-dimensional search. An efficient way of computing the trade-off values is described in [1, 3]. The search can be reduced to a one-dimension problem by setting

$$\mu_2 = \alpha \mu_1 \quad (4.31)$$

for a fixed value of  $\alpha$ , and determining the value of  $\mu_1$  at each iteration which yields the desired  $\chi^2$  misfit (discussed below). The value of  $\alpha$  is adjusted at each iteration based on a comparison of the parameter residuals,  $m_j - \hat{m}_j$ , and the estimate uncertainties,  $\xi_j$ . If the residuals are substantially smaller (i.e. a factor of 2) than the estimate uncertainties, then a smaller value of  $\alpha$  is required, and vice versa. The search is

repeated, replacing  $\alpha$  each time, until  $\sum_{j=1}^N \left( \frac{m_j - \hat{m}_j}{\xi_j} \right)^2 / N \sim 1$ .

Depending on the linearity of the problem and the choice of the starting model, the change in the model estimate between iterations may be too large for the iteration to converge to a solution. The trade-off parameter  $\mu_1$  is chosen to reduce the  $\chi^2$  misfit by an approximate, fixed amount at each iteration of the inversion until  $\chi^2 = N$  is achieved. Reducing  $\chi^2$  in this manner limits change in the model between iterations and stabilizes the convergence; however, more iterations may be required. At early iterations of the inversion an approximate value for  $\mu_1$  is sufficient and can be determined by a bisection method (since  $\chi^2$  increases monotonically with  $\mu_1$ ); however, near convergence one or more iterations of Newton's method is used to obtain a precise value for  $\mu_1$  [1].

For linear inverse problems with Gaussian-distributed errors and prior estimates, the model covariance matrix is given by

$$\mathbf{C} = [\mathbf{J}^T \mathbf{G}^T \mathbf{G} \mathbf{J} + \mathbf{H}_1^T \mathbf{H}_1]^{-1}. \quad (4.32)$$

For non-linear inverse problems solved using the iterated linearized approach described above, the covariance matrix can be approximated by Eq. 4.32 with the Jacobian matrix  $\mathbf{J}$  evaluated at the final model. While this approach generally provides a reasonable estimate of the model uncertainty for AEL inversion, a fully non-linear uncertainty estimate can be obtained by performing a Monte Carlo appraisal procedure; however, at a much greater computational cost. In this procedure, the source and receiver positions derived from the inversion of the measured data are assumed to define true positions for a synthetic inverse problem. Travel-time data are computed, and a series of independent inversions are carried out with different realizations of Gaussian-distributed, random errors added to the synthetic data, the prior position estimates, and starting model. The standard deviations of the additive errors are equivalent to the corresponding estimated uncertainties of the data and prior esti-

mates. The standard deviations about the true receiver positions are then computed from the ensemble of the inversion results. Both absolute and relative (sensor-to-sensor) uncertainties can be estimated using this approach.

### 4.3 Cross-correlation data processing

A sample of acoustic pressure data recorded by the VLA as the *R/V Pelican* transited along track-line 1 is shown in Fig. 4.1(a) (data for hydrophones 1, 8, and 16 were of poor quality and are not shown or analyzed here). Direct observation of coherent arrivals from the time series is difficult due to the continuous nature of the sound source. However, the time difference between arrivals of acoustic energy along the array can be extracted from the cross-correlation of signals recorded at pairs of receivers over the same time interval. The cross-correlation between signals  $p_i(t)$  and  $p_j(t)$  at hydrophones  $i$  and  $j$ , over a finite duration  $T$ , can be written as

$$R_{i,j}(\tau) = \sum_{t=0}^{T-1-\tau} p_i(t)p_j(t+\tau), \quad (4.33)$$

resulting in a vector of length  $2T-1$  as a function of the time delay,  $\tau$ , over the range  $-(T-1) \leq \tau \leq T-1$ . The values of  $\tau$  at the maxima of the correlation function correspond to the time delay of arrival of coherent acoustic energy between the receivers,

$$\Delta t_{i,j} = \text{Arg}_{\max}[R_{i,j}]. \quad (4.34)$$

Figure 4.1(b) shows the cross-correlation functions for several hydrophone pairs, derived from the data in Fig.4.1(a). Trace 1 represents the autocorrelation of the data received at hydrophone 2 (bottom of the array), and traces 2–14 are the cross-correlations between hydrophone 2 and the other hydrophones on the array. The cross-correlations are normalized such that the autocorrelation at time lag zero is unity. The maximum correlation occurs when one of the signals is time-delayed by

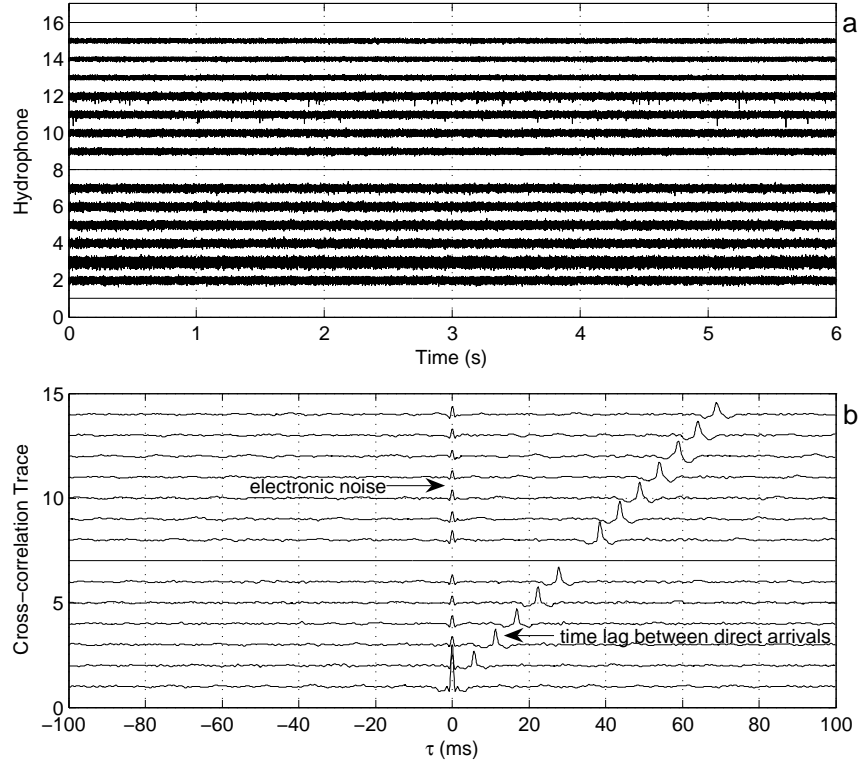


Figure 4.1: (a) Unfiltered time series of ship noise (hydrophones 1, 8, and 16 zeroed due to poor data). (b) Results of cross-correlation processing between each hydrophone and hydrophone 2. The time delay ( $\tau$ ) between the direct arrivals for each hydrophone pair increases uniformly from the bottom to the top of the array. Hydrophone numbers increment from the bottom of the array.

an amount equal to the difference between arrival times of the ship noise at the hydrophone locations. The time delay increases with the separation between the hydrophones. The peaks of the cross-correlation traces at  $\tau = 0$  (Fig. 4.1(b)) are an artifact of electrical noise common to all the receivers. The resolution of the cross-correlation function improves with the bandwidth and recording length of the data [77], and thus the broadband nature of ship noise is well-suited to this application. For data digitized at a sampling rate of  $f_s$ , the limiting resolution for the time-delay  $\tau$  is  $1/f_s$ .

The presence of tonal signals in the data that are not associated with the survey ship can degrade the correlation processing, introducing noise and false maximums

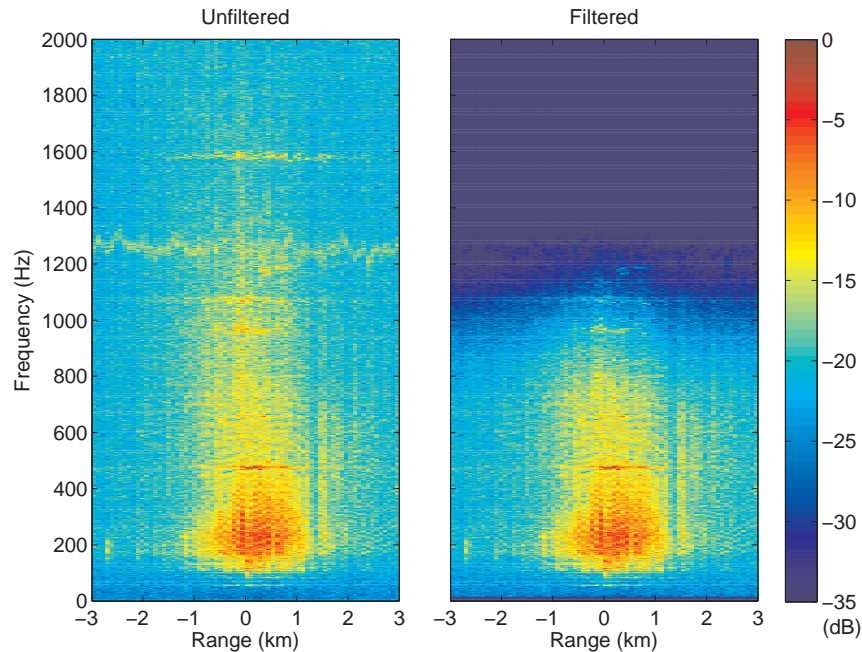


Figure 4.2: Spectrogram of unfiltered (left) and filtered (right) ship-noise data recorded for track-line 2. Decibel scale is normalized to maximum.

in the cross-correlation functions. Prior to computing the cross-correlation, the data were band-pass filtered to exclude signals outside the band containing the majority of the power of the ship noise spectrum. Normalized spectrograms of the acoustic data recorded for hydrophone 2 along track-line 2 are shown in Fig. 4.2. In the spectrogram of the raw data (left panel), the tonal band near 1250 Hz is not associated with the ship as the signal strength does not diminish with increasing distance from the array. After some experimentation, a filter with a pass band of 20–600 Hz and a 3dB/octave roll-off was found to yield a good balance between peak resolution and cancelation of noise in the cross-correlation functions. The spectrogram of the filtered data is shown in the right panel of Fig. 4.2.

A raster image showing the cross-correlation function for hydrophones 2 and 6 for all recordings along track-line 1 is shown in Fig. 4.3. The time delay of the direct arrival can be readily identified as a dark band in the image that moves out hyperbolically with range from the estimated array position. Faint bands can be

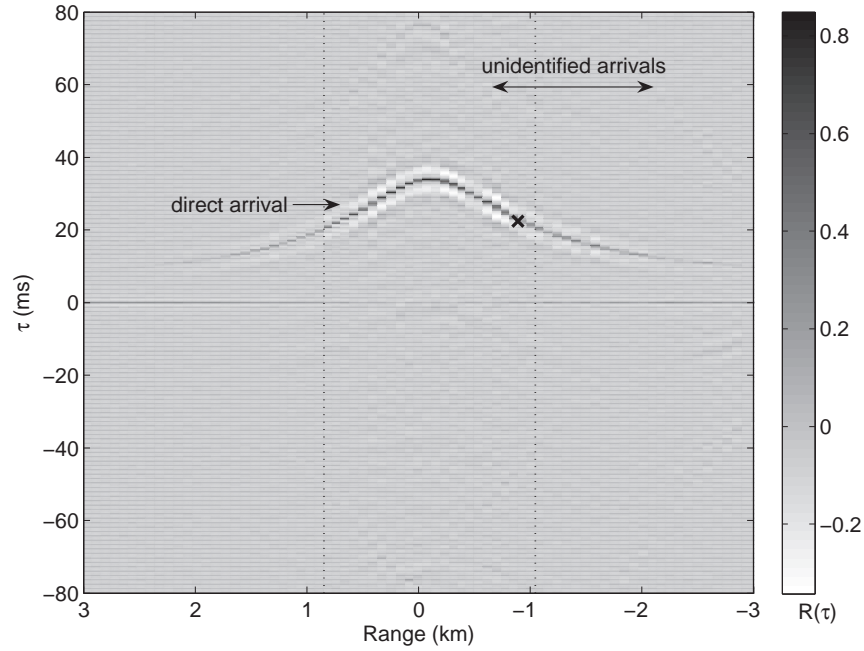


Figure 4.3: Raster image showing the correlation between the time series of hydrophones 2 and 6 for all ship-noise recordings of track-line 1. Dotted lines indicate the range of data used in the inversion. The  $\times$  indicates the data sample in Fig. 4.1.

observed at larger time delays in the image and may be associated with multi-path arrivals. If the path structures of these arrivals were identified, they could potentially be included in the inversion; however, in this case they were too weak to pick reliably and are not considered.

## 4.4 Results

Using hydrophone 2 as the reference receiver, cross-correlation functions were computed with all other hydrophones on the array (excluding 1, 8 and 16) for the two orthogonal ship track lines (see Fig. 3.3). The time delays corresponding to the maxima of the processed cross-correlation functions were found for multiple recordings of ship noise along each line. The data were picked for 13 receivers and 64 source positions over the two track lines (25 from track-line 1, and 39 from track-line 2) for a total

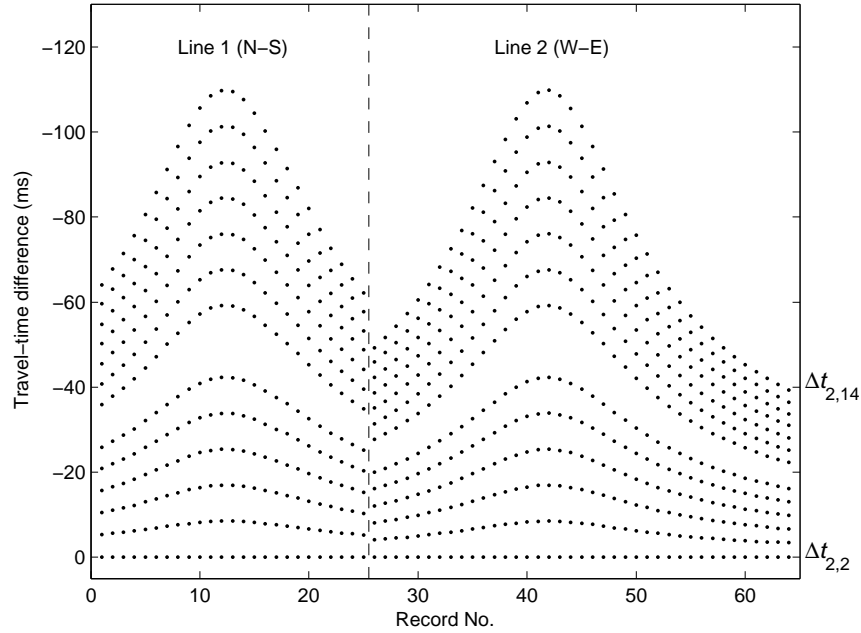


Figure 4.4: Relative travel-time picks from cross-correlation for all hydrophone pairs and both ship track lines.

of 832 data. Figure 4.4 shows the data picked from the cross-correlation functions for all hydrophone pairs used in the inversion. Since the acoustic energy propagates down the array, and the reference hydrophone is near the bottom of the array, the travel-time differences are negative. The time series were sampled at 10 kHz, giving a sampling interval of 0.1 ms along the time-axis of the cross-correlation functions. Based on the width of the peaks, the standard deviation of the errors on the picked relative travel-times were estimated to be 0.2 ms.

Prior estimates of the location of the array elements in  $x$  and  $y$  were obtained from the GPS position of the ship where the array was deployed and allowed to free-fall to the seafloor. The  $z$  coordinates were based on the chart water depth at this location and the nominal heights of the hydrophones above the array anchor. The horizontal coordinates of the ship and hydrophone locations were converted from geodetic coordinate system (WGS 84) to a planar coordinate system (UTM) and translated to make the prior array position the origin. The uncertainties of the

hydrophone position estimates were taken to be 1000 m in  $x$  and  $y$  and 100 m in  $z$ . These relatively large values apply more weight to the information provided by the data in the inversion, and less to the prior information.

The position of the ship at the start of each 6-s recording was extracted from the navigation data and corresponds to the location of the GPS antenna near the fore-aft centre of the vessel. Traveling at  $\sim 5$  m/s, the ship moved  $\sim 30$  m over a 6-s record and  $\sim 90$  m between records. To determine the position of the ship at the middle of each recording, the positions were interpolated between records, assuming the ship traveled in a straight line at a constant speed. Based on this procedure and the GPS accuracy, the uncertainties in the  $x$  and  $y$  coordinates of the source positions were estimated to be 15 m. The  $z$  coordinates for all source positions were estimated to be 3 m with an uncertainty of 3 m, based on the draft of the survey vessel.

The regularized inversion procedure described in Sec. 4.2 was applied to the data and prior estimates outlined above to estimate the unknown model consisting of the 3-D position variables  $(x, y, z)$  for each source and receiver, and the time offset,  $t_0$  for each source. For the case of relative travel-time differences between hydrophones obtained by the cross-correlation technique,  $t_0$  represents the time of arrival of the acoustic energy at the reference hydrophone. The data set yields 832 equations and 295 unknown parameters. The initial value assigned to the trade-off parameters,  $\mu_1$  and  $\mu_2$ , in Eq. 4.27 was 1000. Values for  $\mu_1$  were found that reduced  $\chi^2$  by a factor of  $\sim 5$  between iterations. The inversion converged to a solution in 7 iterations achieving a data misfit of  $\chi^2 = 831$  (the expected value is 832), which is more than 23 times smaller than the misfit computed for the starting model of  $\chi^2 = 19400$ .

The  $x$  and  $y$  locations of the VLA and several sources in the vicinity estimated from the inversion are shown in Fig. 4.5, along with the corresponding prior estimates (the position of the VLA is represented by hydrophone 2). The estimated location of the VLA is approximately 33 m east and 29 m south of its measured deployment position. Figure 4.6 shows the vertical array shape in  $x$  and  $y$  relative to the position

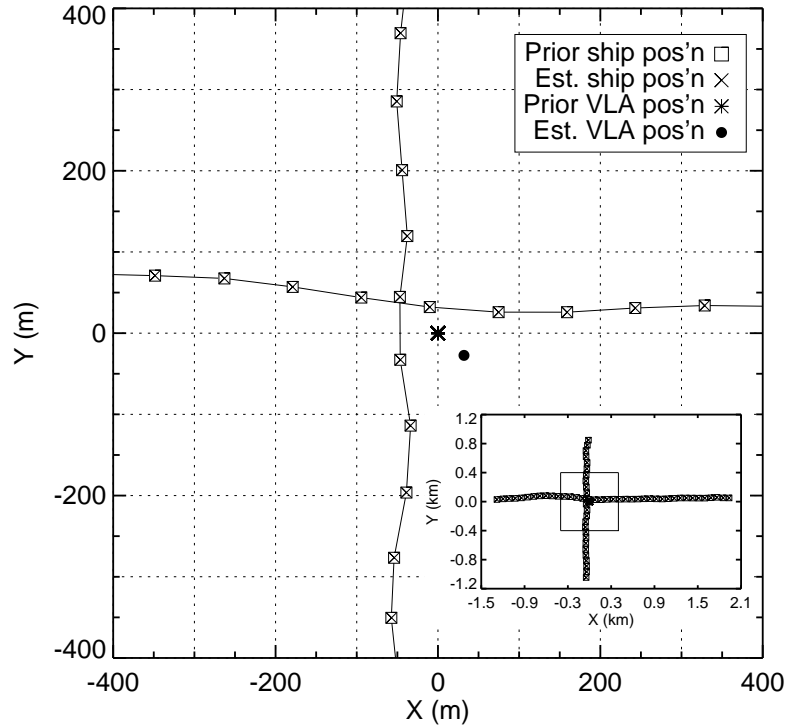


Figure 4.5: Plan view showing initial (prior) and recovered (est.) ship and VLA locations relative to the deployment position. Inset shows all ship positions.

of hydrophone 2, as well as the radial distance,  $R = \sqrt{x^2 + y^2}$ . The results indicate that the array is approximately 4 m shallower in depth than the prior estimate. Nominally, hydrophone element 2 is approximately 31.5 m above the array mooring; therefore, using the estimated  $z$  value of 737.3 m, the depth of the water at the array location should be 768.8 m. The water depth determined from the bathymetry data at the array position from the inversion is 769.0 m, indicating excellent agreement.

Figure 4.6 shows that the array is tilted  $\sim 5.5$  m toward the south-southeasterly direction over the portion of the array between hydrophones 2 and 14. This agrees with the average direction of the bottom current observed from the ADCP data. The array shape is smooth and physically reasonable. A slight curvature is apparent which is consistent with the expected hydrodynamic behavior of a moored VLA in the presence of a current. The final source locations did not move significantly from their initial estimates, likely because the data did not contain enough information to

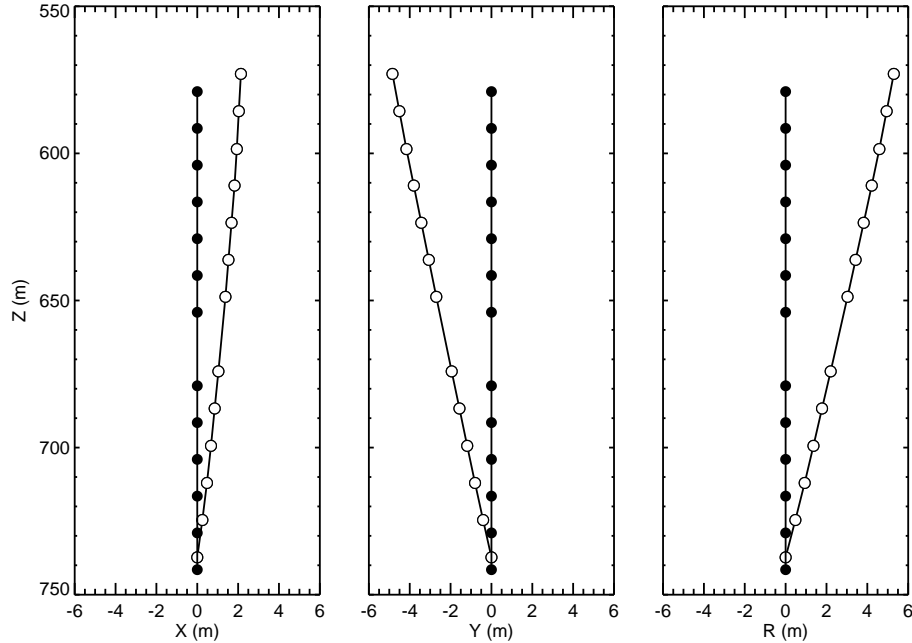


Figure 4.6: Vertical array shape in  $x$ ,  $y$ , and  $R$  from prior (solid circles), and recovered (open circles) estimates of receiver locations. Receiver locations are relative to hydrophone 2.

reposition both sources and receivers for this geometry.

The inter-element spacing from the AEL solution varied from 12.4–12.9 m with a mean of 12.6 m, compared to the nominal spacing of 12.5 m. The total distance between hydrophone elements 2 and 14 from the AEL solution is 1.9 m longer than the nominal length. As a check to see if the smoothing criteria stretched the array in order to minimize the curvature, the inversion was re-run without the smoothing regularization. There was almost no difference between the solutions, indicating that the regularization is not the cause of the apparent stretching. The VLA manufacturer indicated <sup>1</sup> that it is possible, under load, for the inter-element hydrophone spacings to stretch to as much as 12.6 m. It was also indicated that there may be some measurement error in the construction of the cable, and differences between the measured break-out points of the pigtailed and the positions the hydrophones were taped to the

<sup>1</sup>Personal communication with Paul Higley of Specialty Devices Inc.

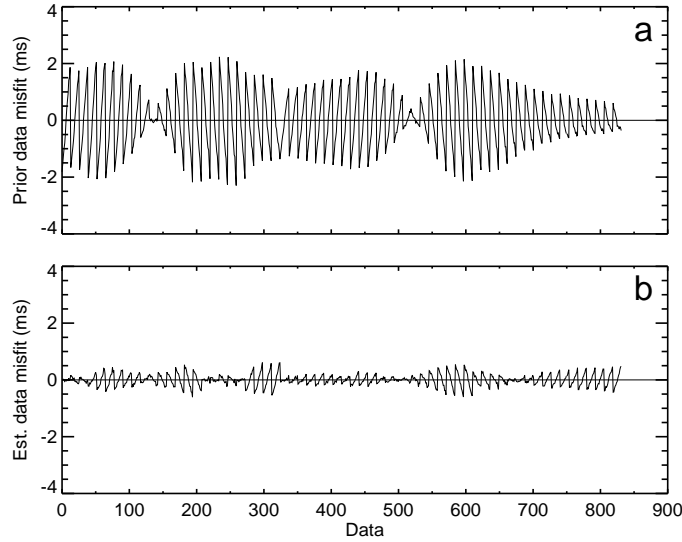


Figure 4.7: (a) Data residuals between the measured data and the data estimated from  $\hat{\mathbf{m}}$ . (b) Residuals between the measured data and the data estimated from  $\mathbf{m}$ .

cable just prior to deployment.

Figure 4.7(a) shows the differences between the measured data and the data computed for the prior model  $\hat{\mathbf{m}}$ , and Fig. 4.7(b) shows the differences between the measured data and the data for the final model  $\mathbf{m}$ . The data residuals are reduced from a maximum of 2.2 ms at the prior estimate to less than 0.6 ms at the final model. The regions with low values in the prior data residuals near data points 140 and 525 correspond to the ship passing (close to) over the array on track-lines 1 and 2 respectively. At this point the ship is near endfire to the array, and the relative travel-times are sensitive only to the vertical hydrophone separation; modest errors in the  $x$ - $y$  hydrophone positions for these source locations will not affect the data significantly.

The model uncertainties are examined in Fig. 4.8. Figure 4.8(a) displays the absolute uncertainties for the receiver positions estimated from the linearized inversion. The mean standard deviations are 4.3 m in  $x$ , 7.2 m in  $y$ , 1.8 m in  $z$ , and 8.6 m in

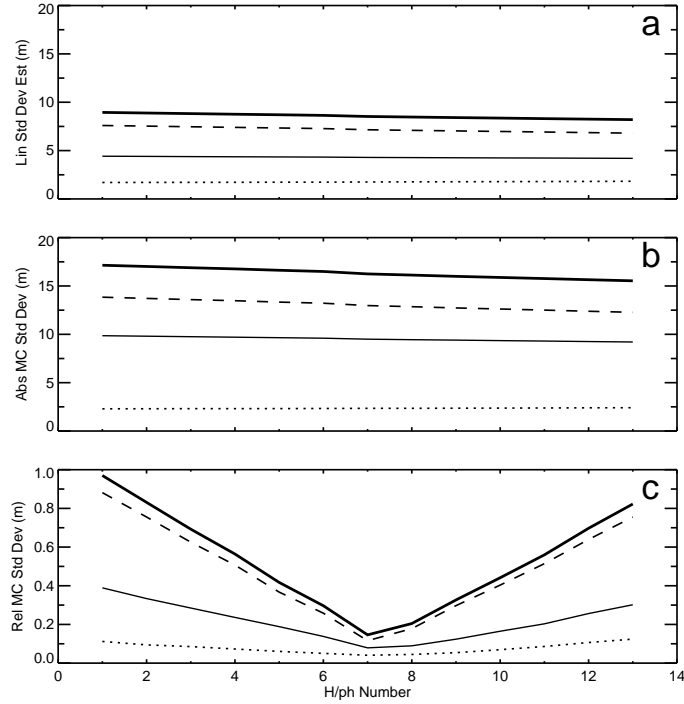


Figure 4.8: Array element uncertainty estimates in  $x$ ,  $y$ ,  $z$  and  $R$  indicated by solid, dashed, dotted, and heavy solid lines respectively. Linearized estimates of standard deviation (a), and absolute (b) and relative (c) standard deviations estimated by Monte Carlo appraisal.

$R$ , where  $R = \sqrt{x^2 + y^2 + z^2}$ . The uncertainties were also estimated using the Monte Carlo appraisal method described in Sec. 4.2 and are shown in Fig. 4.8(b) and (c). The appraisal involved 500 iterations of the inversion with random realizations of Gaussian noise added to the data, starting model and prior position estimates. The estimated standard deviations from the Monte Carlo analysis are 9.5 m in  $x$ , 13.0 m in  $y$ , 2.4 m in  $z$ , and 16.3 m in  $R$ . The linearized inversion underestimated the absolute model uncertainties in this case. The uncertainties shown in Fig. 4.8(c) represent the errors in position with respect to the other array elements with translation and rotation errors removed. The mean standard deviations of the relative uncertainties are 0.2 m in  $x$ , 0.5 m in  $y$ , 0.1 m in  $z$ , and 0.5 m  $R$ . The mean standard deviations in the source positions estimated by the Monte Carlo method are 11.3 m in  $x$ , 12.0 m in  $y$ , and 2.5 m in  $z$ , and are similar to the linearized estimates. These values are

slightly smaller than the prior uncertainties (15 m in  $x$  and  $y$ , and 3 m in  $z$ ).

## 4.5 Array geometry and source repositioning: synthetic case study

A somewhat novel aspect of this work is the application of the smoothing regularization to the unknown source positions along the tracks. The nature of most AEL experiments is such that the source positions are considered independent of each other; however, in this case the positions are extracted from continuous ship tracks and it is expected that the solution should minimize unrealistic zig-zags or jumps between adjacent positions. In the previous section, the measured data did not contain enough independent information to adjust the source positions due to the geometry of the experiment and limited spatial aperture of the array. Here, a synthetic study is performed to illustrate how source position estimates can be improved significantly in cases involving an array with horizontal aperture.

The geometry used for the synthetic example consists of nine equispaced receivers arranged in a box pattern on the seafloor as shown in Fig. 4.9. This configuration is similar to that of a geophysical experiment using ocean bottom seismometers. The array elements are 150 m apart at 800 m depth, and the centre of the pattern is offset from the intersection of the source tracks by 70 m in  $X$  and  $-120$  m in  $Y$ . A total of 64 source positions along two orthogonal tracks are used (simulating the MC798 experiment). The north–south source track is 2750 m long with 25 source positions, and the west–east source track is 4480 m long with 39 positions. A simple sine function with a 20 m amplitude was applied to the source tracks to simulate a meandering ship (Fig. 4.9).

Synthetic (relative) travel-time data were calculated for the source–receiver geometry described above with random errors added, drawn from a Gaussian distribution with standard deviation  $\sigma_d = 0.2$  ms. Prior estimates of the source positions were

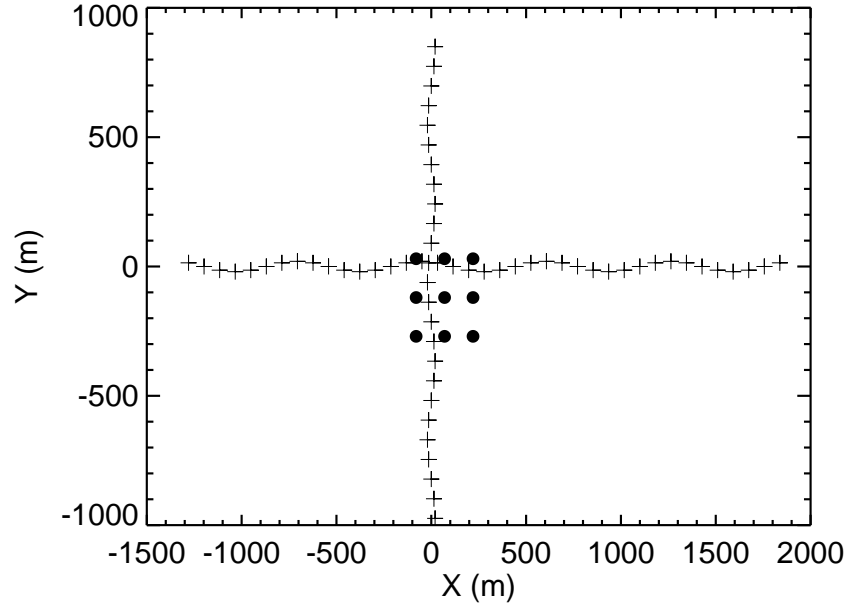


Figure 4.9: Source and receiver geometry for the synthetic example.

generated by adding random Gaussian errors with standard deviations of 15 m in  $x$ ,  $y$ , and 3 m in  $z$  to the true positions. The prior estimates of the receiver positions included errors with standard deviations of 25 m in  $x$ ,  $y$ , and 5 m in  $z$ .

The inversion was carried out with the data and prior source position uncertainties outlined above; however, the receiver position uncertainties in  $x$  and  $y$  were increased to 50 m. Figure 4.10 shows that both the source and receiver positions estimated from the inversion are significantly closer to the true positions than the prior estimates. Figure 4.11 shows that the absolute errors in the estimated source positions are generally less than the linearized estimates. This receiver geometry has a larger horizontal aperture compared to the VLA, and hence it provides more information about the source positions.

When the inversion was repeated without the source-track smoothing, the impact on the solution was negligible. To verify that the smoothing was indeed having an impact on the solution, the inversion was repeated with the errors on the data increased by a factor of 10 ( $\sigma_d=2$  ms). With this modification, the estimated source

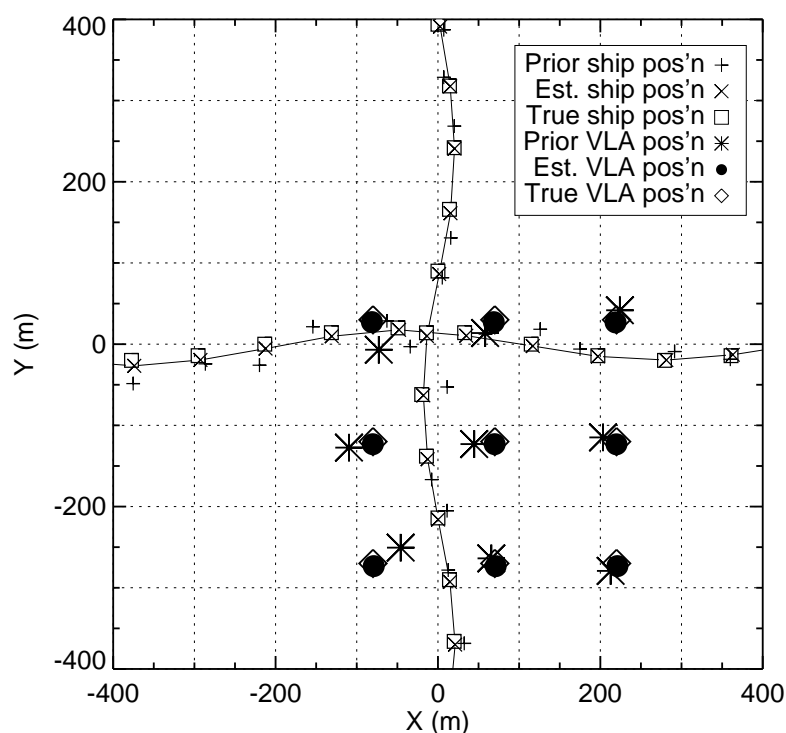


Figure 4.10: Plan view showing true, prior, and recovered (est.) ship and receiver locations for the synthetic example.

tracks are notably smoother than the prior tracks.

In a trial inversion, the receiver offsets were removed, making the geometry symmetric about the intersection of the source tracks. The inversion produced a poor solution in which the pattern of the receivers is severely skewed. The symmetry of this particular geometry leads to an east-west and north-south ambiguity in the data. The data at similar offsets on either side of the receiver pattern is nearly identical and hence redundant. Symmetries of this nature should be avoided in real-data experiments.

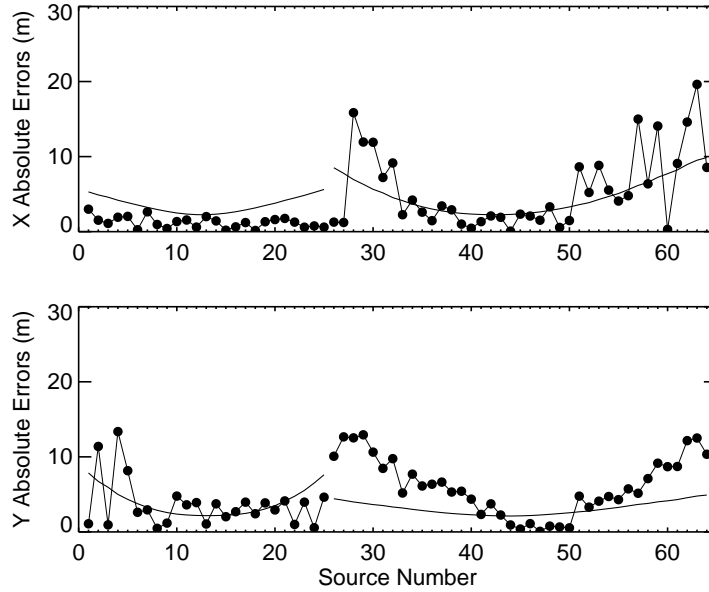


Figure 4.11: Absolute errors (solid circles) and linearized estimates (solid lines) for  $x$  and  $y$  coordinates of source positions.

## 4.6 Discussion

The AEL inversion provided a solution for the VLA location and shape that is consistent with available information. Using relative arrival times obtained from cross-correlations of time series of the hydrophone data allows a continuous, non-impulsive source such as the survey ship, or of a vessel of opportunity, to be used for localization. For practical considerations, the technique could potentially simplify the operation, reducing the time and costs of the survey, and, if implemented using ships of opportunity, allows the array elements to be positioned covertly.

The limited aperture provided by the VLA geometry diminishes the ability to adjust the source positions from their prior estimates; however, in a synthetic study it was shown that array geometries with some horizontal extent can improve source locations in addition to the array elements. Asymmetrical source tracks are best for avoiding ambiguity in the data which can lead to biases in the estimated receiver positions.

## Chapter 5

# Matched-field inversion using ship noise

Despite the problems with the MC798 data that were outlined in Chapter 3, matched-field inversion was applied to snapshots of data collected at a few ship positions in the vicinity of the VLA position. The data were first inverted using optimization (ASSA) to determine the MAP estimate of the solution, then Bayesian inversion (FGS) was applied to a subset of these data to examine the information content in the data and estimate geoacoustic model uncertainties. This chapter begins with a qualitative description of the typical features of a ship signature, followed by an outline of the data pre-processing steps applied to the MC798 ship-noise data. In the next two sections the results from optimization and Bayesian inversions using the data are shown. In the last section there is a brief discussion of the results.

### 5.1 Ship noise

The radiated noise from a ship is a complicated broadband signal containing a mixture of tones and continuous spectra. Reference [79] defines three major classes of ship noise – machinery noise, propeller noise, and hydrodynamic noise. Of these three,

machinery and propeller noise dominate the spectrum at most frequencies. Machinery noise originates from the ships engines, generators, bearings, shafts and vibrations from all other mechanically driven components onboard the ship. It contains tonal components from rotating and reciprocating parts, and a continuous component from sources of mechanical friction, turbulent flow of fluids through pipes, etc. Machinery noise can come from several locations inside the ship and is radiated into the water through the hull.

Propeller noise is composed of tonal components associated with the speed of rotation of the propeller blades and shaft, and a continuous component caused by cavitation. The tonal components include low-frequency blade lines plus higher frequency harmonics. The cavitation noise is a loud “hiss” that dominates the high frequency end of the ship noise spectrum, caused by the collapse of cavitation bubbles on the tips and surface of the propeller blades. Propeller noise originates outside the hull of the ship and tends to be weaker in the forward direction than broadside due to shadowing from the hull.

Hydrodynamic noise is generated by irregularities in the flow of water past the hull of the ship as it moves through the water. It is composed of *flow noise*, a normal characteristic of viscous fluid flowing around a body, noise from the wake of the vessel, and noise generated by the lapping and breaking of waves against the hull (particularly at the bow). Of the three classes of ship noise, hydrodynamic noise is generally much less dominant than machinery and propeller noise.

## 5.2 Data pre-processing

Spectrograms of the acoustic pressure data received at hydrophone 2 of the VLA as the ship transited along the west-east (line 1) and north-south (line 2) track lines in the MC798 survey area are shown in Fig. 5.1. The spectrograms were computed by averaging the spectra of several overlapping windows of data from each 6-s ship-noise

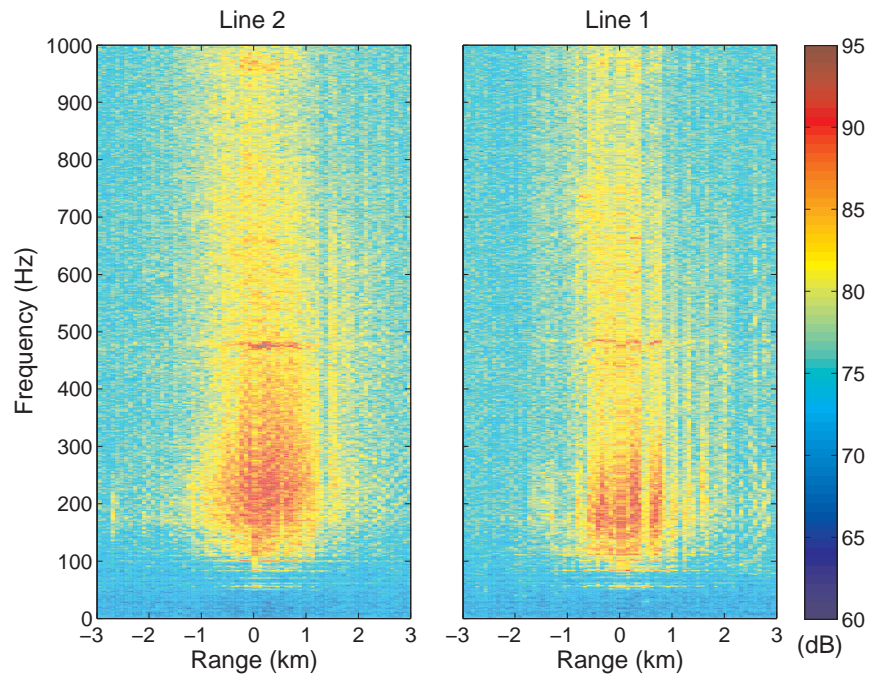


Figure 5.1: Spectrograms of signal received at hydrophone 2 as the ship transited along track-line 2 (left panel) and 1 (right panel). Spectral levels are not absolute. Negative range values indicate the ship was approaching the array and positive values indicate it is receding from the array.

recording and compiling each spectrum into a raster image as a function of horizontal distance from the array. Each 6-s record was divided into 1-s windows with a 50% overlap between adjacent windows. The data in each window were multiplied with a Hanning function then fast Fourier transformed to the frequency domain. The spectral power in each window was computed and then averaged over all the windows. The resulting spectra have a frequency resolution of 1 Hz and a Nyquist frequency of 5 kHz (at a sampling frequency of 10 kHz).

The spectra are dominated by the noise from the survey ship in the band between 50–500 Hz but may also include contributions from ambient noise sources such as wind generated noise at the at the sea surface, distant shipping, and seismic disturbances. The “bathtub” pattern observed in Fig. 5.1 is likely caused by the interference of the direct and bottom-reflected acoustic arrivals of the ship signal. The bathtub

pattern is more pronounced as the ship recedes from the array, than as it approaches. Anomalous vertical bands of muted spectral power are observed in these spectrograms that cut across all frequencies. After some investigation it was determined that these were not due to a naturally occurring field interference pattern or acoustic shadow zone, but were due to some error in the recording of the data. Judging from the spectrogram plots, the data for track-line 2 appear to have fewer of these signal dropouts and than for track-line 1. In general, the spectral levels appear slightly lower as the ship approached the array than as the ship receded from the array. This is likely due to the ship's hull shadowing some of the machinery and propeller noise in the forward direction.

The data from both track lines were sifted through to find recordings not affected by the muting described above and with higher SNRs and source-receiver offsets equivalent to one water-depth or more. The highest SNR occurs at the closest point of approach to the VLA; however, since sensitivity to geoacoustic parameters generally increases with the horizontal distance from the array (over the relatively short distance scales considered in this experiment), data samples for inversion were mostly restricted to be from one water depth or more in range. The map in Chapter 3 (Fig. 3.3) shows the approximate locations of the data samples selected for MFI.

The data for MFI generally consist of complex acoustic pressure vectors  $\mathbf{d}_f$  at the  $f$ 'th frequency across an array of hydrophones which are obtained from pressure time series by Fourier transform methods. The Bartlett objective functions in Chapter 2 were derived assuming the data were from a single time sequence of acoustic data, as is generally the case for impulsive sources. However, if it is reasonable to assume that the source signal is stochastic over the recording interval (e.g., a constant waveform source, or ambient noise), then the time-domain data can be sub-divided into a number of windows and averaged over the frequency-domain elements. Dividing the

data into  $K$  windows, the cross-spectral average is computed as

$$\mathbf{D}_f = \frac{1}{K} \sum_{k=1}^K \mathbf{d}_{f,k} \mathbf{d}_{f,k}^\dagger = \langle \mathbf{d}_f \mathbf{d}_f^\dagger \rangle, \quad (5.1)$$

where  $\mathbf{D}_f$  is the cross-spectral density matrix (CSDM) of the data  $\mathbf{d}_f$  which have been normalized to unit magnitude across the array (i.e.,  $\mathbf{d}_f = \mathbf{d}_f / |\mathbf{d}_f|$ ). The elements on the main diagonal of the CSDM are real-valued spectral powers of the received signal for each hydrophone, and the off-diagonal elements are the cross-power spectra between hydrophone pairs. An advantage to representing the data in this form is that coherent phase disturbances across the array are minimized (i.e., if the array were to bob up and down in the water). Secondly, time-window averaging of the received signals improves the SNR by suppressing uncorrelated noise [42].

To compute CSDMs for the samples of the ship-noise data selected for MFI, the 6-s ship noise records at each hydrophone were subdivided into 11 windows each of 1-s duration with a 50% overlap between adjacent windows. The data in each window were multiplied with a Hanning window and Fourier transformed to the frequency domain. A vector of the complex pressures across the array at each of the frequencies of interest was formed and normalized to unit magnitude across the array. Finally, a time-averaged CSDM was computed for each frequency according to Eq. 5.1. The three hydrophones (1, 8, and 16) that recorded poor data were omitted resulting in 13x13 element cross-spectral matrices.

### 5.3 Optimization inversion of ship-noise data

This section examines the results of several optimization inversions performed on a few selected snapshots of ship-noise data as the *R/V Pelican* transited along track-lines 1 and 2 of Fig. 3.3. The approximate locations of the ship corresponding to these data samples are shown in the figure and labeled with the file number of the

recording.

The frequencies of the data to be inverted were chosen by visual inspection of the ship-noise spectrograms. Upon close examination of the spectrograms (Fig. 5.1), prominent spectral lines are observable at frequencies of 56, 83, and 100 Hz with a broad peak at  $\sim 475$ –480 Hz. The inversions were performed at 6 frequencies from the set [56, 83, 100–101, 171–173, 199–200, 227, 300, 475–484] Hz which were selected after some experimentation. Frequencies corresponding to tones (e.g., 56, 83 and 100 Hz) and broadband noise near the peak of the spectrum (e.g., 200 and 300 Hz) are represented in this set. The exact combination of the frequencies used in each inversion varied for individual data snapshots. All data from track-line 2 were inverted using the frequencies [100, 171, 199, 227, 300, 476] Hz. Along track-line 1, data snapshot 4900 was inverted using the frequencies [56, 83, 100, 172, 200, 480] Hz and data snapshot 4906 was inverted using [56, 83, 101, 173, 200, 484] Hz

The optimization code ASSA was run for 1500 temperature steps with 10 random accepted perturbations at each step and a temperature reduction factor of 0.995. The mismatch function employed is based on the implicit form of the Bartlett (Eq. 2.34), modified to represent the data as CSDMs. The exact form of the mismatch function used is,

$$E(\mathbf{m}) = \sum_f \log_e[B_f(\mathbf{m})], \quad (5.2)$$

where

$$B_f(\mathbf{m}) = 1 - \frac{\mathbf{d}_f^\dagger(\mathbf{m})\mathbf{D}_f\mathbf{d}_f(\mathbf{m})}{|\mathbf{d}_f|^2}. \quad (5.3)$$

The forward model used in the inversion is the normal-mode model ORCA [68], run in the complex mode to include both the discrete and evanescent modes in the field calculations. Each inversion took approximately 12 hours running on a 1.8 GHz PC, with the computer coding done in FORTRAN.

The assumed form of the geoacoustic model consists of an ocean with the sound speed profile of Fig. 3.4 over a sediment half space. The environment is depicted in

Fig. 5.2. The model parameters inverted for are the source range ( $r_s$ ) and depth ( $z_s$ ), water depth ( $H$ ), and the sediment sound speed ( $c$ ), density ( $\rho$ ) and attenuation ( $\alpha$ ). Relatively wide search bounds for the geoacoustic parameters for  $c$ , and  $\rho$  were chosen (1450–1650 m/s and 1.1–1.4 g/cm<sup>3</sup> respectively) reflecting the limited information available about the seabed in the vicinity of the VLA, other than it generally consists of soft mud near the surface. The search bounds for  $\alpha$  were especially wide (0.001–2.0 dB/ $\lambda$ ) with the idea that the recovered estimates will represent both the in-situ attenuation of the seabed plus attenuation due to acoustic loss mechanisms such as scattering. The bounds for the water depth were 760–820 m which spans the minimum and maximum water depths between the source and receiver positions. Since the ship is known to be near the the sea surface and its positions are fairly well determined, the parameter bounds for source depth and range were kept relatively narrow (1–5 m and  $\pm 100$  m respectively). Though the true environment is range dependent, the inversions were performed assuming a range-independent model with the expectation that the recovered model parameters would represent some form of average of the range-dependent values. The validity of this assumption is investigated in Chapter 6 for a simple environment.

When the form of the geoacoustic model is unknown, it is common practice to invert for a simple model parameterization and then repeat the inversion with a larger number of sediment layers until an optimum parameterization is found based on the fit to the data (e.g., Ref. [80]). In this case, trial inversions for 2- and 3-layer parameterizations did not generally improve the data fit and hence a 1-layer model parameterization was considered to be sufficient.

Figure 5.3 shows the results of the ASSA optimization inversion for data snapshot 5259, when the ship was  $\sim 0.95$  km from the VLA along track-line 2. Each point in the plot indicates an accepted model perturbation and the corresponding value of the mismatch function at that model. The width of the envelope of accepted models in these plots provides a qualitative indication of the relative sensitivity of

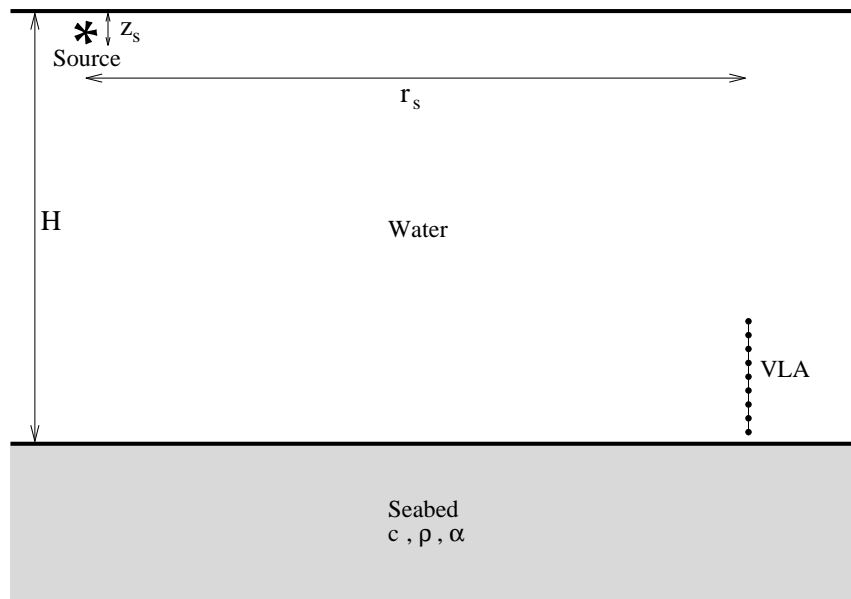


Figure 5.2: General form of the geoacoustic model assumed for MFI of ship noise data.

each parameter in the inversion. The most sensitive parameter is the source range, followed by the source depth; however, the geoacoustic parameters appear to be poorly determined as relatively small changes in the value of the mismatch function correspond to large ranges of possible values of the model parameters. The best-fit model parameters (MAP estimate) are indicated by dashed red lines. The value of the mismatch function at the MAP model is  $-6.4$  which corresponds to a normalized Bartlett mismatch of 0.36, averaged over the 6 frequencies.

The ASSA inversion results for data snapshot 5274 are shown in Fig. 5.4 where the source-receiver range is  $\sim 2.1$  km. Again, the source range appears to be the only parameter with any sensitivity in the inversion. The minimum value of the mismatch function for this data snapshot is  $-1.4$  (corresponding to a normalized Bartlett mismatch of 0.79), indicating a poor fit to the data.

The results of several inversions for data snapshots along track-lines 2 and 1 are summarized in Table 5.1. The second column indicates the value of the mismatch function at the best-fit model ( $E_{min}$ ). The estimated values for  $r_s$  are in good agree-

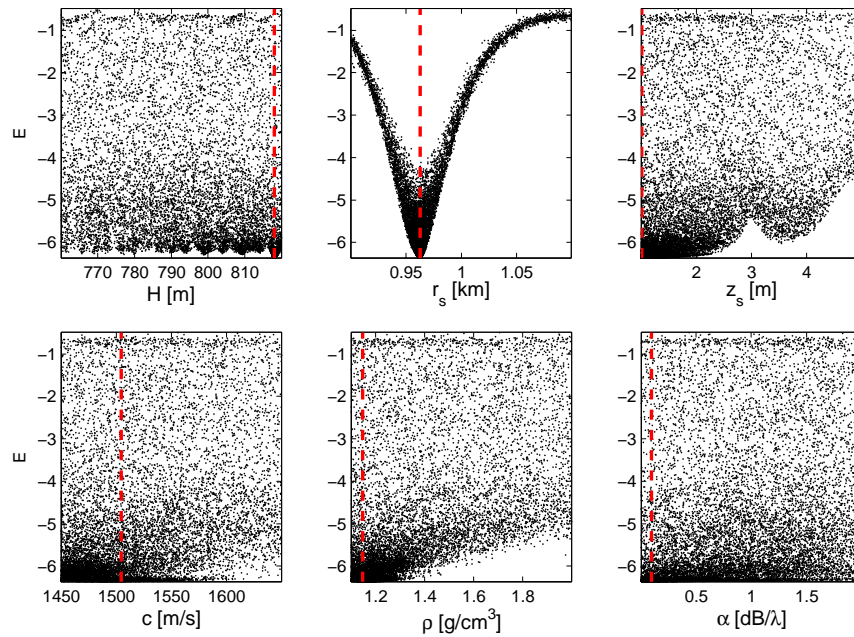


Figure 5.3: Results of optimization inversion of data from snapshot 5259 along track-line 2. The dashed red line indicates the optimum (MAP) model.

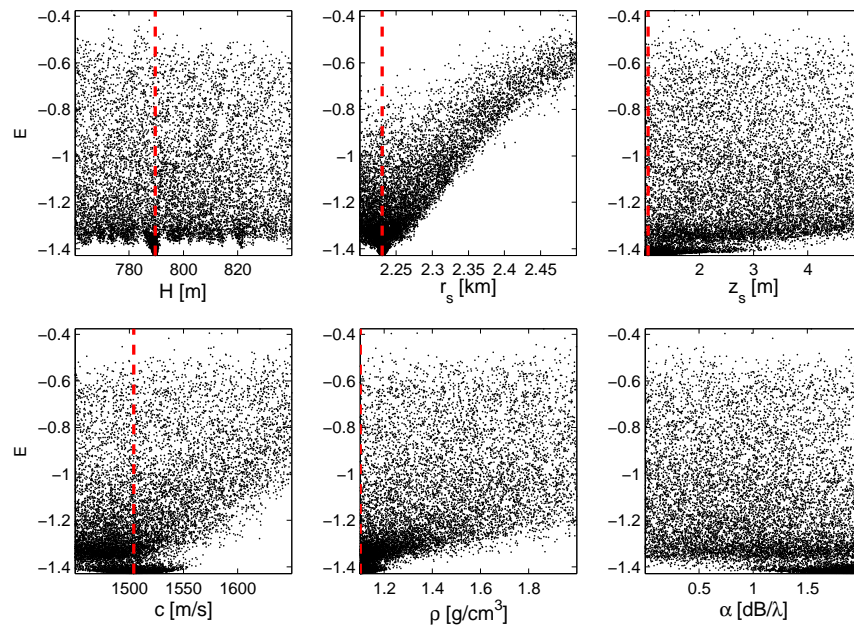


Figure 5.4: Results of optimization inversion of data from snapshot 5274 along track-line 2. The dashed red line indicates the optimum (MAP) model.

Table 5.1: Summary of optimization inversion results for several data snapshots along track-lines 1 and 2. The final column indicates the difference between the nominal source range from the AEL inversion and from MFI.

Data Snapshot	$E_{min}$	$c$ (m/s)	$\rho$ (g/cm <sup>3</sup> )	$\alpha$ (dB/ $\lambda$ )	$H$ (m)	$z_s$ (m)	$r_s$ (km)	$\Delta r_s$ (m)
Line 2								
5232	-2.84	1488	1.18	0.86	816	1.01	1.377	-94
5237	-4.88	1475	1.20	0.01	780	1.01	0.938	-77
5256	-7.05	1452	1.19	1.70	783	1.03	0.709	47
5259	-6.36	1505	1.15	0.09	818	1.01	0.963	46
5264	-4.23	1453	1.15	0.04	816	1.00	1.376	52
5272	-1.66	1532	1.40	0.05	814	3.09	2.056	48
5274	-1.43	1504	1.10	1.95	790	1.06	2.231	42
Line 1								
4900	-7.35	1487	1.15	0.04	835	2.25	0.519	55
4906	-6.45	1479	1.10	1.17	796	1.00	0.987	59

ment with the nominal values computed using the GPS position of the ship and the VLA position estimated by AEL inversion. There is a systematic difference between the values of  $r_s$  determined by MFI and nominal values. Specifically, the MFI estimates are consistently smaller than the nominal values as the ship recedes from the VLA and larger as the ship approaches. For the five inversions of data where the ship was east of the VLA (i.e., receding from the array) along track-line 2, the average source-range discrepancy is 47 m. Along track-line 1, the average distance of the two data snapshots (receding from the VLA) is 57 m. A significant source of the discrepancy between the AEL and MFI results is likely due to the fact that the majority of the ship noise comes from near the stern of the vessel, and the ship positions are referenced to the GPS antenna near midships. The sign of the source range discrepancy is consistent with this hypothesis. It isn't clear what is causing the difference in magnitude of the source range discrepancy from one side of the VLA to the other or between the different track lines; however, it may be due to the water depth mismatch and bottom slope which are known to bias source range estimates in

MFI.

The estimates for the sediment sound speed from all the inversions favour the lower end of the search interval which is consistent with a soft, muddy sediment. The values for density are consistently small and tend towards the minimum value in the search interval. It is likely that this is an artifact due to lack of information in the data rather than a true indication of the density. The estimates of the water depth and attenuation vary considerably from snapshot to snapshot.

## 5.4 Bayesian inversion of ship-noise data

The results of the optimization inversion do not appear to be very sensitive to any of the geoacoustic parameters of the seabed. To get a better idea of the amount of information contained in the data and to estimate the uncertainties in the model parameters, the Bayesian inversion algorithm FGS was applied to a couple of data snapshots.

The FGS algorithm described in Chapter 3 was run using data from snapshots 5259 and 5274 of track-line 2 in the form of CSDMs. The implicit form of the Bartlett mismatch function was used (Eq. 2.34). Each FGS run was initiated from the MAP model determined from ASSA for that data set (see Table 5.1). The convergence criteria for the pre-rotation stage in FGS was that the maximum difference between the correlation matrices computed from two different samples  $\epsilon_r$  should be less than or equal to 0.25. The sampling convergence criteria was that the difference between the marginal distributions of two independent samples was  $\epsilon \leq 0.05$ . Each inversion with FGS took roughly 24 hours to complete.

The 1-D marginal distributions of the model parameters were computed from the samples collected for data snapshots 5259 and 5274 and are plotted in Figs. 5.5 and 5.6 along with the MAP estimates and the 95% confidence intervals. These results are summarized together with the prior parameter bounds in Table 5.2. For data

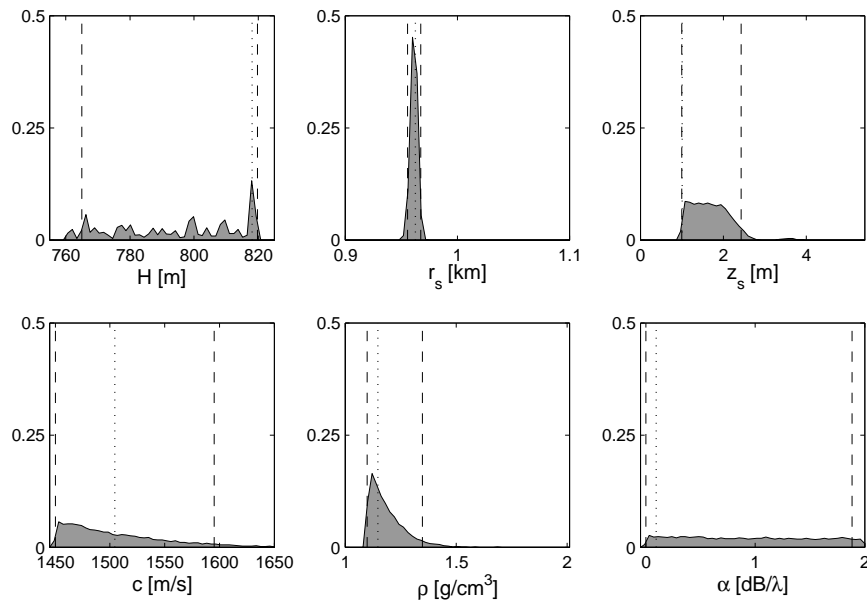


Figure 5.5: Results of Bayesian inversion of data from snapshot 5259 along track-line 2. The MAP model (dotted line) and 95% confidence interval (dashed lines) are indicated.

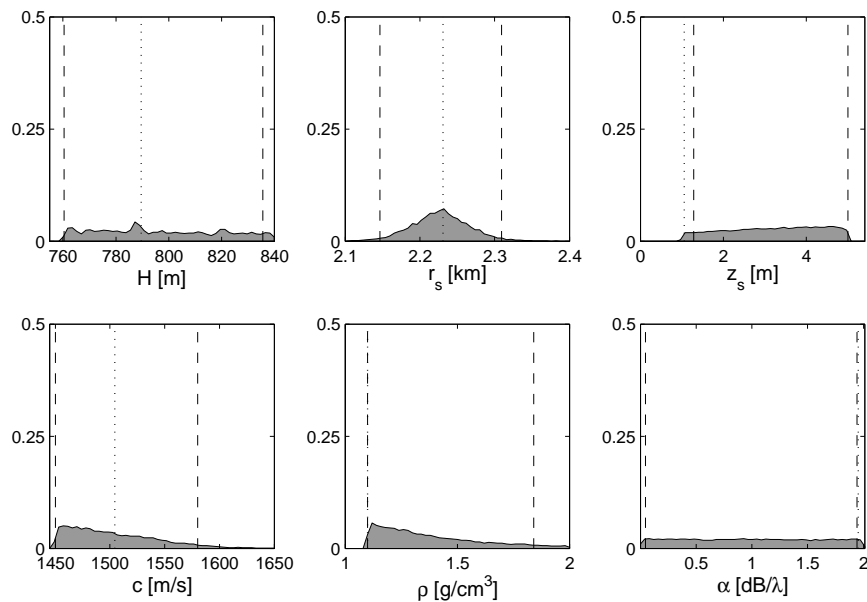


Figure 5.6: Results of Bayesian inversion of data from snapshot 5274 along track-line 2. The MAP model (dotted line) and 95% confidence interval (dashed lines) are indicated.

Table 5.2: Summary of Bayesian inversion results from the MC798 dataset showing the prior bounds, MAP estimates, and 95% confidence intervals (CI) for each parameter.

Parameter	Data Snapshot 5259			Data Snapshot 5274		
	Prior	MAP	95% CI	Prior	MAP	95% CI
$c$ (m/s)	1450–1650	1505	1450–1595	1450–1650	1504	1450–1580
$\rho$ (g/cm <sup>3</sup> )	1.1–2.0	1.15	1.10–1.35	1.10–2.00	1.10	1.10–1.84
$\alpha$ (dB/ $\lambda$ )	0.001–2.0	0.09	0.001–1.89	0.001–2.0	1.95	0.05–1.94
$H$ (m)	760–820	818	765–820	760–840	790	760–836
$r_s$ (km)	0.9–1.1	0.963	0.956–0.967	2.1–2.4	2.231	2.147–2.309
$z_s$ (m)	1.0–5.0	1.01	1.0–2.4	1.0–5.0	1.06	1.3–5.0

snapshot 5259, the source range is the only parameter that is well determined with a 95% confidence interval of 12 m. The water depth and the geoacoustic parameters (with the exception of density) are poorly determined with wide confidence intervals. In Fig. 5.5 the density appears to be somewhat well determined with a confidence interval of 0.25 g/cm<sup>3</sup>; however, this is likely not realistic. In most inversions, the values for density were driven towards the minimum of the search bound (see Table 5.1) which is likely due to some bias in the data. For data snapshot 5274, the source range was determined with a 95% confidence interval of 163 m; however, there is very little sensitivity to any other parameters.

## 5.5 Synthetic data example

In order to examine the “best-case scenario” for determining geoacoustic parameters by MFI in an environment similar to MC789, a synthetic study was performed with a similar experimental setup as the MC798 data set. The data were computed using the ORCA normal mode model for a range-independent environment consisting of a 769 m deep ocean with the MC798 water column sound speed profile over a sediment half-space. The sediment was based on a soft mud model with a sound speed of 1500 m/s, density of 1.4 g/cm<sup>3</sup>, and attenuation of 0.2 dB/ $\lambda$ . The data were generated for a

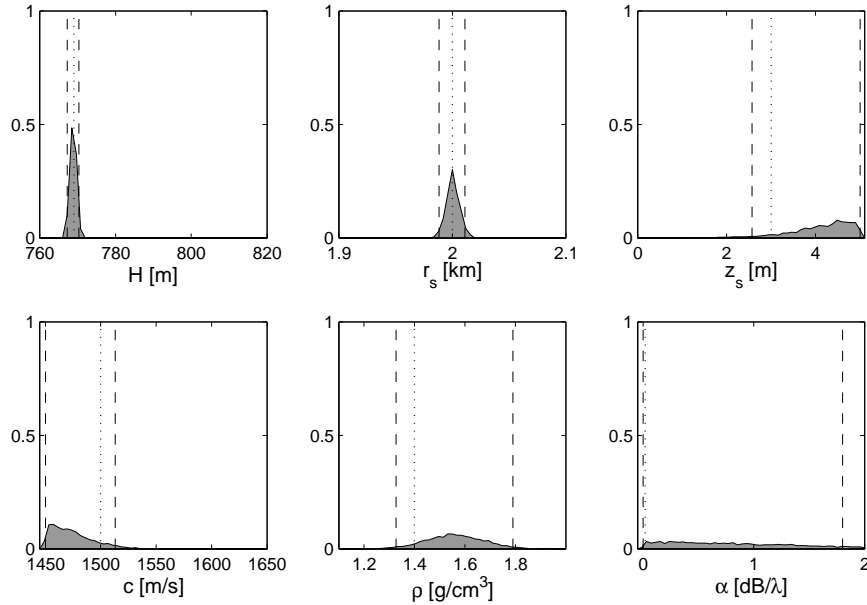


Figure 5.7: Results of Bayesian inversion of synthetic data for range-independent model of MC798. The true model (dotted line) and 95% confidence intervals (dashed lines) are indicated.

source at 2.2 km, and all 16 hydrophones of the VLA were used rather than only 13 as for the real data examples. Four frequencies were used and included some frequencies lower than those used for the real data inversions (i.e., [25, 50, 100, 200] Hz). Random noise drawn from a Gaussian distribution was added to the data to achieve an SNR of 5 dB.

The marginal distributions from the range-independent synthetic data inversion are shown in Fig. 5.7. As expected, the water depth, source range, and source depth are very well determined for the range-independent case. The distributions of the geoacoustic parameters for  $c$  and  $\rho$  are somewhat better than for the real data examples with 95% confidence intervals of 1450–1512 m/s and 1.32–1.79 g/cm<sup>3</sup> respectively.

## 5.6 Discussion

The results of the inversions of data from the MC798 cruise did not provide much information about the geoacoustic properties of the seafloor. The inversion results suggest that the seabed sound speed is less than  $\sim 1600$  m/s. The average value from all of the MAP estimates is 1486 m/s which agrees well with the results from sonic logs performed on a few shallow cores retrieved from the survey site <sup>1</sup>. Recent results of travel-time inversions of the water-gun data from the MC798 cruise indicate that the seabed sound speed in the vicinity of the VLA in MC798 is  $\sim 1480$ – $1510$  m/s and is fairly uniform down to about 40 m depth [81]. On top of the other issues impacting the data from this survey, the low impedance contrast at the ocean-seafloor interface reduces the sensitivity to the geoacoustic parameters obtained from MFI.

Despite many issues with the experiment and the data, the ranges to the ship source obtained by MFI were in good agreement with the positions estimated by AEL. The deep water, low SNR of the source, neglected environmental range dependence, short array aperture, and various problems with the data made the experiment less than ideal for determining geoacoustic parameters by MFI.

The results from an inversion of synthetic data for “ideal” experimental conditions (i.e., full array aperture and no range dependence) with a low-SNR source were somewhat better than for the real data; however, the sensitivity to seabed geoacoustic parameters is likely still too low to consider using MFI or MFP for monitoring purposes. Therefore, it is unlikely that matched-field techniques have the resolving power to detect spatial or temporal changes in the seabed due to changes in the distribution of gas hydrates.

---

<sup>1</sup>Personal communication with Carol Lutken at MMRI.

## Chapter 6

# Parameter estimate biases in geoacoustic inversion from neglected range dependence

In Chapter 5 the range dependence of the environment was neglected in the geoacoustic inversions in order to simplify the model parameterization. In this chapter, the impact of neglecting range dependence in MFI is examined.

### 6.1 Introduction

Due to the computationally intensive nature of MFI, most geoacoustic inversion work has been based on range-independent geoacoustic models, with the assumption that the recovered parameters represent some form of average over the actual range-dependent environmental properties. Lapinski and Chapman [28] examined this issue by considering a large number of range-independent inversions of synthetic acoustic data computed for range-dependent environments. Environmental range dependence was generated by adding random fluctuations to the seabed sound speed or water depth to achieve a desired mean and standard deviation over the propagation

range. The environment they considered was characterized by a high seabed sound speed (i.e., a hard bottom) and relatively rapid range-dependent fluctuations. They used a parabolic equation model to compute both the range-dependent acoustic data and the range-independent replica fields for MFI, and hence large computation times limited most of their work to single-frequency inversions. The results of their study indicated significant uncertainties in MFI results due to neglected range dependence, with reduced uncertainties for the one case considered which used two frequencies. Lapinski and Chapman [28] noted that the recovered parameter distributions included a bias, but did not consider the cause or pursue the observation beyond suggesting multi-frequency inversion as a possible remedy.

While considerable effort has been applied to optimization and uncertainty estimation in MFI, the issue of parameter biases has received little attention. Biased parameter estimates can result from inverting data that contain biased errors (i.e., random errors from a non-zero mean distribution). This chapter illustrates that neglecting environmental range dependence can lead to biased errors. In particular, for the simple environments considered here, random fluctuations in seabed sound speed or water depth tend to preferentially increase bottom loss. Neglecting this effect in MFI is equivalent to introducing biased theory errors in the data. This, in turn, results in biased parameter estimates, as the inversion adjusts parameters in an attempt to compensate for the increased loss (e.g., by choosing values that decrease the seabed reflection coefficient).

It is important to note that since standard MFI approaches are based (explicitly or implicitly) on the assumption of unbiased data errors, they are generally incapable of detecting such errors independently or of assessing their effect on parameter estimates. Statistical studies based on synthetic inversion results (where the true model is known for comparison) represent one of the few approaches to investigate quantitatively the effects on inversion of biased theory errors such as those that arise from neglected range dependence.

This chapter applies two approaches to examine biases introduced by neglecting range dependence in MFI. The first approach follows the methodology of Lapinski and Chapman [28] in carrying out ensembles of range-independent inversions of synthetic data generated for random range-dependent environments. For efficiency, range-independent replica fields are computed using a normal-mode propagation model, which allows a thorough investigation of the effects of multi-frequency data in the inversion. Further, the study considers range dependence of seabed sound speed and water depth for both hard- and soft-bottom environments. Different scales of lateral variation in water depth are also examined. The study indicates that significant biases in geoacoustic parameters can result from neglected range dependence. Although the variability of MFI results (e.g., the standard deviation about the ensemble mean) is reduced for multi-frequency inversion, parameter biases are not generally reduced, and are increased in some cases. Finally, the effects of neglected range dependence are shown to differ for different environments.

The second approach applies range-independent Bayesian inversion to synthetic data generated for range-dependent environments. The resulting uncertainty distributions are themselves found to be biased (i.e., distributed about biased parameter estimates), with no independent indication or estimate of the bias.

The remainder of this chapter is organized as follows. Section 6.2 describes the environments and propagation modelling. Section 6.3 presents the statistical results from ensembles of range-independent inversions for random range-dependent environments. Section 6.4 considers Bayesian geoacoustic uncertainty estimation with neglected range dependence. Finally, Sec. 6.5 summarizes and discusses this work.

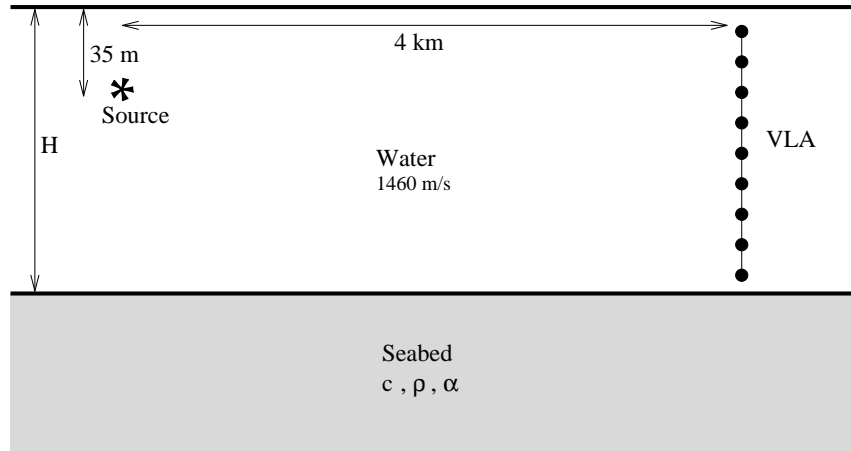


Figure 6.1: Base range-independent environmental model considered in this study.

## 6.2 Forward modelling

### 6.2.1 Geoacoustic model and range dependence

The environments considered in this paper are based on the model illustrated in Fig. 6.1, consisting of a water column of depth  $H = 80$  m and sound speed 1460 m/s over a semi-infinite seabed. Two different seabed types are considered. The hard-bottom case is similar to the environment in Ref. [28] based on a sand/gravel mixture representative of the Scotian Shelf with sound speed  $c = 1677$  m/s, density  $\rho = 2.06$  g/cm<sup>3</sup>, and attenuation  $\alpha = 0.436$  dB/ $\lambda$  ( $\lambda$  is wavelength). The soft-bottom case is typical of littoral regions of a sedimentary basin with average values of  $c = 1500$  m/s,  $\rho = 1.5$  g/cm<sup>3</sup>, and  $\alpha = 0.2$  dB/ $\lambda$ . The experiment geometry in both cases involves a source at 35-m depth and 4-km range from a 70-m vertical line array (VLA) of 71 sensors spaced at 1-m intervals from 5–75-m depth [28]. To generate environmental realizations with range-dependent seabed sound speed, random variations are added to the sound speed every 100 m in range. The perturbations are drawn from a uniform distribution, shifted to zero-mean and scaled to the desired standard deviation [28]. Several scales of range dependence are considered in Sec. 6.3, characterized by sound-speed standard deviations of  $\sigma_c = [0, 10, 20, 40]$  m/s, where  $\sigma_c = 0$  m/s corresponds

to the range-independent case.

Realizations of random range-dependent water depth with the desired mean and standard deviation are generated by summing a finite number of sinusoids [28] such that

$$H(r) = H + \sum_n A_n \cos(k_n r + \phi_n), \quad (6.1)$$

where  $A_n$  is the amplitude,  $k_n$  is the wave number, and  $\phi_n$  is the phase of the  $n$ th sinusoid. Values of  $\phi_n$  are drawn from a uniform random distribution on  $[0, 2\pi]$ ; values of  $A_n$  and  $k_n$  are calculated according to the power-law wavenumber spectrum method [28]. The bathymetry function,  $H(r)$ , is evaluated at 10-m range intervals and interpolated to the range-depth grid for the numerical propagation model (described below).

Two parameters control the scale of the water-depth fluctuations: the standard deviation,  $\sigma_H$ , which controls the vertical scale of the undulations; and the maximum wavelength,  $\lambda_{\max}$  (or minimum wavenumber,  $k_{\min} = 2\pi/\lambda_{\max}$ ), of the component sinusoids, which controls the horizontal scale. Larger values of  $\lambda_{\max}$  yield seabed realizations that vary more slowly with range while retaining the same mean and standard deviation. Examples of  $H(r)$  as a function of  $\lambda_{\max}$  are given in Fig. 6.2, which also shows the distributions of local slope angles of the seabed for 100 bathymetry realizations at each  $\lambda_{\max}$  value. Cases are considered in Sec. 6.3 for  $\sigma_H = [0, 0.125, 0.25, 0.5, 1.0]$  m and  $\lambda_{\max} = [0.5, 1.0, 1.5, 2.0, \infty]$  km, where  $\sigma_H = 0$  m and  $\lambda_{\max} = \infty$  km both correspond to the range-independent case.

## 6.2.2 Propagation modelling

The range-dependent data sets used in this study are generated using the PECan [69] parabolic equation propagation model described in Chapter 2. The PE model was used only to generate the range-dependent synthetic data and was not used to compute the replica fields in the inversion; thus, accuracy took precedence over compu-

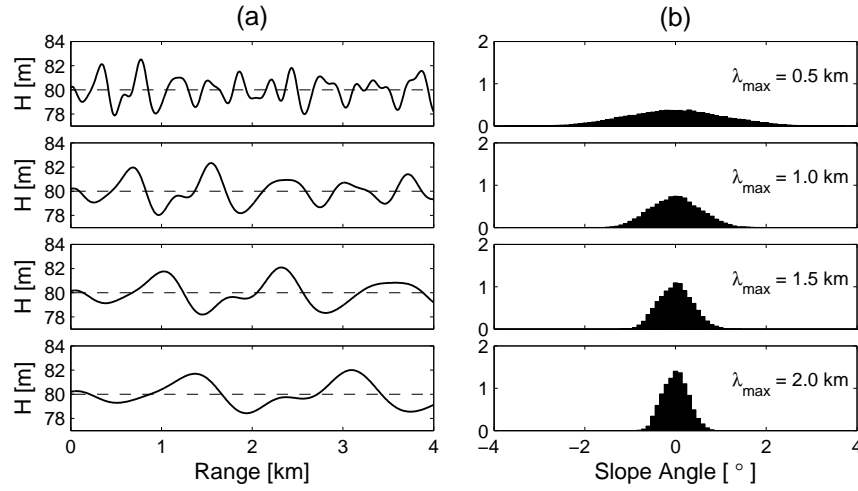


Figure 6.2: (a) Sample realizations of randomly varying bathymetry for different values of  $\lambda_{\max}$  with  $\sigma_H = 1.0$  m. (b) Distributions of seafloor slope angles from 100 random bathymetry realizations (normalized to unit area).

tation time for PE modelling. The replica fields in the inversions were computed using the (range-independent) normal-mode propagation model ORCA [68]. Prior to generating the range-dependent data, comparisons between the fields generated by the PE and normal-mode models for the range-independent environment were carried out based on the the normalized Bartlett mismatch

$$B_f = 1 - \frac{|\mathbf{p}_f^\dagger \mathbf{w}_f|^2}{|\mathbf{p}_f|^2 |\mathbf{w}_f|^2}, \quad (6.2)$$

where  $\mathbf{p}_f$  and  $\mathbf{w}_f$  are vectors of complex acoustic pressure along the VLA at the  $f$ th frequency from PECan and ORCA, respectively, and  $\dagger$  indicates conjugate transpose. The number of Padé terms ( $N_P$ ), grid spacing ( $\delta_z, \delta_r$ ), depth to the top of the absorbing layer ( $Z_\alpha$ ), and absorbing layer thickness ( $\Delta Z_\alpha$ ) were adjusted to achieve a good match between the propagation models. A summary of the mismatches between the PE and normal-mode fields over 100–800 Hz is given in Table 6.1. The mismatches between the modelled fields for the soft-bottom case are typically one to two orders of magnitude smaller than for the hard-bottom case. A mismatch of  $\sim 10^{-3}$  is sufficient

Table 6.1: Summary of PECan parameters used to generate range-dependent synthetic data. The normalized Bartlett mismatch between PE and normal-mode fields,  $B_f$ , is given for the hard- and soft-bottom environments in columns on left and right, respectively.

Freq. (Hz)	$N_P$	$\delta z$ (m)	$\delta r$ (m)	$Z_\alpha$ (m)	$\Delta Z_\alpha$ (m)	$B_f$ ( $\times 10^{-3}$ )	$B_f$ ( $\times 10^{-4}$ )
100	4	0.25	20	180	200	0.28	0.54
150	4	0.10	10	180	200	0.24	0.092
200	4	0.0625	10	180	100	0.24	0.16
250	4	0.0625	10	180	100	0.24	0.21
300	4	0.0625	10	180	100	0.72	0.34
350	4	0.0625	10	180	100	0.79	0.25
400	5	0.05	10	180	100	0.37	0.045
450	6	0.05	10	180	100	0.64	0.19
500	6	0.05	10	180	100	3.1	0.12
550	5	0.05	10	180	100	3.7	0.20
600	5	0.03125	10	180	100	3.1	1.1
650	5	0.03125	10	140	100	1.8	1.5
700	5	0.03125	10	120	100	1.0	1.1
750	6	0.03125	5	120	100	3.3	0.29
800	7	0.03125	5	120	100	1.5	0.52

for the purposes of this study, given that the noise added to the data prior to inversion produces mismatch values for the true model an order of magnitude larger than this (see Sec. 6.3).

## 6.3 MFI ensemble results

### 6.3.1 Methodology

MFI consists of finding the geoacoustic model that minimizes the mismatch between measured and replica fields. The model space can be large and complex, and an efficient search method is required to find the globally optimal solution. The method used here, adaptive simplex simulated annealing [22] (ASSA), is a hybrid inversion algorithm that combines the local downhill simplex method [58, 60] with the global-

search method of fast simulated annealing [63]. An important consideration for the present work is the variability of the inversion results caused by the search algorithm itself. A previous study concluded that ASSA achieved lower mismatch values with less variability in the solution than other methods typically applied in MFI (fast simulated annealing and genetic algorithms) [29].

Mismatch functions commonly used in MFI can be derived from maximum-likelihood methods [24, 30] based on the assumption that data errors are zero-mean, uncorrelated, Gaussian-distributed random variables. For single-frequency inversions, the likelihood-based mismatch function is equivalent to the normalized Bartlett mismatch, defined in Eq. 6.2, where  $\mathbf{d}_f$  and  $\mathbf{w}_f$  represent measured (PE) and replica (normal-mode) fields, respectively (this mismatch function was also used in Ref. [28]). For multi-frequency inversion, Ref. [28] used a simple average of Bartlett mismatches at the component frequencies, which is equivalent to assuming that the ratio of the data magnitude to its standard deviation is constant over frequency [24]. However, this assumption may not be valid since theory error due to neglected range dependence is likely frequency dependent; hence, this paper uses a more general likelihood-based mismatch function (Eq. 2.34) that allows for variation in errors from frequency to frequency [24, 30].

The effect of neglected range dependence is examined in the remainder of this section by carrying out range-independent inversions for 100 data sets generated for random, range-dependent environments. Spatially-white, zero-mean Gaussian noise is added to each data set to achieve an SNR of 20 dB at each frequency. The inversions estimate the geoacoustic parameters of the sediment ( $c$ ,  $\rho$ ,  $\alpha$ ) and the water depth ( $H$ ). Single-frequency inversions are performed using data at 100 Hz, and multi-frequency inversions use 15 frequencies at 50 Hz intervals from 100–800 Hz. To complete 100 multi-frequency inversions required  $\sim 16$  hrs on a 1.8 GHz PC running a *Linux* operating system.

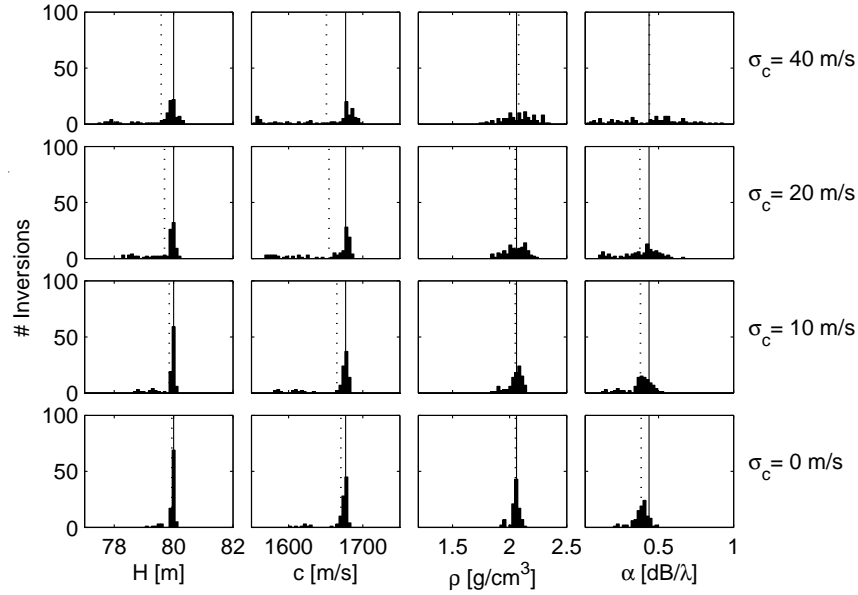


Figure 6.3: Parameter distributions from 100 single-frequency inversions of range-dependent sound speed environments for the hard-bottom case. The true mean (solid line) and distribution mean (dotted line) are included.

### 6.3.2 Range-dependent sound speed

#### Hard-bottom case

The distributions of the optimal models from 100 single-frequency inversions for the hard-bottom environment with range-dependent sound speed are shown in Fig. 6.3 for sound-speed standard deviations of  $\sigma_c = 0\text{--}40$  m/s. The results show considerable spread in the parameter values (even for the range-independent case,  $\sigma_c = 0$  m/s), with uncertainties increasing with  $\sigma_c$ . The cases  $\sigma_c = 20$  and 40 m/s were also considered in Ref. [28] with very similar results. The distributions from multi-frequency inversions for the same cases are shown in Fig. 6.4, which illustrates a substantial improvement over the single-frequency results. The range-independent case ( $\sigma_c = 0$  m/s) demonstrates that even with random noise on the data, the inversions consistently find values close to the true model parameters. The recovered parameters remain distributed near the true mean values for the range-dependent cases (with the exception

of  $\alpha$  at  $\sigma_c = 40$  m/s). However, as the range-dependence increases, small but systematic differences between the distributions and the true mean values are observed for the seabed parameters  $c$ ,  $\rho$ , and  $\alpha$ .

The results from the single- and multi-frequency inversions are summarized in Fig. 6.5, which shows statistical properties of the distributions (ensembles) of inversion results. The bias,  $b$ , represents the difference between the distribution mean and the true mean parameter value. The standard deviation of the distribution about its mean is denoted by  $\sigma$ , and the standard deviation of the distribution about the true mean value is denoted by  $\Sigma$ , with

$$\Sigma^2 = b^2 + \sigma^2. \quad (6.3)$$

The standard deviations in Fig. 6.5 are much smaller for all parameters for multi-frequency inversion than for single-frequency inversion. Further, the multi-frequency biases are significantly smaller for  $H$  and  $c$ , and generally smaller for  $\rho$  and  $\alpha$ . However, even for multi-frequency inversion, significant negative and positive biases are evident for  $c$  and  $\alpha$ , respectively, for large  $\sigma_c$ . A small negative bias also occurs for  $\rho$ , while  $H$  is essentially unbiased for multi-frequency inversion.

### Soft-bottom case

The results from multi-frequency inversions for the soft-bottom case are shown in Fig. 6.6. As the sound-speed range dependence increases, the distributions of recovered parameters become broader than for the hard-bottom case (Fig. 6.4), particularly for  $\rho$  and  $\alpha$  which also exhibit large biases. Note that for  $\sigma_c \geq 20$  m/s, all inversion results for  $\alpha$  are greater than the true value. Figure 6.7 summarizes the results for multi-frequency inversion (Fig. 6.6) and for single-frequency inversion (not shown). Substantially smaller standard deviations are generally achieved for multi-frequency inversion; however, significant biases remain for some parameters.

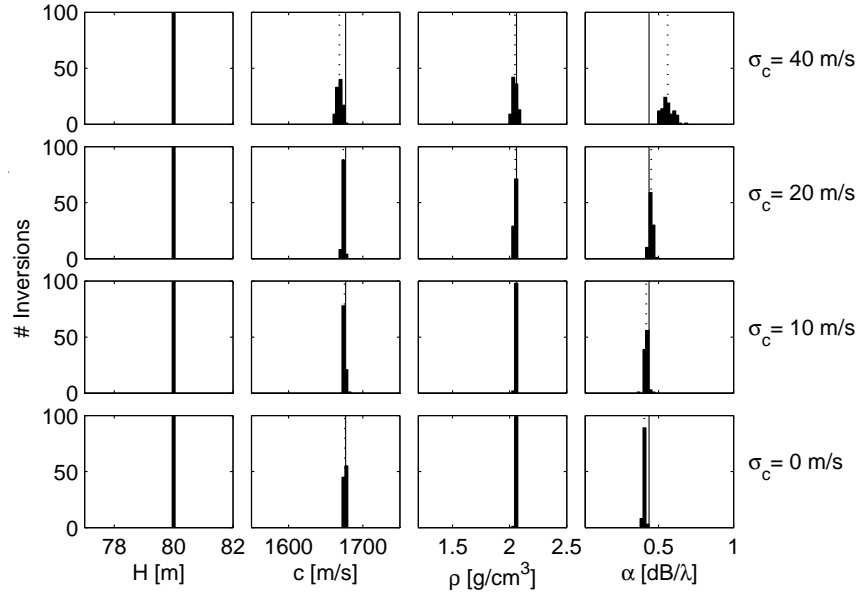


Figure 6.4: Distributions of results from 100 multi-frequency inversions of range-dependent sound speed environments for the hard-bottom case. The true mean (solid line) and distribution mean (dotted line) are included.

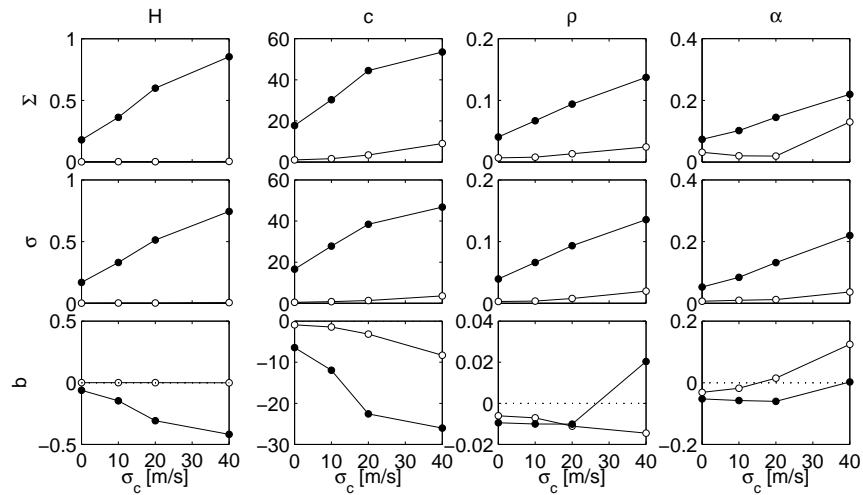


Figure 6.5: Summary of inversion results for the hard-bottom case with range-dependent sound speed. Results from multi-frequency (open circles) and single-frequency inversions (solid circles) are shown.

For multi-frequency inversion, a small negative bias occurs for  $c$ , and larger positive biases occur for  $\rho$  and  $\alpha$  with values of approximately  $0.3 \text{ g/cm}^3$  and  $1 \text{ dB}/\lambda$ , respectively, for  $\sigma_c = 40 \text{ m/s}$ . For  $\sigma_c \geq 20 \text{ m/s}$ , the biases for  $\rho$  and  $\alpha$  are larger for multi-frequency inversion than single-frequency inversion. However, biases for  $c$  are smaller for multi-frequency inversion for all  $\sigma_c$ . Water depth  $H$  is essentially unbiased for multi-frequency inversion (maximum bias:  $-0.1 \text{ m}$ ).

The geoacoustic parameter biases may be explained by examining the effect that range-dependent sound-speed fluctuations have on the average seabed reflection coefficient. Figure 6.8 shows reflection coefficient versus grazing angle curves for the soft- and hard-bottom cases. The solid curves show the reflection coefficient for the true mean geoacoustic parameters. The dashed curves represent the reflection coefficient averaged over 1000 random seabed sound speeds drawn from a uniform distribution of standard deviation  $\sigma_c = 40 \text{ m/s}$  centered at the true mean sound speed (i.e, simulating the effect of range-dependent sound-speed fluctuations) and the true values of density and attenuation. This curve illustrates the nonlinearity of the reflection coefficient: the net effect of averaging over symmetric, uniformly-distributed sound-speed fluctuations is to decrease the seabed reflection coefficient at angles below the critical angle (which contribute most to long-range propagation). The dotted curves show the average reflection coefficient calculated from the 100 multi-frequency inversion results for  $\sigma_c = 40 \text{ m/s}$  (shown in Figs. 6.4 and 6.6). In Fig. 6.8, the biases in the inversion results for  $c$ ,  $\rho$ , and  $\alpha$  decrease the average reflection coefficient at angles below critical, similar to the curve averaged over random seabed sound speeds. The decrease in average seabed reflection coefficient due to range-dependent sound speed fluctuations increases the loss into the seabed. To compensate for this loss and improve the match between the measured and replica fields, the inversions find combinations of range-independent geoacoustic parameters that also lower the seabed reflection coefficient, introducing biases into the parameter estimates. Figure 6.8 shows that this effect is much greater for the soft-bottom case.

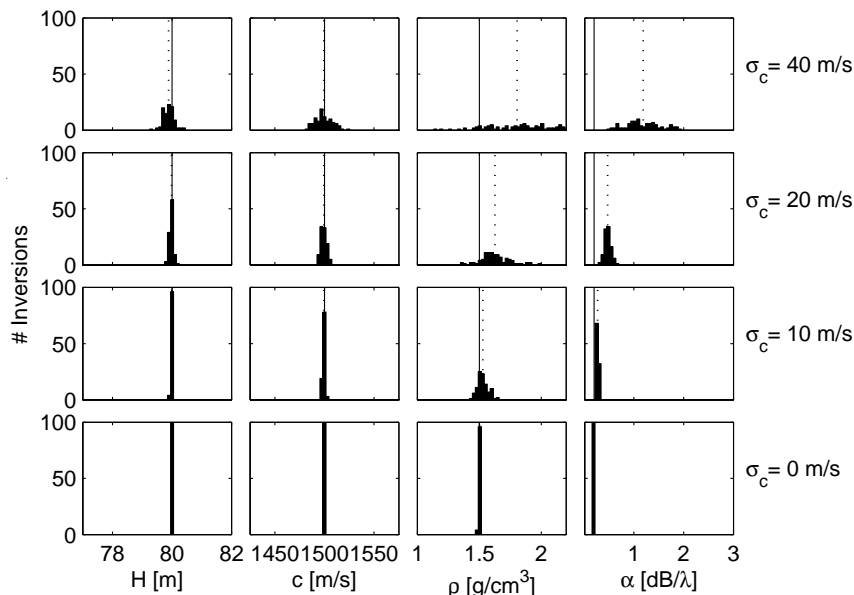


Figure 6.6: Distributions of results from 100 multi-frequency inversions of range-dependent sound speed environments for the soft-bottom case. The true mean (solid line) and distribution mean (dotted line) are included.

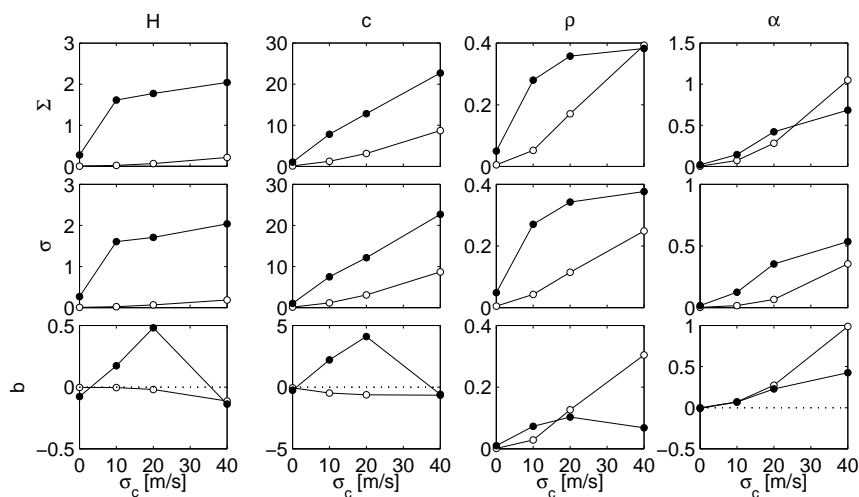


Figure 6.7: Summary of inversion results for the soft-bottom case with range-dependent sound speed. Results from multi-frequency (open circles) and single-frequency inversions (solid circles) are shown.

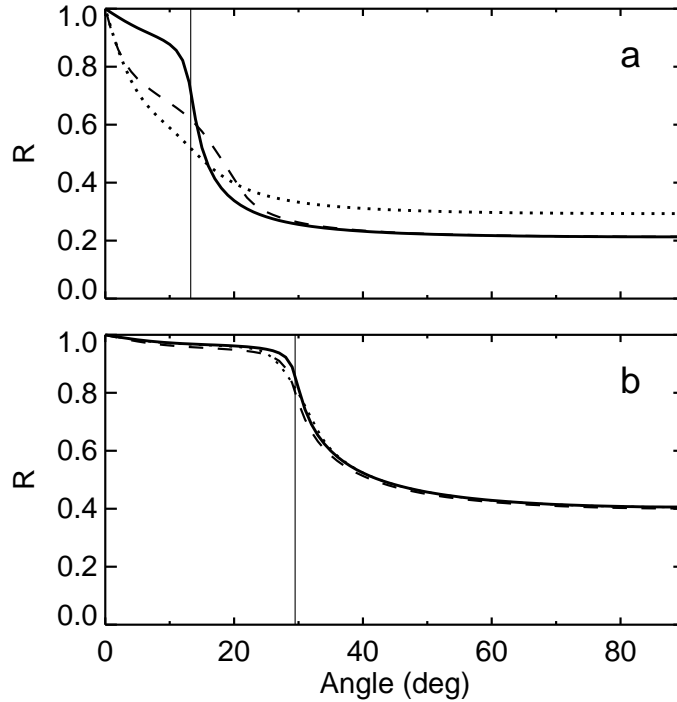


Figure 6.8: Reflection coefficient ( $R$ ) versus grazing angle for (a) soft-bottom, and (b) hard-bottom cases. See text for explanation of curves. Critical angles are indicated by vertical lines.

### 6.3.3 Range-dependent bathymetry

#### Hard-bottom case

This section considers the sensitivity of MFI to neglected fluctuations in water depth for the hard-bottom case. Data were generated for  $\lambda_{\max} = 0.5$  km and several different water-depth standard deviations varying from  $\sigma_H = 0$  m (range independent) to  $\sigma_H = 1$  m. Figure 6.9 shows that the ensemble of multi-frequency inversion results for  $\sigma_H > 0$  m are shifted to lower values for  $c$  and  $\rho$  and to higher values for  $\alpha$  (all inversion results for  $\alpha$  are greater than the true value). A statistical summary of the results for both single- and multi-frequency inversions is given in Fig. 6.10. The standard deviations for  $H$  and  $c$  and the biases for  $H$  are significantly reduced when multiple frequencies are employed. However, large negative biases in  $c$  and  $\rho$  and

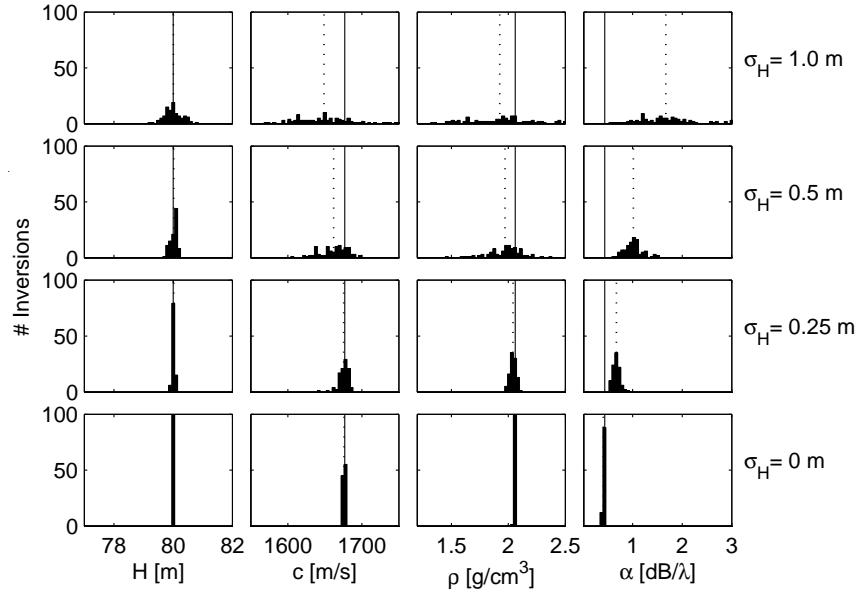


Figure 6.9: Distributions of results from 100 multi-frequency inversions of range-dependent water depth environments for the hard-bottom case. The true mean (solid line) and distribution mean (dotted line) are included.

positive biases in  $\alpha$  occur for multi-frequency inversion for  $\sigma_H > 0.25$  m, with values of approximately  $-28$  m/s,  $-1.4$  g/cm<sup>3</sup>, and  $1.2$  dB/ $\lambda$ , respectively, at  $\sigma_H = 1$  m. The biases in  $\alpha$  are larger for multi-frequency than single-frequency inversion.

The biases observed in Fig. 6.10 can be explained with energy loss arguments. Bathymetric undulations affect the grazing angle at the seabed, which increases the acoustic energy lost into the bottom over up-slope sections. This loss can be partially compensated in the range-independent approximation by reducing the seabed sound speed or density and/or by increasing the attenuation, all of which make the reflection coefficient smaller below the critical angle.

To investigate the inter-relationships between parameters, the multi-frequency inversions for  $\sigma_H = 0.5$  m were repeated with  $\alpha$  held constant at its true value. The biases in  $c$  and  $\rho$  increased to  $-37$  m/s and  $-0.24$  g/cm<sup>3</sup> from values of  $-15$  m/s and  $-0.09$  g/cm<sup>3</sup> when  $\alpha$  is included in the inversion (Fig. 6.10). Hence, by fixing  $\alpha$  the inversion finds even lower values for  $c$  and  $\rho$  to account for the increased bottom loss

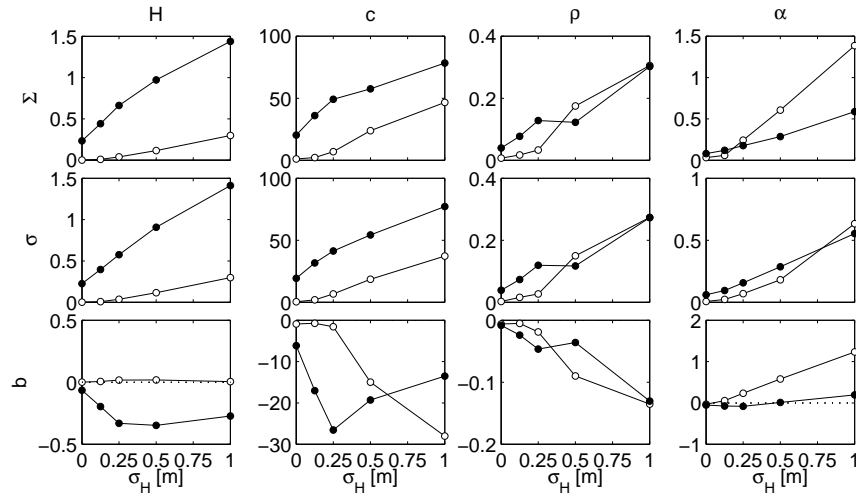


Figure 6.10: Summary of inversion results for the hard-bottom case with range-dependent water depth. Results from multi-frequency (open circles) and single-frequency inversions (solid circles) are shown.

due to the bathymetric fluctuations.

### Soft-bottom case

A summary of the distribution of inversion results for the soft-bottom case with range-dependent bathymetry is shown in Fig. 6.11. The standard deviations and biases for  $H$  for multi-frequency inversions are similar to the hard-bottom case (Fig. 6.10); however, the standard deviations and biases for the seabed parameters are much smaller. Even for the largest value of  $\sigma_H$ , the inversion results for all parameters are in good agreement with the true mean values with little bias and small uncertainty. Since the water and seabed sound speeds are similar for the soft-bottom case, the exact depth of the interface is less important than in the hard-bottom case, and there is low sensitivity to water-depth fluctuations. As in previous cases, the standard deviations are smaller for multi-frequency than single-frequency inversion.

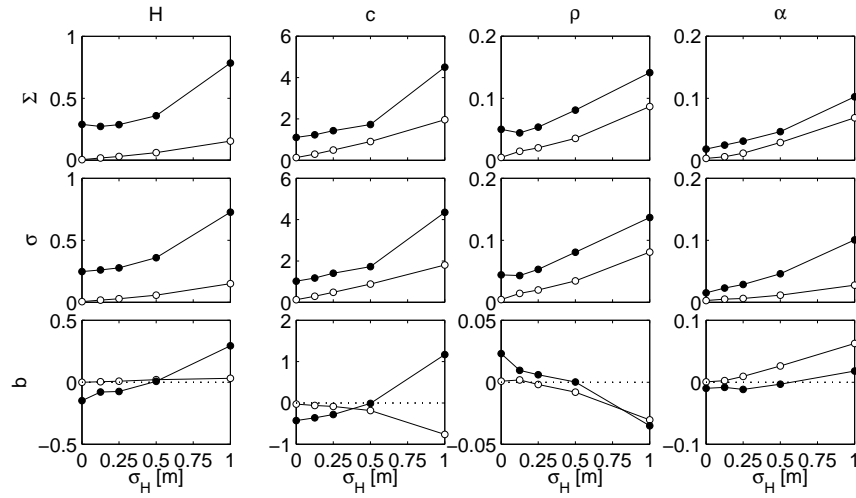


Figure 6.11: Summary of inversion results for the soft-bottom case with range-dependent water depth. Results from multi-frequency (open circles) and single-frequency inversions (solid circles) are shown.

### Effect of horizontal variation scale ( $\lambda_{\max}$ )

The inversions for range-dependent bathymetry considered so far held  $\lambda_{\max}$  (maximum wavelength of bathymetric fluctuations) fixed at 0.5 km. To examine the effect of varying the horizontal scale of the water depth variations, inversions were carried out for several values of  $\lambda_{\max}$  from 0.5 km to  $\infty$  km (range independent) with  $\sigma_H$  fixed at 1 m. (For examples of the dependence of bathymetry on  $\lambda_{\max}$ , see Fig. 6.2.) A summary of the multi-frequency inversion results for both the hard- and soft-bottom cases is given in Fig. 6.12. For the hard-bottom case, the results show a sharp transition between good results (small biases and standard deviations) for  $\lambda_{\max} \geq 1.5$  km and much poorer results (including large negative biases in  $c$  and  $\rho$  and positive biases in  $\alpha$ ) for  $\lambda_{\max} < 1.5$  km. The soft-bottom case shows no sharp transition, and the biases and standard deviations for  $c$ ,  $\rho$ , and  $\alpha$  are much smaller than for the hard-bottom case for  $\lambda_{\max} \leq 1$  km. Water depth  $H$  shows little bias in all cases.

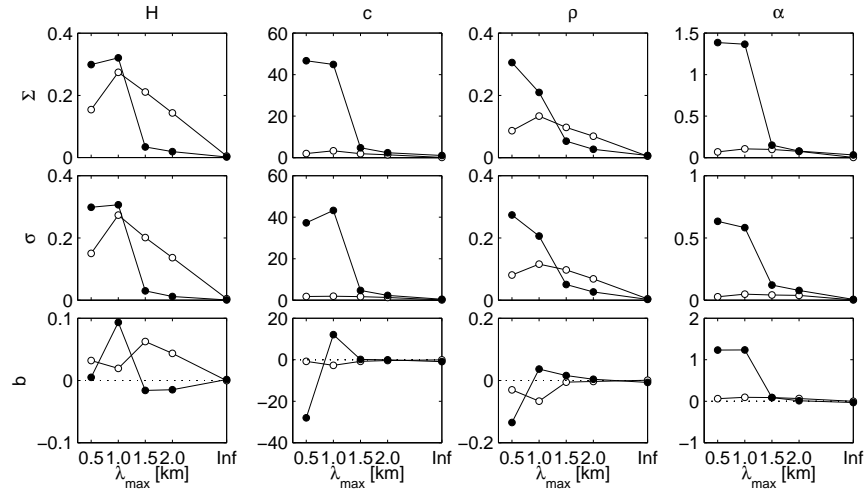


Figure 6.12: Comparison of multi-frequency inversion results for hard-bottom case (solid circles) and soft-bottom case (open circles) for different horizontal scales of range-dependent water depth,  $\lambda_{\max}$ , with  $\sigma_H = 1.0$  m.

## 6.4 Bayesian inversion results

The ensemble inversion results presented in the previous section indicate that neglecting range dependence can introduce a bias in the optimal geoacoustic parameter estimates. In this section, Bayesian inversion is applied to examine the effect of neglected range dependence on parameter uncertainty distributions. The two cases that exhibited the largest biases are considered: range-dependent sound speed for the soft-bottom environment, and range-dependent bathymetry for the hard-bottom environment (multi-frequency inversions are considered in both cases).

In Bayesian inversion, the solution to the inverse problem is characterized by PPD, which is interpreted through integral moments such as marginal probability (uncertainty) distributions. Evaluating these integrals involves sampling models from the parameter space in an efficient manner. The fast Gibbs sampler algorithm [25, 26], used here, applies the Markov chain Monte Carlo method of Metropolis Gibbs sampling in a principal-component parameter space to provide efficient PPD sampling.

While data errors are usually treated as spatially uncorrelated in optimization

inversion, it has been shown that this assumption can lead to underestimating parameter uncertainties in a Bayesian approach [27]. In this study, the closely spaced hydrophones and theory error due to the neglected range dependence lead to correlated data errors. To account for error correlations, the likelihood-based mismatch function used in the Bayesian inversions consists of a sum of covariance-weighted Bartlett mismatches [27],

$$E = \sum_f \mathbf{p}_f^\dagger \mathbf{C}_f^{-1} \mathbf{p}_f - \frac{|\mathbf{w}_f^\dagger \mathbf{C}_f^{-1} \mathbf{p}_f|^2}{\mathbf{w}_f^\dagger \mathbf{C}_f^{-1} \mathbf{w}_f}. \quad (6.4)$$

The covariance matrices,  $\mathbf{C}_f$ , are estimated using an iterative, non-parametric approach based on data residuals [27]. Note that while Eq. 6.4 accounts for error correlations, it is still based on the assumption of unbiased data errors.

Figure 6.13 shows marginal probability distributions from inversions of single (noisy) multi-frequency data sets for the case of range-dependent sound speed for the soft-bottom environment with  $\sigma_c = 10, 20, 40$  m. For sound-speed standard deviation of  $\sigma_c = 10$  m/s, the marginal distributions indicate that the uncertainties in the parameter estimates are relatively small and the distribution means nearly coincide with the true mean parameter values. As  $\sigma_c$  increases, the marginal distributions widen and become biased (shifted away from the true values), with significant positive biases in  $\rho$  and  $\alpha$ . These observations are consistent with the ensemble inversion results given in Fig. 6.6. For  $\sigma_c = 20$  and 40 m/s, the marginal distributions for  $\rho$  and  $\alpha$  in Fig. 6.13 completely exclude the true parameter values.

Marginal probability distributions for the case of range-dependent water depth and a hard bottom are shown in Fig. 6.14 for  $\sigma_H = 0.25, 0.5, 1.0$  m and  $\lambda_{\max} = 0.5$  m. The marginal distributions for  $\alpha$  are biased to significantly higher values, such that the true value is excluded from the distribution in all cases, while the distributions for  $c$  and  $\rho$  are generally biased to slightly lower values. These observations are consistent with the ensemble inversion results in Fig. 6.9.

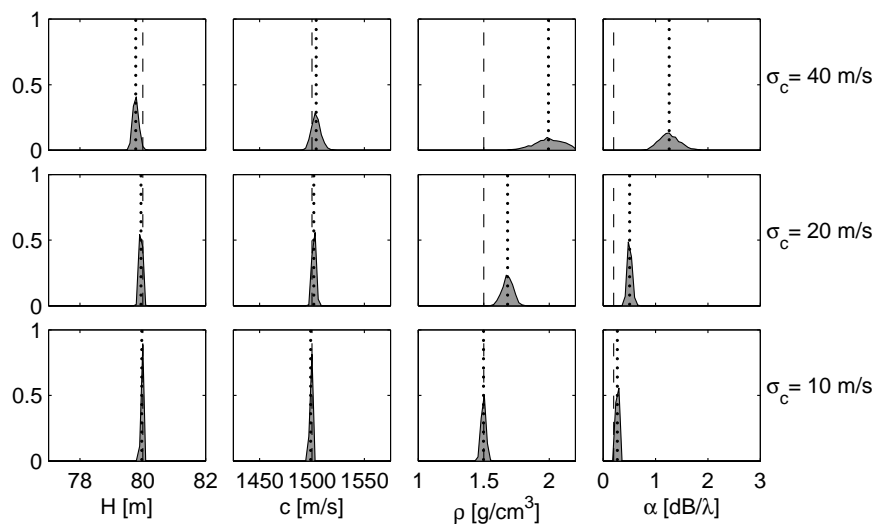


Figure 6.13: Marginal PPDs of single data sets for the case of range-dependent sediment sound speed in the soft-bottom environment. The true mean (dashed line) and distribution mean (dotted line) are shown. Plot bounds indicate parameter search limits.

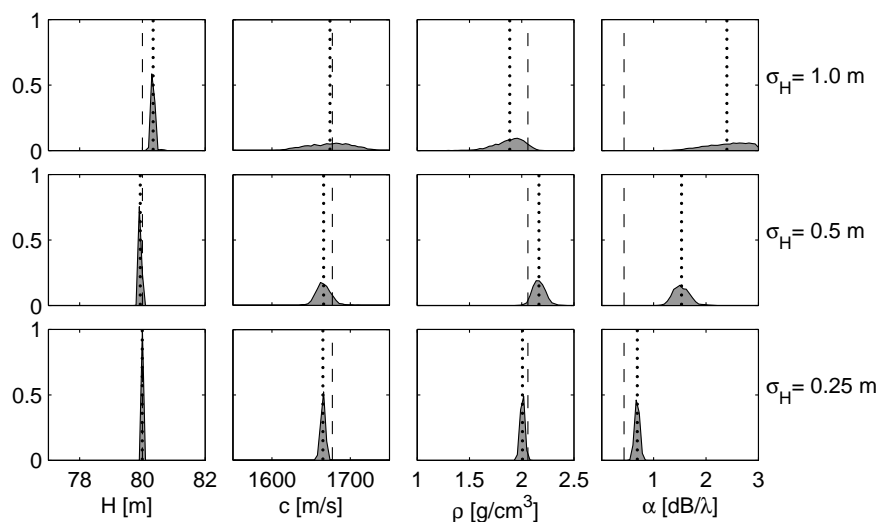


Figure 6.14: Marginal PPDs of single data sets for the case of range-dependent water depth in the hard-bottom environment. The true mean (dashed line) and distribution mean (dotted line) are shown. Plot bounds indicate parameter search limits.

The results in this section confirm that parameter biases introduced by neglected range dependence are not accounted for in standard Bayesian uncertainty analysis. In particular, the estimated parameter uncertainties do not include the effects of parameter biases, and without independent knowledge of the true parameter values there is no indication that the probability distributions obtained are biased.

## 6.5 Summary and discussion

Range dependence at some level is present in virtually all ocean environments but, for computational practicality, the simplifying assumption of range independence is often required for matched-field geoacoustic inversion. Hence, it is important to investigate the possible effects of neglected range dependence on geoacoustic parameter estimates. This issue was investigated here using two approaches: statistical analysis of ensembles of range-independent MFI results for random range-dependent environments [28], and range-independent Bayesian inversion of range-dependent synthetic data. Range dependence was considered in seabed sound speed and water depth for hard- and soft-bottom environments at different scales of lateral variation, and for single- and multi-frequency inversion.

This work suggests that range-dependent fluctuations in sound speed or water depth tend to increase bottom loss, and that neglecting this effect introduces biased theory errors in MFI. These errors ultimately lead to biased parameter estimates in an attempt to account for the additional loss. The largest biases occurred in seabed attenuation, which was biased to high values in all cases. Seabed sound speed was generally biased to low values. Density was biased to low values for all cases except sound-speed range dependence for the soft bottom. It was shown that the biased parameter combinations obtained by range-independent MFI for environments with range-dependent sound speed lowered the seabed reflection coefficient at sub-critical angles in a manner similar to that expected for random sound-speed fluctuations.

Water-depth estimates were essentially unbiased in all cases.

The effects of range dependence were found to differ for different environments. The hard-bottom case was more sensitive to range-dependent water depth, since the large sound-speed contrast between the water and seabed emphasizes the precise location of the interface but reduces the effect of sound-speed fluctuations. Conversely, the soft-bottom case was more sensitive to range-dependent sound speed. Including multiple frequencies in the inversion reduced the variability of parameter estimates (e.g., the standard deviation about the distribution mean). Importantly, however, multi-frequency inversion did not generally reduce parameter biases (except for water depth), and increased biases for seabed attenuation.

Standard MFI approaches are based on the assumption of unbiased data errors, and are generally incapable of detecting biased errors or of assessing their effect on parameter estimates. Hence, synthetic studies such as this are perhaps the only way to investigate quantitatively the effects of neglected range dependence. The simple form of the seabed models considered here allowed for straightforward analysis of biases in terms of halfspace reflection coefficients. Bias effects may be more complicated in more complex environments, but the general conclusions of this work are expected to remain valid.

## Chapter 7

# Conclusions and future work

In this thesis, acoustic inversion methods were applied to estimate receiver positions and seabed geoacoustic properties using measured data consisting of noise generated by a surface ship, and synthetic data. An AEL inversion procedure was demonstrated that uses relative travel time data extracted from the recordings of the ship noise at several locations by cross-correlating the time-series between several hydrophone pairs. The AEL solved for both the receiver and source positions simultaneously and made use of prior information consisting of initial estimates of the positions and the expectation that the source tracks and array shape are smooth. The AEL inversion provided a solution for the VLA location and shape that is consistent with the available information; however, there was very little difference between the prior and recovered source positions. Using a synthetic study, it was demonstrated that for a different source-receiver geometry with a larger horizontal aperture, the data are more informative and the inversion procedure can also provide improved estimates of the source positions. This is a potentially useful technique for positioning underwater receivers without the need for an impulsive source where there is concern about the impact to marine wildlife, or if covertness is required.

MFI using optimization and Bayesian techniques were also applied to ship-noise data. Estimates of the source-receiver ranges from the inversions were well determined

and agreed with the values determined from the results of the AEL inversion; however, there was not enough information in the data to obtain the seabed parameters with any certainty. The data were not well suited to matched-field techniques due to the deep water, short array aperture, low SNR, hydrophone and recording problems, and the severity of the range dependence of the environment.

The latter issue motivated a study into the impact of neglecting environmental range dependence on the results from MFI. It was shown that range-dependent seabed sound speed and water depth can introduce biases in the geoacoustic parameters estimates obtained by MFI when it is assumed that the environment is range independent. Seabed sound speed was generally biased toward lower values, and density was biased toward higher values in all but the case for sound-speed range dependence in a soft-bottom. The greatest effect occurred for the attenuation which was always biased toward higher values. The effects differ for different environments with hard-bottom environments being more sensitive to range-dependent water depth, and soft-bottom environments being more sensitive to range-dependent sound speed. In the case of range-dependent sound speed fluctuations in the seabed, the net effect is to lower the seabed reflection coefficient at the seafloor. To compensate for this, the inversion finds combinations of parameters that similarly lower the reflection coefficient in order to provide the best fit to the data. Including information from multiple frequencies in the inversion did not generally reduce the parameter biases.

Preliminary research using measured and synthetic acoustic data (based in part on work related to this thesis) indicate that the feasibility of using matched-field techniques on ship noise for gas hydrate monitoring is questionable. It is believed that the changes to the region of interest around the gas hydrate monitoring station would likely be small and localized over the time scale considered. Since MFP techniques are generally sensitive to the bulk geoacoustic properties of the seafloor (i.e., meso-scale properties), and not to the fine-scale structure, MFP is not a good candidate technique for this application. In the most recent evolution of the monitoring station

design, there is a reduced emphasis on the concept of continuous monitoring using MFP. Currently, other methods for acoustically monitoring the geoacoustic properties of the gas hydrate bearing sediment using ambient noise are being considered.

One possibility which has been the subject of much research in recent years is seismic coda wave, or ambient noise interferometry. Coda waves refer to the part of a seismic signal that arrives well after the main wave that propagates directly from the source, and consists of long-duration, multiply-scattered, noisy arrivals [82]. The Stanford Exploration Project tested the conjecture that cross-correlating noise traces recorded at two locations enables one to construct the wave-field that would be recorded at one of the locations if there was a source at the other [83]. Since then, it has been shown theoretically that it is possible to extract a time-domain Green's function from these apparently noisy, random signals by cross-correlating the recordings from separated receivers (e.g., Refs. [84–89]). The technique has been demonstrated in laboratory experiments for diffuse fields generated by ultrasonic noise sources [84, 90]. The method has also been demonstrated in underwater acoustics using sea-surface generated ambient ocean noise [69, 77, 91, 92]. In seismology, coda wave and ambient noise interferometry has been applied to estimate large-scale surface- and P-wave speeds [93–97], and to detect temporal changes in the seismic and/or thermal properties of a medium [98, 99]. The latter has potential applications to monitoring volcanoes and waste disposal sites and to earthquake prediction [98].

Adapted to a much smaller scale, the technique could potentially be applied to the gas hydrate monitoring station project to monitor seismic properties in the vicinity of the station using various sources of noise such as wind-generated surface waves and ocean turbulence, microseisms due to salt tectonics, etc. By cross-correlating long-duration, broadband recordings of noise received by the network of bottom-moored HLAs and the borehole array (see Fig. 1.1), it may be possible to devise a tomography experiment to estimate P- and S-wave speeds in a 3D volume beneath the monitoring station. This is purely conjecture; however, if the technique were proved feasible, it

might allow for temporal monitoring of the properties of a gas hydrate system without the need for an active source.

---

## References

- [1] S. E. Dosso, M. R. Fallat, B. J. Sotirin, and J. L. Newton. Array element localization for horizontal arrays via Occam's inversion. *J. Acoust. Soc. Am.*, 104(2):846–859, 1998.
- [2] S. E. Dosso, G. H. Brooke, B. J. Kilistoff, B. J. Sotirin, V. K. McDonald, M. R. Fallat, and N. E. Collison. High-precision array element localization of vertical line arrays in the Arctic Ocean. *IEEE J. Oceanic Eng.*, 23(4):365–379, 1998.
- [3] S. E. Dosso and N. E. Collison. Regularized inversion for towed-array shape estimation. In *Inverse Problems in Ocean Acoustics*, pages 77–103. Springer-Verlag, New York, 2001. edited by M. I. Taroudakis and G. N. Makrakis.
- [4] S. E. Dosso and M. Riedel. Array element location for towed marine seismic arrays. *J. Acoust. Soc. Am.*, 110(2):955–966, 2001.
- [5] S. E. Dosso and N. E. Collison. Acoustic tracking of a freely drifting sonobuoy field. *J. Acoust. Soc. Am.*, 111(5):2166–2177, 2002.
- [6] S. E. Dosso, N. E. B. Collison, G. J. Heard, and R. I. Verrall. Experimental validation of regularized array element localization. *J. Acoust. Soc. Am.*, 115(5):2129–2137, 2004.
- [7] S. E. Dosso and G. R. Ebbeson. Array element localization accuracy and survey design. *Can. Acoust.*, 34(4):3–13, 2006.
- [8] A. Tolstoy. MFP benchmark inversions via the RIGS method. *J. Comput. Acoust.*, 6(1/2):185–203, 1998.
- [9] M. D. Collins, W. A. Kuperman, and H. Schmidt. Nonlinear inversion for ocean-bottom properties. *J. Acoust. Soc. Am.*, 92(5):2770–2783, 1992.
- [10] S. E. Dosso, M. L. Jeremy, J. M. Ozard, and N. R. Chapman. Estimation of ocean-bottom properties by matched-field inversion of acoustic field data. *IEEE J. Oceanic Eng.*, 18(3):232–239, 1993.

- 
- [11] C. E. Lindsay and N. R. Chapman. Matched field inversion for geoacoustic model parameters using adaptive simulated annealing. *IEEE J. Oceanic Eng.*, 18(3):224–231, 1993.
- [12] M. D. Collins and L. Fishman. Efficient navigation of parameter landscapes. *J. Acoust. Soc. Am.*, 98(3):1637–644, 1995.
- [13] M. R. Fallat and S. E. Dosso. Geoacoustic inversion for the Workshop '97 benchmark test cases using simulated annealing. *J. Comput. Acoust.*, 6(1/2):29–44, 1998.
- [14] G. J. Heard, D. Hannay, and S. Carr. Genetic algorithm inversion of the 1997 geoacoustic inversion workshop test case data. *J. Comput. Acoust.*, 6(1/2):61–71, 1998.
- [15] P. Ratilal, P. Gerstoft, and J. T. Goh. Subspace approach to inversion by genetic algorithms involving multiple frequencies. *J. Comput. Acoust.*, 6(1/2):99–115, 1998.
- [16] M. Siderius, P. Gerstoft, and P. L. Nielsen. Broadband geoacoustic inversion from sparse data using genetic algorithms. *J. Comput. Acoust.*, 6(1/2):117–134, 1998.
- [17] M. I. Taroudakis and M. G. Markaki. Bottom geoacoustic inversion by “Broadband” matched-field processing. *J. Comput. Acoust.*, 6(1/2):167–183, 1998.
- [18] P. Gerstoft. Inversion of seismoacoustic data using genetic algorithms and *a posteriori* probability distributions. *J. Acoust. Soc. Am.*, 95(2):770–782, 1993.
- [19] M. R. Fallat and S. E. Dosso. Geoacoustic inversion via local, global, and hybrid algorithms. *J. Acoust. Soc. Am.*, 105(6):3219–3230, 1999.
- [20] M. Musil, N. R. Chapman, and M. J. Wilmut. Range-dependent matched-field inversion of Swellex-96 data using the downhill simplex algorithm. *J. Acoust. Soc. Am.*, 106(6):3270–3281, 1999.
- [21] M. R. Fallat, P. L. Nielsen, and S. E. Dosso. Hybrid geoacoustic inversion of Mediterranean Sea data. *J. Acoust. Soc. Am.*, 107(4):1967–1977, 2000.
- [22] S. E. Dosso, M. J. Wilmut, and A.-L. S. Lapinski. An adaptive-hybrid algorithm for geoacoustic inversion. *IEEE J. Oceanic Eng.*, 26(3):324–336, 2001.
- [23] P. Gerstoft and C. F. Mecklenbräuker. Ocean acoustic inversion with estimation of *a posteriori* probability distributions. *J. Acoust. Soc. Am.*, 104(2):808–819, 1998.

- 
- [24] S. E. Dosso and M. J. Wilmut. Quantifying data information content in geoaoustic inversion. *IEEE J. Oceanic Eng.*, 27(2):296–304, 2002.
- [25] S. E. Dosso. Quantifying uncertainty in geoaoustic inversion I: A fast Gibbs sampler approach. *J. Acoust. Soc. Am.*, 111(1):129–142, 2002.
- [26] S. E. Dosso and P. L. Nielsen. Quantifying uncertainty in geoaoustic inversion II: Application to broadband, shallow-water data. *J. Acoust. Soc. Am.*, 111(1):143–159, 2002.
- [27] S. E. Dosso, P. L. Nielsen, and M. J. Wilmut. Data error covariance in matched-field geoaoustic inversion. *J. Acoust. Soc. Am.*, 119(1):208–219, 2006.
- [28] A.-L. S. Lapinski and D. M. Chapman. The effects of ignored seabed variability in geoaoustic inversion. *J. Acoust. Soc. Am.*, 117(6):3524–3538, 2005.
- [29] M. R. Fallat, S. E. Dosso, and P. L. Nielsen. An investigation of algorithm-induced variability in geoaoustic inversion. *IEEE J. Oceanic Eng.*, 29(1):78–87, 2004.
- [30] C. F. Mecklenbräuker and P. Gerstoft. Objective functions for ocean acoustic inversion derived by maximum likelihood methods. *J. Comput. Acoust.*, 8(2):259–270, 2000.
- [31] K. A. Kvenvolden and T. D. Lorenson. The global occurrence of natural gas hydrate. In *Natural Gas Hydrates: Occurrence, Distribution, and Detection*, pages 3–18. American Geophysical Union, Washington, D.C., 2001. edited by C. K. Paull and W. P. Dillon.
- [32] K. A. Kvenvolden. Potential effects of gas hydrates on human welfare. In *Proceedings of the National Academy of Sciences*, volume 96, pages 3420–3426, 1999.
- [33] A. V. Milkov. Global estimates of hydrate-bound gas in marine sediments: how much is really out there? *Earth Sci. Rev.*, 66:183–197, 2004.
- [34] B. Buffet and D. Archer. Global inventory of methane clathrate: sensitivity to changes in the deep ocean. *Earth Planet. Sci. Lett.*, 227:185–199, 2004.
- [35] K. P. Shine, R. G. Derwent, D. J. Wuebbles, and J. J. Morcriste. Radiative forcing of climate change. In *Climate Change, The IPCC Scientific Assessment*. Cambridge Univ. Press, 1990. eds. J. T. Houghton, G. J. Jenkins, and J. J. Ephraums.
- [36] C. K. Paull, W. Ussler, and W. P. Dillon. Potential role of gas hydrate decomposition in generating submarine slope failures. In *Natural Gas Hydrate in Oceanic and Permafrost Environments*, pages 149–156. Kluwer Academic Publishers, Dordrecht, The Netherlands, 2000. edited by M. D. Max.

- [37] T. Bugge, S. Befring, R. Belderson, T. Eidvin, J. Eystein, N. H. Kenyon, H. Holtedahl, and H. P. Sejrup. A giant three-stage submarine slide off Norway. *Geo-Mar. Lett.*, 7:191–198, 1987.
- [38] H. E. Brown, W. S. Holbrook, M. J. Hornbach, and J. Nealon. Slide structure and role of gas hydrate at the northern boundary of the Storegga Slide offshore Norway. *Marine Geology*, 229:179–186, 2006.
- [39] M. Hovland and O. T. Gudmestad. Potential influence of gas hydrates on seabed installations. In *Natural Gas Hydrates: Occurrence, Distribution, and Detection*, pages 307–315. American Geophysical Union, Washington, D.C., 2001. edited by C. K. Paull and W. P. Dillon.
- [40] X. Liu and P. B. Flemings. Dynamic multiphase flow model of hydrate formation in marine sediments. *J. Geophys. Res.*, 112:B03101–1–B03101–23, 2007.
- [41] T. M. McGee and J. R. Woolsey. A remote station to monitor gas hydrate outcrops in the Gulf of Mexico. In *Gas Hydrates: Challenges for the Future*, volume 912, pages 527–532. New York Academy of Sciences, 2000.
- [42] A. Tolstoy. *Matched Field Processing for Underwater Acoustics*. World Scientific Publishing Co. Pte. Ltd., Singapore, 1993.
- [43] A. B. Baggeroer, W. A. Kuperman, and P. M. Mikhalevsky. An overview of matched field methods in ocean acoustics. *IEEE J. Oceanic Eng.*, 18(4):401–424, 1993.
- [44] W. S. Hodgkiss, P. Gerstoft, and J. J. Murray. Array shape estimation from sources of opportunity. In *Proc. Oceans Conf.*, volume 1, pages 582–585, San Diego, CA., 1999.
- [45] E. K. Westwood and D. P. Knobles. Source track localization via multipath correlation matching. *J. Acoust. Soc. Am.*, 102(5):2645–2654, 1997.
- [46] B. F. Kuryanov and A. I. Vedenev. Investigation of the bottom sediment profiling method in the deep ocean by means of ship noise analysis. *Oceanology*, 34(4):563–570, 1995.
- [47] N. R. Chapman, R. M. Dizaji, and R. L. Kirilin. Geoacoustic inversion using broad band ship noise. In *Proceedings of the fifth European Conference on Underwater Acoustics*, volume 1, pages 787–792, Lyon, France, 2000.
- [48] D. J. Battle, P. Gerstoft, W. A. Kuperman, W. S. Hodgkiss, and M. Siderius. Geoacoustic inversion of tow-ship noise via near-field matched-field-processing. *IEEE J. Oceanic Eng.*, 28(3):454–467, 2003.

- [49] M. Nicholas, J. S. Perkins, G. J. Orris, and L. T. Fialkowski. Environmental inversion and matched-field tracking with a surface ship and an l-shaped receiver array. *J. Acoust. Soc. Am.*, 116(5):2891–2901, 2004.
- [50] R. Koch and D. P. Knobles. Geoacoustic inversion with ships as sources. *J. Acoust. Soc. Am.*, 117(2):636–637, 2004.
- [51] D. Tollefsen, S. E. Dosso, and M. J. Wilmut. Matched-field geoacoustic inversion with a horizontal array and a low-level source. *J. Acoust. Soc. Am.*, 120(1):221–230, 2006.
- [52] W. Menke. *Geophysical Data Analysis: Discrete Inverse Theory*. Academic Press, New York, 1984.
- [53] A. Tarantola. *Inverse Problem Theory: Methods for data fitting and model parameter estimation*. Elsevier Science Publishing B.V., Amsterdam, 1987.
- [54] M. Sen and P. L. Stoffa. *Global Optimization Methods in Geophysical Inversion*. Elsevier Science, B.V., Amsterdam, 1995.
- [55] M. R. Fallat, P. L. Nielsen, S. E. Dosso, and M. Siderius. Geoacoustic characterization of a range-dependent ocean environment using towed array data. *IEEE J. Oceanic Eng.*, 30(1):198–206, 2005.
- [56] R. M. S. Barlee and N. R. Chapman. Geoacoustic model parameter estimation using a bottom-moored hydrophone array. *IEEE J. Oceanic Eng.*, 30(4):773–783, 2005.
- [57] Y.-M. Jiang and N. R. Chapman. Quantifying the uncertainty of geoacoustic parameter estimates for the new jersey shelf by inverting air gun data. *J. Acoust. Soc. Am.*, 121(4):1879–1894, 2007.
- [58] J. A. Nelder and R. Mead. A simplex method for function minimization. *Computer Journal*, 7:308–313, 1965.
- [59] M. Musil. Range-dependent matched-field inversion using the downhill simplex algorithm. Master’s thesis, University of Victoria, 1998.
- [60] E. K. Press, S. A. Teukolsky, W. T. Vetterling, and B. P. Flannery. *Numerical Recipes in FORTRAN, 2nd ed.* Cambridge University Press, Cambridge, 1992.
- [61] S. Kirkpatrick, Jr. Gelatt, C. D., and M. P. Vecchi. Optimization by simulated annealing. *Science*, 220:671–680, 1983.
- [62] N. Metropolis, A. Rosenbluth, M. Rosenbluth, A. Teller, and E. Teller. Equation of state calculation by fast computing machines. *J. Chem. Phys.*, 21:1087–1092, 1953.

- [63] H. Szu and R. Hartley. Fast simulated annealing. *Phys. Lett.*, 122:157–162, 1987.
- [64] M. Sen and P. L. Stoffa. Bayesian inference, Gibbs’ sampler and uncertainty estimation in geophysical inversion. *Geophysical Prospecting*, 44:313–350, 1996.
- [65] S. E. Dosso and M. J. Wilmut. Data uncertainty estimation in matched-field geoacoustic inversion. *IEEE J. Oceanic Eng.*, In Press.
- [66] F. B. Jensen, W. A. Kuperman, M. B. Porter, and H. Schmidt. *Computational Ocean Acoustics*. AIP Press, New York, 1994.
- [67] G. V. Frisk. *Ocean and Seabed Acoustics - A Theory of Wave Propagation*. P T R Prentice Hall, New Jersey, 1994.
- [68] E. K. Westwood, C. T. Tindle, and N. R. Chapman. A normal mode model for acousto-elastic ocean environments. *J. Acoust. Soc. Am.*, 100:3631–3645, 1996.
- [69] G. H. Brooke, D. J. Thomson, and G. R. Ebbeson. PECan: A Canadian parabolic equation model for underwater sound propagation. *J. Comput. Acoust.*, 9:69–100, 2001.
- [70] M. D. Collins. The split-step Padé solution for the parabolic equation method. *J. Acoust. Soc. Am.*, 93:1736–1742, 1993.
- [71] Z. Y. Zhang and C. T. Tindle. Improved equivalent fluid approximations for a low shear speed ocean bottom. *J. Acoust. Soc. Am.*, 98(6):3391–3396, 1995.
- [72] T. W. Neurauter and W. R. Bryant. Gas hydrates and their association with mud diapir/mud volcanos on the Louisiana continental slope. In *Proceedings of the 21st Offshore Technology Conference*, volume 1, pages 599–607, 1989.
- [73] E. Geresi, C. Lutken, T. McGee, and A. Lowrie. Complex geology and gas hydrate dynamics characterize Mississippi Canyon Block 798 on the upper continental slope of northern Gulf of Mexico. *Gulf Coast Ass. of Geo. Soc. Trans.*, 52:309–321, 2002.
- [74] M. I. Taroudakis and M. G. Markaki. Bottom geoacoustic inversion by matched-field processing – a sensitivity study. *Inverse Problems*, 16:1679–1692, 2000.
- [75] S. E. Dosso and B. J. Sotirin. Optimal array element localization. *J. Acoust. Soc. Am.*, 106(6):3445–3459, 1999.
- [76] L. E. Freitag and P. L. Tyack. Passive acoustic localization of the Atlantic bottlenose dolphin using whistles and echolocation clicks. *J. Acoust. Soc. Am.*, 93(4):2197–2205, 1993.

- 
- [77] K. G. Sabra, P. Roux, A. M. Thode, G. L. D'Spain, W. S. Hodgkiss, and W. A. Kuperman. Using ocean ambient noise for array self-localization and self-synchronization. *IEEE J. Oceanic Eng.*, 30(2):338–347, 2005.
- [78] M. M. Zykov. *3-D Travel Time Tomography of the Gas Hydrate Area Off-shore Vancouver Island Based on OBS Data*. PhD thesis, University of Victoria, 2005.
- [79] R. J. Urick. *Principles of Underwater Sound*. McGraw-Hill Inc., New York, 1983.
- [80] A.-L. S. Lapinski and S. E. Dosso. Bayesian geoacoustic inversion for the Inversion Techniques 2001 Workshop. *IEEE J. Oceanic Eng.*, 28(3):380–393, 2003.
- [81] E. Geresi. *Vertical line array performance in gas hydrate bearing sediments in the Northern Gulf of Mexico*. PhD thesis, University of Victoria, 2007.
- [82] R. L. Weaver. Information from seismic noise. *Science*, 307:1568–1569, 2005.
- [83] J. Claerbout and J. Rickett. Acoustic daylight imaging via spectral factorization: Helioseismology and reservoir monitoring. *The Leading Edge*, 18(8):957–960, 1999.
- [84] O. I. Lobkis and R. L. Weaver. On the emergence of the Green's function in the correlations of a diffuse field. *J. Acoust. Soc. Am.*, 110(6):3011–3017, 2001.
- [85] A. Derode, E. Larose, M. Tanter, J. de Rosny, A. Tourin, M. Campillo, and M. Fink. Recovering the Green's function from field-field correlations in an open scattering medium. *J. Acoust. Soc. Am.*, 113(6):2973–2976, 2003.
- [86] R. Sneider. Extracting the Green's function from the correlation of coda waves: A derivation based on stationary phase. *Phys. Rev. E*, 69(6):046610–1–046610–8, 2004.
- [87] K. G. Sabra, P. Gerstoft, P. R. Roux, W. A. Kuperman, and M. C. Fehler. On the emergence of the Green's function in the correlations of a diffuse field. *Geophys. Res. Lett.*, 32:L03310, 2005.
- [88] K. G. Sabra, P. Roux, and W. A. Kuperman. Arrival-time structure of the time-averaged ambient noise cross-correlation function in an oceanic waveguide. *J. Acoust. Soc. Am.*, 117(1):164–174, 2005.
- [89] K. Wapenaar. Nonreciprocal Green's function retrieval by cross correlation. *J. Acoust. Soc. Am.*, 120(1):EL7–EL13, 2006.
- [90] A. Derode, E. Larose, M. Campillo, and M. Fink. How to estimate the Green's function of a heterogenous medium between two passive sensors? application to acoustic waves. *App. Phys. Lett.*, 83(15):3054–3056, 2003.

- 
- [91] P. Roux and W. A. Kuperman. Extracting coherent wave fronts from acoustic ambient noise in the ocean. *J. Acoust. Soc. Am.*, 116(4):1995–2003, 2004.
- [92] K. G. Sabra, P. Roux, and W. A. Kuperman. Emergence rate of the time-domain Green’s function from the ambient noise cross-correlation function. *J. Acoust. Soc. Am.*, 118(6):3524–3531, 2005.
- [93] M. Campillo and A. Paul. Long-range correlations in the diffuse seismic coda. *Science*, 299(5606):547–549, 2003.
- [94] N. M. Shapiro and M. Campillo. Emergence of broadband Raleigh waves from correlations of the ambient seismic noise. *Geophys. Res. Lett.*, 31:L07614–1–L07614–4, 2004.
- [95] N. M. Shapiro, M. Campillo, L. Stehly, and M. Ritzwoller. High-resolution surface-wave tomography from ambient seismic noise. *Science*, 307(5715):1615–1618, 2005.
- [96] P. Roux, K. G. Sabra, P. Gerstoft, and W. A. Kuperman. P-waves from cross-correlation of seismic noise. *Geophys. Res. Lett.*, 32:L19303–1–L19303–4, 2005.
- [97] K. G. Sabra, P. Gerstoft, P. Roux, and W. A. Kuperman. Extracting time-domain green’s function estimates from ambient seismic noise. *Geophys. Res. Lett.*, 32:L03310–1–L03310–5, 2005.
- [98] R. Snieder, A. Grêt, H. Douma, and J. Scales. Coda wave interferometry for estimating nonlinear behavior in seismic velocity. *Science*, 295(5563):2253–2255, 2002.
- [99] R. Sneider and Page. J. Multiple scattering in evolving media. *Physics Today*, 60(5):49–60, 2007.

## List of Abbreviations

4-C	Four component acoustic sensor
ADCP	Acoustic doppler current profiler
AEL	Array element localization
ASSA	Adaptive simplex simulated annealing
AV14	Atwater Valley, Block 14
BHSZ	Base of the hydrate stability zone
BSR	Bottom simulating reflector
CI	Confidence interval
CMRET	Center for Marine Resources and Environmental Technology
CSDM	Cross-spectral density matrix
DATS	Data acquisition and telemetry system
DHS	Downhill simplex method
FGS	Fast Gibbs sampling
FSA	Fast simulated annealing
GPS	Global positioning system
HSZ	Hydrate stability zone
MAP	Maximum <i>a posteriori</i>
MC118	Mississippi Canyon, Block 118
MC798	Mississippi Canyon, Block 798
MFI	Matched-field inversion
MFP	Matched-field processing
PE	Parabolic equation
PPD	Posterior probability density
SA	Simulated annealing
SNR	Signal to noise ratio
UTM	Universal transverse mercator
VLA	Vertical line array
WGS 84	World geodetic system 1984